Institute of Mechanics

Montanuniversität Leoben,Austria

Dissertation

Controlled Rolling Contact Fatigue in Railway Wheels

Brijesh Pratap Singh

Studying Program: G 087 940

March, 2008

I hereby declare that I myself composed this thesis without any assistance from unacknowledged third parties. Furthermore, I confirm that no sources and resources have been used in the preparation of this thesis other than those indicated in the thesis itself. All references have been cited as appropriate.

Leoben, Date Brijesh Pratap Singh

Acknowledgements

It gives me enormous pleasure to see my three years work come to a concluding point. It would have been impossible for me to achieve this success alone, at this point I would like to thank all those who in some way or the other contributed to this work. I am grateful to the vanguards who guided me to this success and I am equally grateful to my friends and colleagues, at the Institute of Mechanics at the Montanuniversität Leoben (MUL) and Materials Center Leoben Forschungs GmbH (MCL), who walked hand in hand with me through this time.

I can only say that I was too lucky to be able to carry out this work under the guidance of Prof. Dr. Franz Dieter Fischer, Head of the Institute of Mechanics, whose comments and input were the basis of all the major conclusions. Throughout my work I was in constant contact with Dr. Werner Daves who leads the wheel-rail simulation group at MCL. I would like to thank Dr. Daves for always being able to spare his precious time to discuss the scientific and technical problems arising during the development of the model and also in interpreting the results.

I would like to say special thanks to Dr. Thomas Antretter for his contribution in overcoming small and big problems in day to day running of the research and also for the high level of hospitality he extended towards me whenever I, as a foreigner, needed the help of a native person.

I would like to thank my colleague Dr. Martina Wiest with whom I could always discuss and clarify my doubts and confusions through informal discussions. I would take the opportunity to thank Siemens Transportation Systems Graz (STS), the industrial partner

for this project, for financially supporting the project and providing the necessary input data as and when needed. Special thanks to Dr. Six Klaus, the contact person at STS.

The nice people that I got to know at MCL and MUL provided such a homely atmosphere for me to live in Leoben that, although away from home, I could concentrate in my work without being homesick. Back home in India, I would like to thank my parents, sisters and friends whose blessings, wishes and trust made me feel strong in all the good and bad times. Last but not least, I would like to thank God for making all of us to be able to work together towards the common goal and bringing us to a conclusion.

Abstract

The current work deals with the problem of rolling contact fatigue found in railway wheels. The finite element method is adopted to mathematically model the wheel-rail system and simulate the loads acting in the system. Results from the multi-body simulation software SIMPACK are integrated in the wheel-rail model developed using the finite element code ABAQUS/Explicit. Different loading scenarios and combinations of these scenarios are analyzed. Reaction forces, reaction moments, slip rates, plastic deformations, stresses and strains in the system are studied. A detailed analysis is made for the plastic strain and the eventual possible damage accumulated in the contact region of the wheel. The detailed analysis is facilitated by modeling only a part of the wheel rather then modeling the complete wheel. A fine mesh in the contact region enables a magnified overview of the development of various physical quantities in the region. Dynamic and quasi-static models are developed. ABAQUS/Standard is used to determine the accumulation of plastic strain in the contact region in a wheel under repeated loading. The damage indicator concept is integrated with the ABAQUS/Standard calculation using a FORTRAN code. A comparison of the results obtained from cyclic loading calculations is made with the shakedown map for a point contact, thus the validity of the shakedown theory in the wheel-rail contact problem is looked upon. Qualitative and quantitative conclusions are drawn regarding the development of damage under the normal service life of a railway wheel. Various loading scenarios identified by the normal load and the traction coefficient are investigated and compared.

Kurzfassung

Die vorliegende Arbeit beschäftigt sich mit dem Problem der Rollkontaktermüdung in Eisenbahnrädern. Mittels Finite-Elemente-Simulationen wurden das Rad-Schiene-System mathematisch nachgebildet und die auftretenden Lasten simuliert. Ergebnisse aus der Mehrkörpersimulationssoftware SIMPACK wurden in das mit ABAQUS/Explicit entwickelte Rad-Schiene-Modell integriert. Verschiedene Lastzustände und Kombinationen von Zuständen wurden analysiert. Auftretende Reaktionskräfte, Momente, Schlupfraten, plastische Deformation, sowie Spannungen und Dehnungen wurden studiert. Eine detaillierte Analyse der plastischen Dehnungen und akkumulierten Schäden in der Kontaktregion wurde durchgeführt. Dies wurde durch das Modellieren eines Teils des Rades, repräsentativ für das ganze Rad, erleichtert. Ein feineres Netz in der Kontaktregion ermöglichte eine genauere Betrachtung der Entwicklung relevanter physikalischer Größen. Es wurden dynamische und quasistatische Rechnungen durchgeführt. ABAQUS/Standard ermöglichte die Berechnung von akkumulierter, plastischer Dehnung in der Kontaktregion unter wiederholter Belastung. Ein in FORTRAN geschriebenes Schadensindikatormodell wurde in die ABAQUS/Standard-Simulation integriert. Die Ergebnisse aus den zyklischen Berechnungen wurden mit der shakedown-map für Punktkontakt verglichen, um die Gültigkeit der shakedown-Theorie beim Rad-Schiene-Kontakt zu überprüfen. Aus der Entwicklung der Schäden während der Lebenszeit eines Eisenbahnrades konnten qualitative und quantitative Schlüsse gezogen werden. Verschiedene Belastungsszenarios wurden in Abhängigkeit von Normalkraft und Traktionskoeffizient untersucht und verglichen.

Contents

Declaration of Originality . . . . . **I**

Acknowledgements . . . . . **III**

Abstract . . . . . **IV**

Kurzfassung . . . . . **V**

Contents . . . . . **VI**

List of Abbreviations . . . . . **IX**

1 Introduction **1**

1.1 Development of damage in wheel 2

1.2 Rolling contact fatigue - RCF 3

1.2.1 Wheel spalling 4

1.2.2 Wheel tread shelling 5

1.2.3 Tread checking 5

1.3 Aims 6

2 Modeling and simulation **8**
2.1 Contact mechanics 9
2.1.1 Hertz theory - application in wheel-rail contact problems 9
2.1.2 Rolling contact 10
2.1.3 Cyclic loading of an elastic plastic material 11
2.2 Modeling methods 14

3 Dynamic Finite Element Calculations in a Purely Elastic Scenario . . **16**
3.1 The finite element model 17
3.1.1 Material Definitions 19
3.1.2 Constraints 19
3.1.3 Mechanical Model 20
3.1.4 Meshing 21
3.1.5 Boundary conditions and coordinate system 22
3.1.6 Calculation steps 23
3.1.7 Results 23

4 Load Analysis at Contact Surface **33**
4.1 Model geometry 33
4.2 Defining the contact point and the loading 36
4.3 Meshing the finite element model 37
4.4 Boundary conditions and coordinate system definitions 38
4.5 Simulation steps 38
4.6 Results 39
4.6.1 Wheel in a straight track 40
4.6.2 Wheel on the inner rail in a curve 41

5 Examination of the plastification of the wheel . . . 43

5.1 Finite element model . . . 43

5.2 Damage indicator . . . 47

5.3 Initial calculations and the results . . . 48

5.4 Conclusions . . . 54

6 Cyclic Calculations . . . 56

6.1 The model . . . 57

6.2 Unidirectional loading . . . 57

6.3 Changing direction . . . 74

6.4 Conclusions . . . 82

7 Conclusion and Future Work . . . 83

7.1 Conclusions . . . 83

7.2 Future work . . . 85

List of Figures . . . 86

List of Tables . . . 91

Bibliography . . . 92

List of Abbreviations

Abbreviation	Meaning
D	Total damage
$\overline{dD}$	Weighted average damage rate
FEM	Finite element method
FSLIPR	Contact slip rate
K	Yield stress
L	Load factor
MBS	Multi-body systems
MCL	Materials Center Leoben
MUL	Montanuniversität Leoben
P	Normal load
$P_0{}^s$	Maximum shear stress
PEEQ	Accumulated equivalent plastic strain
Q	Traction force
RCF	Rolling contact fatigue
RF	Reaction Force
STS	Siemens Transportation Systems
n	Number of cycles
p_0	Maximum Hertz contact pressure
μ	Traction coefficient
μ_f	Friction coefficient

CHAPTER 1

Introduction

Today the railways bear the great responsibility of providing a safe, comfortable and fast method of transport on land. Apart from being the key medium of goods transport on land, railway is the most popular means amongst the travel enthusiasts and regular long distance travelers.

This increased popularity of railways has put forward the challenges of high axle loads, fast running speeds, smaller turning radii and increased frequency of accelerating (and braking). These conditions have a negative effect on the service life of the railway wheel and the rail.

The level of comfort and speed offered by the railways makes it possible to travel thousands of kilometers on train without much stress. No doubt there is a need of continuing the engineering development and research to enhance the quality of traveling and to maximize the safety of people involved. Despite continuing engineering development and research the railway system has not been able to attain all the desired safety standards.

Small and big railway accidents occur often in the global railway network. These accidents sometimes cause great loss in terms of life and property.

It is not very long back when a tragic accident occurred in Germany and took many lives. June 3, 1998 - the Eschede train disaster, Eschede, Germany: Part of a high-speed ICE train derails as leaving 101 people dead. The driver and many people in the front part of the train were among the survivors while the rear part of the train was completely engulfed by the disaster [1] , [2]. **Fig. 1.1** shows the tragic accident site.

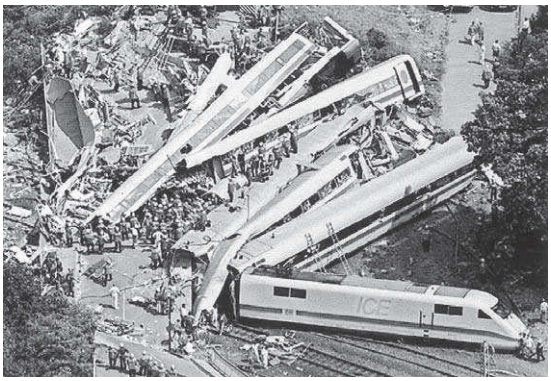

Figure 1.1: Accident site of the German high speed ICE train - Röntgen, June 3rd, 1998 [1]

Investigations were made and it was found out that the accident took place because of the fracture of a wheel, the fractured wheel is shown in **Fig. 1.2**. A few such disasters can easily be quoted for each decade since the railway industry came into existence.

Figure 1.2: Fracture surface of the tyre of the broken railway wheel [1]

1.1 Development of damage in wheel

The service life of a wheel and the mode how the damage develops depend greatly on the service conditions to which the wheel has been subjected. These service conditions include track structure, vehicle type, car load, weather conditions etc. Plastic deformation, fatigue and wear are a few typical failure mechanisms which are encountered in the wheel-rail system.

Wear is a slow and practically visible deterioration process hence can be easily detected on the wheel. On the other hand fatigue failures are abrupt fractures in the wheel or

sudden loss of wheel tread surface material. Because of the unpredictable nature, fatigue is considered quite dangerous. Apart from the direct damage of wheels, fatigue of a wheel has negative side effects like rail damage, damage in the suspensions of train or in some cases unexpected derailment of the train, [3]. In the following section, a detailed background and discussion will be presented on the phenomena of rolling contact fatigue.

1.2 Rolling contact fatigue - RCF

Rolling Contact Fatigue failure is a permanent and quite a severe problem and hence of a major concern to the modern railway industry and the research groups working on wheel-rail contact problems. For years, research in this direction has been going on in several research groups around the world. By use of fast computers and efficient modeling methods like the finite element method (FEM) results are obtained in much less time and at drastically reduced costs.

The design and selection of wheels for different applications should be based on a well-founded understanding about RCF, which - interacting with other forms of surface damage - specifically wear becomes the most important process influencing the service life of railway wheels [4].

Rolling contact fatigue failure may initiate on the surface or in the subsurface region as deep as 7 mm beneath the rolling surface and propagate through the wheel material in a plane at a certain angle to the radial direction.

Based on the position of initiation, the fatigue of a railway wheel can be classified into three broad categories; surface initiated, subsurface initiated and deep surface initiated fatigue failures [3].

Surface failure gives rise to cracks on the wheel surface. The cracks appearing due to the thermal stresses caused by on-tread friction braking are small in size and appear axial to the wheel tread, these cracks generally result in a minor loss of material from the tread [3]. The second type of cracks appear due to mechanical stress at the contact surface due to cyclic loading and unloading. It is found out that thermal cracks constitute only five percent of the total cases of railroad wheel fracture [3]. The major part of the cracks are due to mechanical loads acting on the wheel.

According to Zakharov and Goryacheva, [5], three types of RCF phenomena exist,

- Wheel spalling
- Wheel tread shelling

- Tread checking

1.2.1 Wheel spalling

In simple words spalling can be defined as the breaking off of the material from the surface and near surface regions.

In the case of a railway wheel spalling occurs because of the thermo-mechanical stresses arising in the wheel-rail contact region. As the wheel slides on the rail during braking, the frictional work produces a high amount of thermal energy, see paper [6]. This thermal energy may raise the local temperature of the wheel above the austenitization limits followed by rapid cooling down leading to a martensitic phase transformation, hence disturbing the microstructure of the wheel material (A detailed discussion on the microstructural aspect of this process is presented by Ahlström and Karlsson in [7]). Eventually, under the influence of cyclic loading, this martensitic region fractures. Surface and subsurface hardness of the wheel also changes because of spalling. **Fig. 1.3** shows that the hardness of the grey spot is almost twice as high as that of the work hardened wheel tread surface. Another point to be noted is that the the grey spot is relatively softer at the center as compared to the boundaries [5].

The experimental work by Makino, Yamamoto and Fujimura [8] describes the spalling property of a wheel as combination of RCF property and the impact load. The impact load is independent of the material properties but depends on the shape of the existing flat. The RCF property is found to be dependent on the hardness of the material. It is found that low hardness material has a short life, given the same Hertzian stress [8].

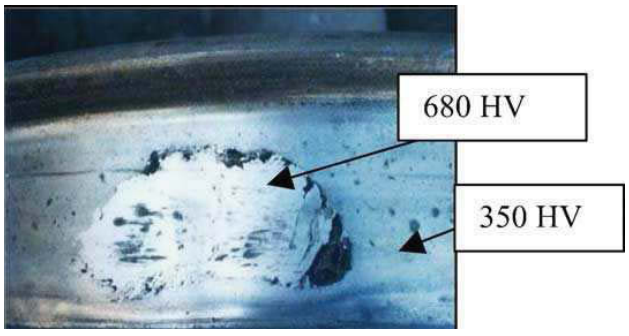

Figure 1.3: Light-gray spot and spalling on the wheel tread surface [5]

1.2.2 Wheel tread shelling

Wheel shelling are deep subsurface shell like defects appearing typically at a depth of about 6-7 mm [9] below the wheel surface. Wheel shelling can be observed on one wheel or on both the wheels of a wheel set at the same time. Through the investigations carried out by many researchers, it has been established that shelling is a consequence of large subsurface cracks. Fatigue rings parallel to the tread surface can be observed on a shelled wheel.

As described in the previous section, martensitic transformation takes place. As these martensitic regions are relatively harder and brittle in comparison to the surrounding material, they are more prone to the initiation of micro-cracks. Under the action of the normal and shear stresses due to the rolling of the wheel on the rail micro-cracks appear predominantly near nonmetallic inclusions.

1.2.3 Tread checking

Tread checking is caused due to the ratchetting response of the wheel material under cyclic loading [10]. Because of the cyclic unidirectional plastic strains, small cracks appear on the wheel surface. Such failure is commonly developed when the wheel rolls on a curved track. These small cracks are developed on the wheel tread. Small cracks join together and cause a material loss from the surface region.

Initiation of surface damage due to surface plasticity is explained in the work by Ekberg and Kaboo [11]. A wheel which is subjected to repeated rolling contact under the condition of high friction undergoes a plastic deformation on and near the surface (shown graphically in **Fig. 1.4**). In the absence of sufficient pressure, residual stresses and material hardening, the accumulation of plastic strain continues till the fracture strain value is arrived. Surface cracks are created through ratchetting. These cracks grow along the plastically deformed grains [12].

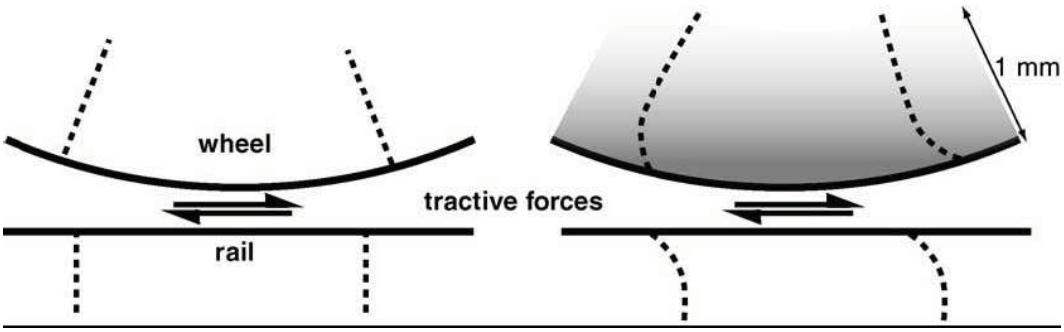

Figure 1.4: Sketch of plastic deformation of the surface material in a railway wheel. The dotted lines indicate the material planes before and after deformation [11]

1.3 Aims

The work is framed around the common problem of RCF encountered in railway wheels. Dynamic and quasi-static finite element simulations are performed using the finite element packages ABAQUS/EXPLICIT and ABAQUS/STANDARD.The preprocessor ABAQUS/CAE is used for model development. In the preliminary stage a dynamic finite element model is developed, in the further stages advanced models are developed to perform a more detailed analysis of the regions in and around the contact patch. Following is the list of all the major tasks (chronologically ordered) covered in this work.

- A dynamic finite element model is developed. This model is capable of finding the dynamic response of the system and determining the macroscopic loading of the wheels.
- A quasi-static finite element model is developed for a detailed examination of the region near the surface of the wheel.
- The quasi-static model is modified to include elastic-plastic material behavior. Deformation near the contact region in the wheel is examined. A damage indicator concept is integrated with the finite element model as an attempt to quantify damage incurred in different cases of loading. Element size and amount of elements are optimized.
- Cyclic loading is performed using a quasi-static finite element model for various cases and combination of cases. The eventual development of the plastic zone and damage indicator variable are compared for different cases. The validity of the

shakedown concept is verified by performing cyclic loads in a wide rage of normal loads and traction coefficients. An attempt is made to predict the service history before a crack initiates in the wheel.

CHAPTER 2

Modeling and simulation

The railway system has become very advanced and complex hence the research in this area has gained importance. A lot of work is going on in different research groups throughout the world. Because of high costs involved and the large amount of time required, the conventional experimental tools are not sufficient to cater the needs of today's research.

Investigations on unconventional components like independently rotating wheels, inclined wheels, slip controlled wheel sets, active suspensions and car body tilting etc. are very important tools but require a detailed analysis of the wheel-rail system. A very useful introduction to the mechanical concepts in the wheel-rail scenario has been given in the work by Zerbst et al in [13].

Because of the uncountable number of loading situations that a wheel-rail system undergoes, modeling and simulation emerges as a very sufficient tool to be employed in the field of wheel-rail contact mechanics. The numerical codes used for developing the model and carrying out the simulations can be broadly classified under two categories. The first one includes the multi-body system dynamics (MBS) programs and the second includes the finite element method (FEM).

Despite of the agility offered by these modern computing tools, the role of classical theories, analytical methods and experimental results can not be ignored as these are the building blocks for the modern computing tools.

2.1 Contact mechanics

If we go into the backward mathematics of a failure, we will realize that every failure problem must be investigated from the very basic level. The failures are a result of the local stress and strain components in the body. In the case of a contact these stresses and strains depend on the nature of the contacting bodies, and of course on the applied loads. Depending on the surface properties of the bodies, the contact may be smooth or rough. The material properties of the contacting bodies determine if it is elastic or an elastic-plastic contact. The geometry of the contacting bodies determines the shape of the contact patch. This patch may be defined as a point or a line contact but in reality it is always circular or elliptical contact. The size of the contact patch also depends on the load and the geometry and material properties of the contacting bodies. A useful reading for understanding the basics of contact mechanics is [10]. Not to be forgotten, weather conditions and foreign agents like rain water also play an important role in determining the fate of a contact.

In 1881 Hertz [14] proposed a theory giving a solution to the contact problem between two elastic bodies with smooth surfaces (For further details on Hertzian and non-Hertzian contact, the reader is referred to the section 2.1.1 in this work.). After the recognition of this solution all the contact problems have been classified under two categories. Contact problems where friction and plasticity comes into play are named as non-Hertzian contact problems and the others as Hertzian contact problems. The geometry of the contacting bodies is also a factor in deciding if the contact is Hertzian or not, a line contact is classified under non-Hertzian problem whereas a point contact between two bodies is classified as Hertzian contact.

One of the first models of rough contact(Contacts involving non-firctionless surface combinations) between elastic bodies was developed by Greenwood and Williamson [15]. This model used the contact solution provided by Hertz [14] in 1881 . Later in 1997 Greenwood [16] analyzed the solution of Hertz and proposed mathematical solutions to calculating the area of contact, contact pressure and the deformation in the contact region.

A lot of work has been done in order to understand and to generate more interpretations from the original theory of Hertz [10], [17], [18] .

2.1.1 Hertz theory - application in wheel-rail contact problems

In 1881 Hertz [14] made the investigation of the deformations produced when two glass lenses were pressed together. Through his investigation Hertz proposed an expression for

the distribution of contact pressure in an elliptic contact area whose axes have the length 2a and 2b. The Hertz's pressure distribution is an ellipsoidal one,

$$p(x,y)=p_0(1-(x/a)^2-(y/b)^2)^{1/2},$$

where p_0 is the maximum contact pressure. If the total load applied is P, the value of p_0 is

$$p_0=\frac{3P}{2\pi ab}$$

The Hertz solution is based on the following assumptions

- Elastic deformations
- Frictionless contact
- Continuous and non-conforming surfaces. An example explaining the difference between conforming and non-conforming surfaces is given by Põdra and Anderson in [19]
- Each body can be assumed as an elastic spherical half space
- The contact area is small compared to the dimensions of the contacting bodies
- Only small strains come into play

The Hertz theory is widely accepted by the scientists working in the area of wheel-rail contact problems [20], [21], [22], [23]. Groups working with the most conventional tools like ultrasonic techniques also turn back to the Hertz concept for the verification of their results [24]. The Hertz concept is also used as a technique for quantifying the surface damage [25].

Some theories exist for solving the problem of contact involving friction. For example the work by M. Andersson [26] describes a method to solve the elastic contact problem involving friction.

2.1.2 Rolling contact

The first attempt to understand and to propose a solution to the problem of rolling contact was done by Carter in 1926 [27]. He proposed his famous two-dimensional theory for the rolling contact between a wheel and a rail. The theory assumes the wheel as a cylinder and the rail as a half space. This theory gives useful results regarding the sliding of the wheel during acceleration and braking. Frictional dissipation can also be calculated by

Carter's two-dimensional theory. However this two-dimensional theory fails to capture the affect of lateral forces which is very important for simulating the vehicle motion.

De Pater worked on Carter's theory and solved it for a special case where there was no slip at all in the contact area. He arrived at an expression where the tangential force at the contact zone bears a linear relation to the rigid slip in the contact patch. This is commonly know as the linear theory which has found application in the concepts developed by Shen, Hedrick and Elkins [28] and for a simplified concept [29], [30].

Kalker [31] took up this work of De Pater at this point and developed it further. He generalized the work by de Pater for a case where small rigid slip exists, the contact area is an Hertzian ellipse and the rolling direction is in one of the axial directions of the contact ellipse.

Kalker, in 1979, developed an algorithm called DUVOROL. This was the first reliable program which was capable of handling all possible rolling contact problems involving two bodies having identical elastic properties touching each other according to the Hertz theory .

Later, in 1982, DUVOROL was replaced by a newer algorithm called CONTACT. This program had the capability to deal with all contact configurations that could be described by half-spaces.

In 1984 Kalker, with the help of the algorithm CONTACT, further developed and generalized his linear theory to include non-elliptic contact patches also.

For a complete report on all the contact algorithms mentioned above, the reader is reffered to the work of Kalker [32]. Wheel-rail contact specific theories have been discussed in detail in [33].

2.1.3 Cyclic loading of an elastic plastic material

The response of a cyclically loaded material depends on the material properties as well as on the applied load. **Fig. 2.1** shows the possible response that a material may exhibit when loaded cyclically.

Under the conditions of very low contact pressure the material does not undergo any plastic deformation and hence exhibits only a reversible deformation.

Under the conditions of repeated loading and elastic-plastic material behavior, the material can reach a state of equilibrium where no further plastic strains accumulate. Under this configuration of residual stresses and loads, the material is said to have reached the state of shakedown.

There are two recognized theorems of shakedown [34]. The first theorem, which gives a lower bound to the shakedown limit describes a configuration in which the system of cyclic loads never allows the stresses to surpass the elastic limit of the material (i.e. condition for elastic shakedown), is called the statical theorem.

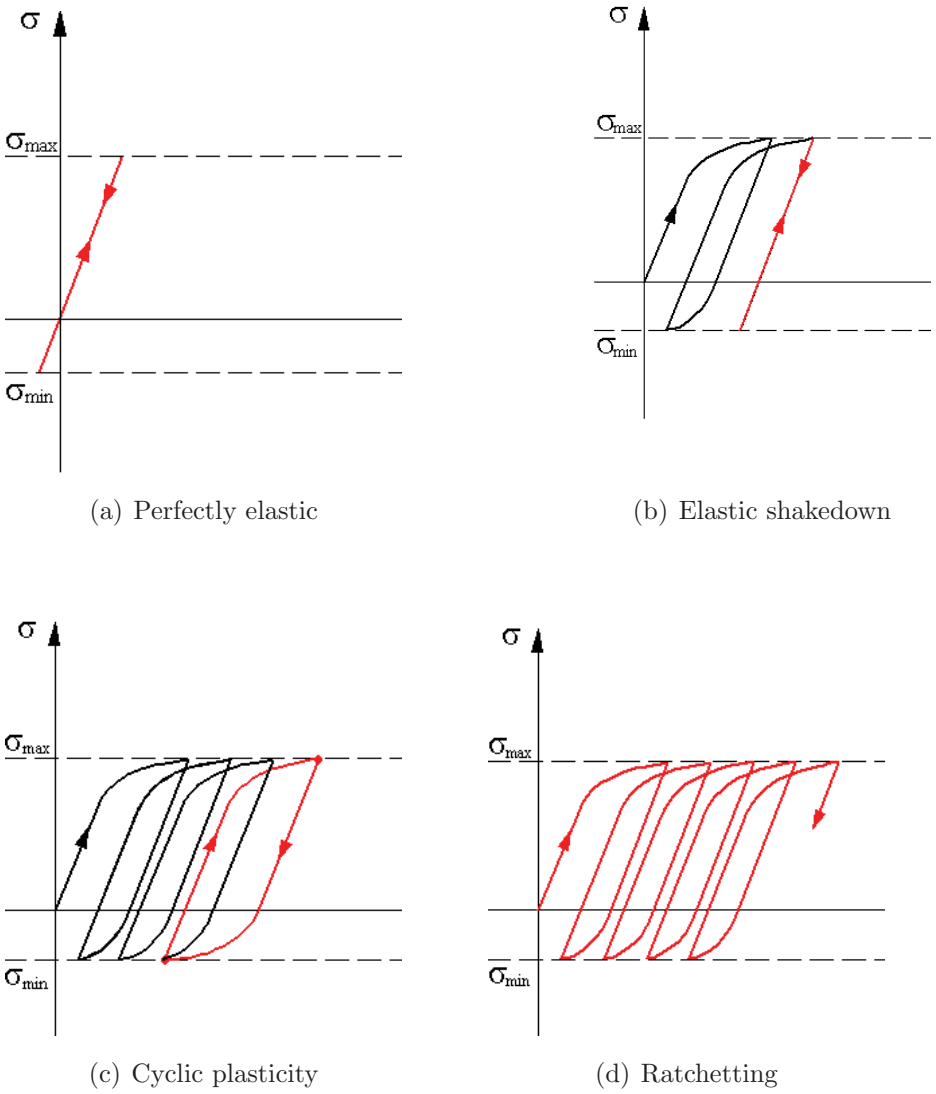

(a) Perfectly elastic

(b) Elastic shakedown

(c) Cyclic plasticity

(d) Ratchetting

Figure 2.1: Structural response to cyclic loading

The second theorem describes the upper bound to the ratchetting threshold and is known as the kinematical theorem. According to this theorem, ratchetting will take place if there exists a kinematically acceptable mechanism of ratchetting where the rate of work done by elastic stresses due to the loading exceeds the rate of plastic dissipation.

The application of shakedown principles in analyzing rolling contact fatigue is discussed in great detail in the work by Johnson [35]. Some further approaches for calculating initial yield and shakedown loads both in two and three dimensions are discussed by Boulbibane and Collins [36] and by Ertz and Knothe [37].

In the case when there are no frictional forces acting between the contacting surfaces, sliding, rolling and mixed rolling and sliding possess the same stress state and hence exhibit the same response to cyclic loading. Conversely in the cases where friction comes into play, the shakedown limit is highly controlled by the friction coefficient, or more precisely, the traction coefficient μ. The shakedown limit is obtained by superposing the stress field caused by traction and the stress field due to the normal load.

Traction is referred to the special case of friction when one of the contacting body is a drive member and the other is the surface on which this drive member moves. A typical example is a driven wheel (drive member) moving on the rail. Traction force is the forward driving force which moves the driven body. The traction coefficient μ = Q/P where Q is the traction force and P is the normal load.

Shakedown is governed by the maximum value of the shear stress component t_{23} (2 is the normal to the rail surface and 3 the longitudinal rail direction). At lower values of μ the maximum value of the shear stress component t_{23} is reached at a point beneath the contact surface, at higher values of μ, the shear stress component t_{23} attains the maximum value at the surface itself. In this case the shakedown limit is given according to the Tresca equivalent stress. The maximum shear stress P_0^s is related to the yield stress k and the traction coefficient μ by the following relation

$$P_0^s = k/\mu,$$

In **Fig. 2.2** two non-dimensional parameters, the load factor (p_0/k) and the traction coefficient (μ = Q/P) are plotted to graphically illustrate various load conditions. p_0 is the maximum Hertz (i.e. elastic) contact pressure, k is the yield stress of the material in simple shear, Q is the traction force and P is the normal load. Such a plot is known as a shakedown map. In this figure , the load factor is plotted on the vertical axis and the traction coefficient is plotted on the horizontal axis. The horizontal line A represents the upper bound to the elastic shakedown limit, curve B and C are the upper bounds to the ratchetting limit, curve D is the lower bound to the elastic shakedown limit and the curve E represents the elastic limit.

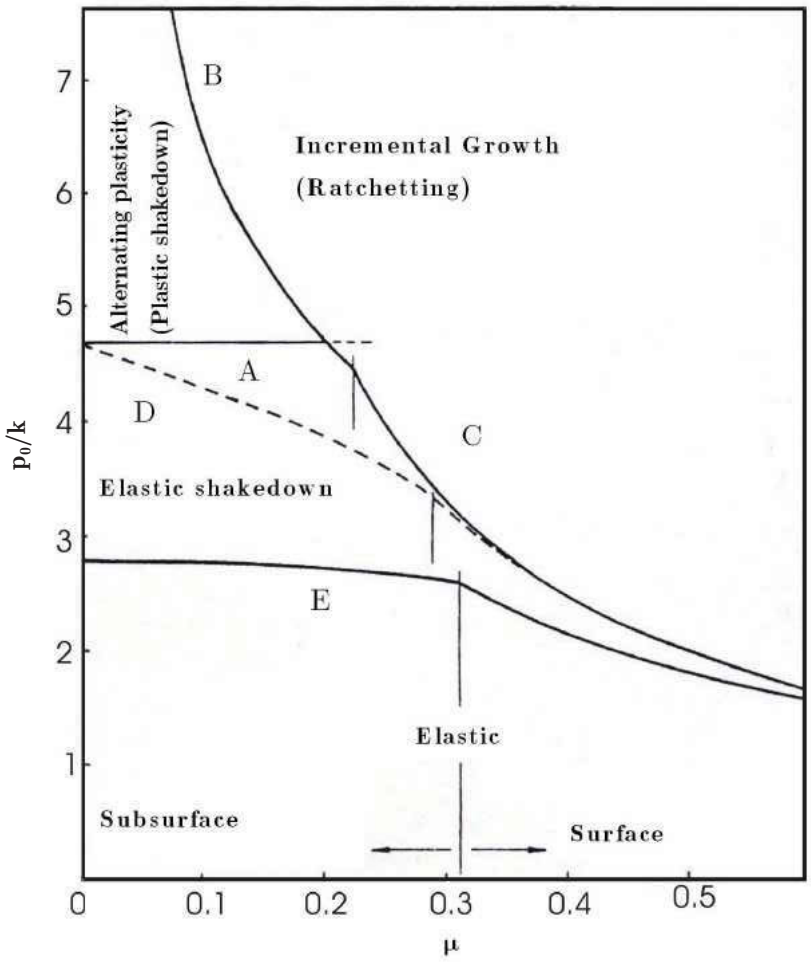

Figure 2.2: Shakedown map for point contacts

2.2 Modeling methods

To study the wheel-rail contact problem, a lot of attempts have been made to break down the problem into small modules and look at the different aspects of the problem individually. The use of computers has given a new face to the term modeling. In the past, to simplify a problem, a complex mechanical system was shaped into a simple mechanical model and solved analytically. With the advent of high performance computing hardware, highly advanced and efficient computing codes have been developed with which one can model almost any mechanical situation into a mathematical problem and can obtain efficient solutions.

The available computing codes are either based on multi-body system dynamics or finite element codes or a combination of the two. Both, two and three-dimensional models

can be developed using these codes. Today several multi-body system (MBS) dynamics modeling packages are available as ADAMS/RAIL [38], [39], GENSYS [40], NUCARS [41], SIMPACK [42] and VAMPIRE [43].

In this work a comparison is made between the results from MBS package SIMPACK and the results from FEM calculations performed using ABAQUS.

CHAPTER 3

Dynamic Finite Element Calculations in a Purely Elastic Scenario

A three dimensional finite element wheel-rail model is developed. This model is capable of simulating the wheel-rail contact situations for a wide variety of loading cases. The necessary input values for geometrical parameters and velocities are provided by run-technical simulations. The inclination of the wheel to the rail is defined by the roll angle **Roll_RS** that the wheel axis makes with the rail, see **Fig.3.1**. Some of the loadings that can be modeled are pure rolling, acceleration, braking and running over a curve of a given radius. The radius of the curve is defined using the yaw angle **yaw_RS**. See **Fig.3.2**.

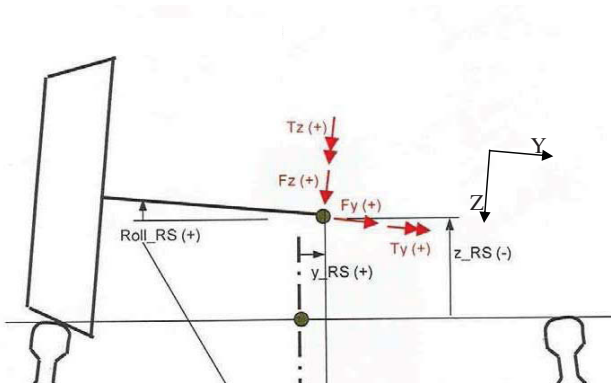

Figure 3.1: Orienting the wheel and the rail - 1 (STS Graz)

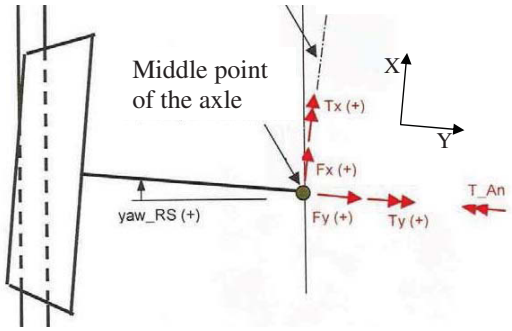

Figure 3.2: Orienting the wheel and the rail - (STS Graz)

In the present chapter a fundamental research work is carried out by performing a finite element analysis which is very different to those encountered in the available literature. The specific case of a wheel with an assigned initial velocity and accelerated by a driving moment is analyzed. Macroscopic loading of the wheel is evaluated by performing finite element calculations on this model.

At this point it is important to mention that the calculations are made taking an elastic material behavior for both the wheel and the rail. The model however, in principle is capable of simulating plastic material behavior also. Plastic behavior is ignored in these calculations to save calculation time. The following section covers the model description in detail.

3.1 The finite element model

The wheel geometry is the standard **UIC ORE 1002**. The **Fig. 3.3** shows the assembled wheel and its individual components.

The wheel is modeled using two parts bonded together using tie constraints [44]. The idea behind making this geometrical modification is to be able to mesh the wheel in an efficient way to reduce the computing time and to run these calculations on a normal PC.

It is assumed that the region of the wheel that is affected due to the wheel-rail contact extends to only a few centimeters below the contact surface. Hence the major part of the wheel is safely assumed to be rigid. **Fig. 3.3** describe the wheel as modeled for these calculations.

(a) W_{Rig} (b) W_o (c) Assembled wheel

Figure 3.3: Wheel geometry in parts and assembled

The total mass of the wheel, **W**, is the sum of the masses of the rigid and the elastic part.

The part of the wheel starting from its center and extending to a radius of 41.14 cm is modeled as a flat disc and is is defined as an analytic rigid body, this part is named W_{Rig}. The part of the wheel lying outside this radius is modeled as a separate part, named as outer ring W_O to which has been assigned elastic material properties.

The total mass of the wheel is 512 kg. The mass of the outer ring is 55 kg. The rest of the wheel mass, which is 457 kg, is assigned to the rigid disc. Since an analytic rigid body acts like a point mass the moment of inertia is also defined separately whose value is 38.6 Kgm^2. A procedure similar to that used for modeling the wheel is adopted for modeling the rail. The standard **UIC 60** rail geometry is broken up into two parts. The interesting part of the rail is named as rail head R_H. The rest of the rail is modeled as a separate part called rail base R_B. The complete rail, i.e., the rail head and the rail base are modeled as elastic. The assembled rail model and the parts comprising it are shown in **Fig. 3.4**

(a) R_H (b) R_B (c) Assembled rail

Figure 3.4: Rail geometry in parts and assembled

For all the elastic regions in the model isotropic elastic properties are assumed.

To attain a more realistic model, a rigid body of weight 7500 kg is attached to the wheel using a dashpot[45] which simulates the dead load contribution from the vehicle M_v.

3.1.1 Material Definitions

In the model, the elastic material is identified with the name "Steel". The properties are tabulated in **Tab. 3.1**.

Table 3.1: Wheel and rail material properties

Elastic behavior (Applicable to both wheel and the rail)	
Property	Value
Density	7800 Kgm^{-3}
Young modulus	2.1E+11Nm^{-2}
Poison's ratio	0.3

These material properties are assigned to the parts R_H, R_B and W_O. The model described is also capable of taking into account plastic materials but elastic material is taken as it simplifies the simulation procedure and remains comparable to MBS results.

3.1.2 Constraints

For assembling the above mentioned parts for a final model, some specific techniques are used. To constrain the two parts of the wheel or the two parts of the rail together, tie

constraints are used. The vehicle mass M_v, is constrained to the center of the wheel using a rigid body constraint [44].

3.1.3 Mechanical Model

Fig. 3.5 explains the mechanical model. In this model, the rail R is fixed to the ground. The wheel W rests on the rail. The coefficient of friction μ_f between the wheel and the rail is set to 0.3. The horizontal and the vertical oscillations in the system are damped out using a damper D1 acting in the vertical direction and a damper D2 acting in the horizontal direction. The damper D1 has a damping coefficient of $1.2\text{x}10^6$ Nsm^{-1}. One end of D1 is connected to the wheel and the other end is fixed in vertical direction. The damper D2 has a damping coefficient of $1.2\text{x}10^9$ Nsm^{-1}. D2 acts between the wheel and the vehicle M_V(a rigid body of mass M = 7500kg). A spring S2 with a spring constant of $2.0\text{x}10^8$ Nm^{-1} also acts between the wheel and the vehicle in horizontal direction. The spring and the dampers D1 and D2 are depicted in the figure. The two dampers together are named as D.

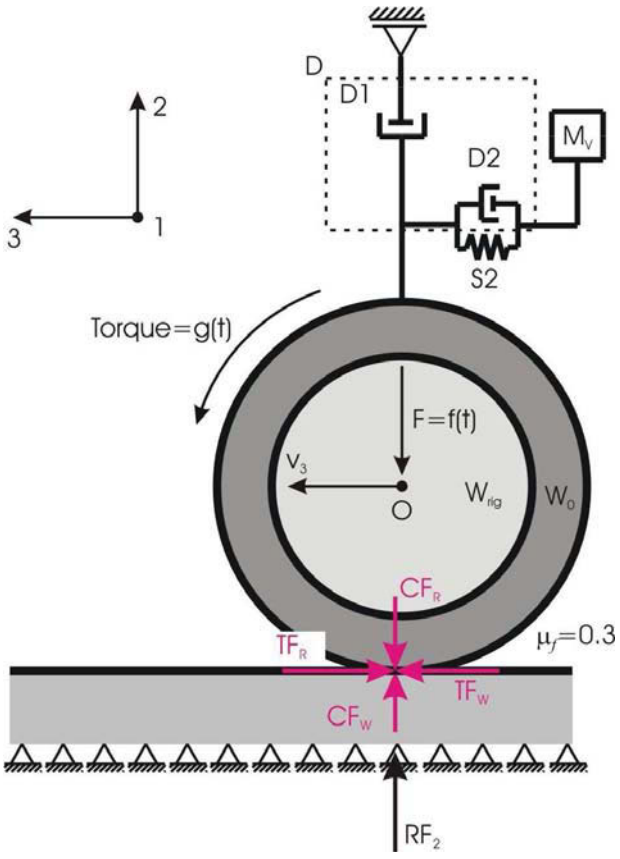

Figure 3.5: The mechanical model of the wheel-rail system

The rail head and the rail base are connected through a tie constraint. W_{Rig} is connected to W_O and the lower point of D1 using a pin type rigid body constraint. The wheel starts moving in 3 direction with an initial translation velocity of $v_{3i} = 16.67$ ms^{-1} and a rotational velocity of $v_{R1i} = 39.04$ rads^{-1}. A load f(t) and torque g(t) act on the wheel. The vertical load (acting in the negative 2 direction) starts acting at time t = 0 with a starting value of 10 percent of the maximum load. This load attains its maximum value at t = 0.01 sec and retains this value thereafter. The maximum load is f(0.01) = 75000 N. A driving moment starts acting as soon as the vertical load attains its constant value. The driving moment increases linearly for a time interval of 0.01 sec (i.e. the starting value g(0.01) = 0 Nm and grows linearly to a value of g(0.02) = 5700 Nm) and thereafter maintains a steady value. The above situation can be mathematically written as follows:

$$f(t) = \begin{cases} 7500 + 6750000t & \text{if } t \leq 0.01 \\ 75000 & \text{if } t > 0.01 \end{cases}$$

and

$$g(t) = \begin{cases} 0 & \text{if } 0 \leq t \leq 0.01 \\ 570000t - 5700 & \text{if } 0.01 < t \leq 0.02 \\ 5700 & \text{if } t > 0.02 \end{cases}$$

3.1.4 Meshing

3.1.4.1 Optimizing the mesh

The standard geometry of the wheel and the rail is divided into two parts each keeping in mind the need to minimize the calculation time without losing the level of precision in the results. The most important factor in deciding the total calculation time is the size of the smallest element in the whole model. This element size must produce an affordable computing time and a sufficient level of accuracy. The second fact which is to be kept in mind while optimizing the computation costs of the model is the number of elements, bearing a linear relation with the total calculation time. Partitioning the geometry along required planes or edges could, to a great extent, control the problem of most critical element. Some of the unimportant geometry details are ignored to increase the efficiency of the model.

Tie constraint is a very useful tool when it comes to reducing the number of elements in the model. The power of this technique lies in the fact that the two surfaces in the tie constraint can be assigned nodes for creating a finite element mesh independently (which is not possible across a partition). After some preliminary mesh studies we have safely

concluded that for our model the best results can be obtained if we decrease the number of elements (mesh density) across the tied surface by a factor of two.

We have been able to drastically control the number of elements using this technique. Reasonable results are obtained with an element size of 3x3mm in the contact region. The mesh can be seen in **Fig. 3.6**. ABAQUS/CAE [45] is taken as the preprocessor. The jobs are calculated using ABAQUS/EXPLICIT [45].

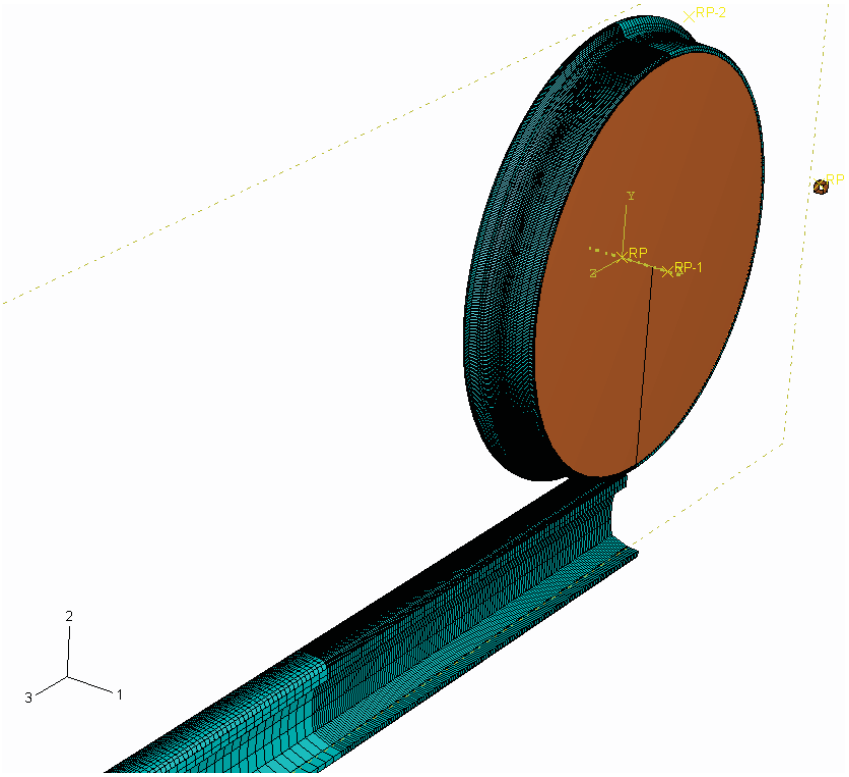

Figure 3.6: Meshed Model

3.1.5 Boundary conditions and coordinate system

The tangential and the normal behavior at the wheel-rail contact are defined using the contact definitions and the boundary conditions. A penalty frictional formulation is defined between the wheel and the rail. The friction coefficient is taken to be μ_f=**0.3**. The boundary conditions applied on the wheel are such that it is allowed to translate and rotate along the rail and is free to move in the vertical plane. The rail has no degree of freedom at its base, this implies that the bedding is rigid. The coordinate system is depicted in **Fig. 3.7**.**Tab. 3.1.5** tabulates the global directions.

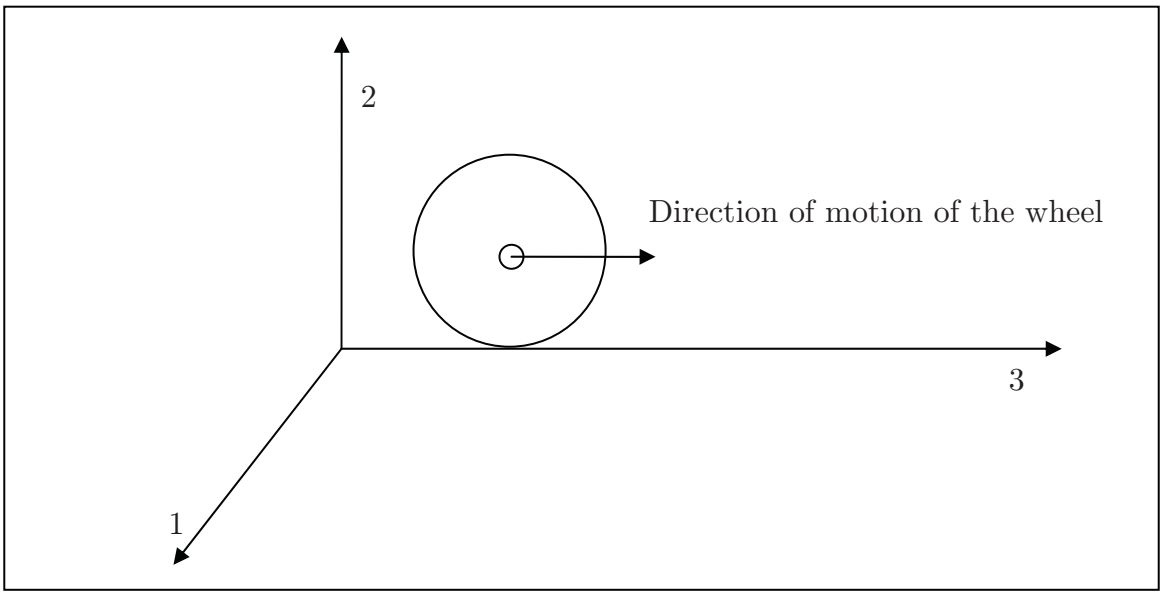

Figure 3.7: Coordinate System

Global direction	Coordinate name
Lateral	1
Longitudinal	2
Normal	3

Table 3.2: Coordinate system definition.

3.1.6 Calculation steps

The whole calculation is carried out in two simple calculation steps. The initial conditions are set at time $\mathbf{t}=0^+$. All the initial positions, boundary conditions and fields are initialized in this step. The second step, the loading step, lasts for a period of 0.05 seconds. The loads and the driving moment are applied during this step.

3.1.7 Results

The wheel-rail contact model described in the above sections is calculated using ABAQUS/EXPLICIT [45]. The interesting quantities are plotted into contour plots at a time instance t=0.03. At this time instance the loading attains its stable value and the oscillations in the systems are damped out, i.e. an almost steady state is reached as can

be seen in the development of the contact slip rate between the wheel and the rail, see **Fig. 3.8**. The first contact is at time 0.0 sec. After 0.03 sec of rolling, a constant slip rate is obtained. The red markers show at which position and the calculation step time the wheel was contacting the rail.

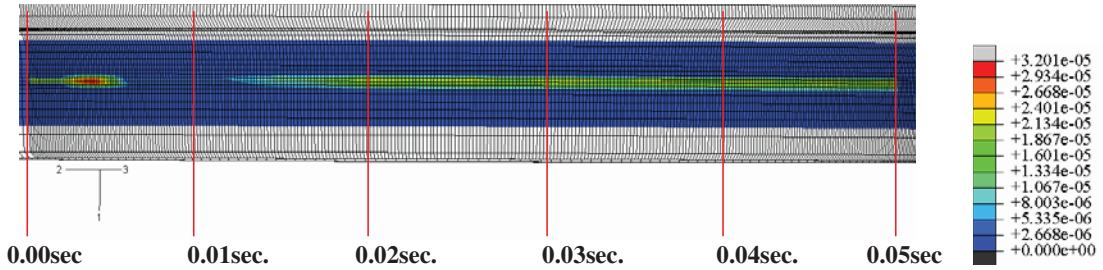

Figure 3.8: Magnitude of the contact slip rate FSLIPR at slave nodes on the wheel surface after contact

In **Fig. 3.9** a contact patch on the wheel surface is analyzed. The direction of motion is such that the first contact point(leading end) of the wheel is at the bottom of the figure and the top of the figure is the last contact point(trailing end) for a contact patch. The red elliptical ring shown in the sketch is the assumed contact patch.

The contour showing the magnitude of the contact slip rate FSLIPR $= \mid \underline{\dot{S}} \mid$ at the nodes of the wheel during contact depict a higher slipping at the leading end of a contact patch.

$$\mid \underline{\dot{S}} \mid = \frac{2(\mid \underline{\nu}_{P_{wheel}} - \underline{\nu}_{P_{rail}} \mid)}{\mid \underline{\nu}_{P_{wheel}} + \underline{\nu}_{P_{rail}} \mid}$$

Slip velocity is defined as the difference between the circumferential and the translational velocity of the wheel (In this work the translational velocity is assigned to the rail instead of the wheel).

$$\mid S_v \mid = \mid \underline{\nu}_{P_{wheel}} - \underline{\nu}_{P_{rail}} \mid$$

Total slip S and the slip velovity S_v is related to each other according to the following mathematical formulation:

$$S = \int_0^{t_c} \mid S_v \mid dt$$

where t is the time and t_c the total time of contact. The velocities are provided by ABAQUS and include both the kinematics and the deformation state.

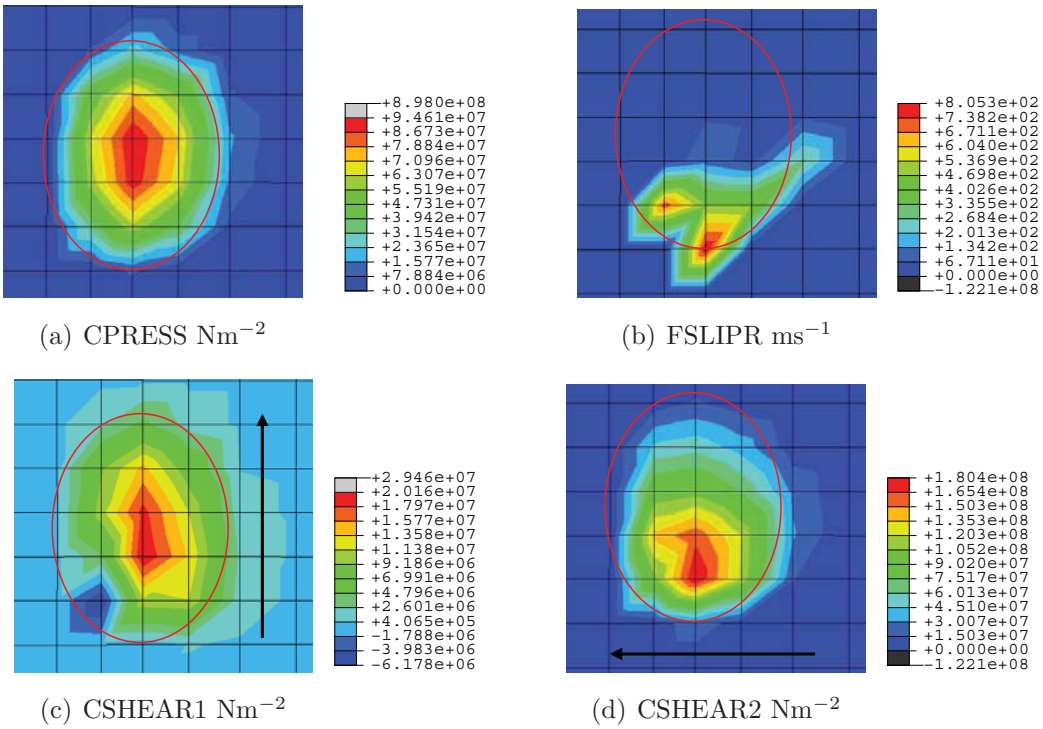

(a) CPRESS Nm^{-2} (b) FSLIPR ms^{-1}

(c) CSHEAR1 Nm^{-2} (d) CSHEAR2 Nm^{-2}

Figure 3.9: Contact variables as the wheel surface

The contours CSHEAR1 and CSHEAR2 represent the friction shear stresses in lateral and longitudinal directions respectively. CSHEAR2 shows a trend of stress concentration in the rear end of the contact patch.

Fig. 3.10 represent the stress components developed in the wheel during a rolling contact. S11, S22 and S33 are the stress components in lateral, normal and longitudinal directions, respectively. SMISES and SPRESSURE are the Mises equivalent stress and hydrostatic pressure . **Fig. 3.10** shows a cut through the wheel to represent the distribution of stress components in the wheel body. The 2 direction is the depth into the wheel body. The total depth of the cut is approximately 12mm. The contour for the Mises stress shows a stress concentration a few millimeters below the contact surface. The plots in **Fig. 3.11, 3.12, 3.13 and 3.14** represent various reaction forces, energy components and other relevant variables. All the reaction forces (hence the corresponding acceleration components) seem to stabilize after 0.03 seconds. The reaction forces are calculated at the rigid bedding of the rail.

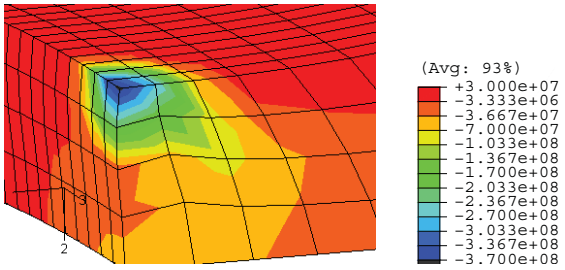

(a) S11 Nm^{-2}

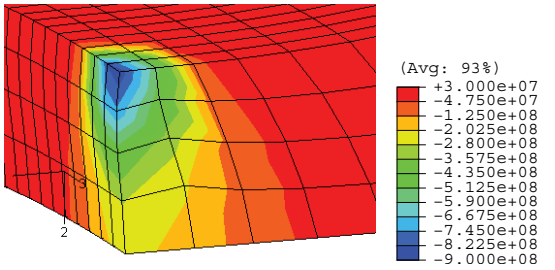

(b) S22 Nm^{-2}

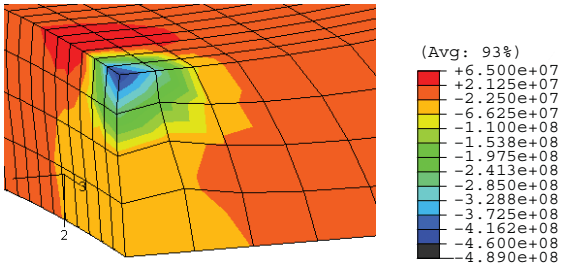

(c) S33 Nm^{-2}

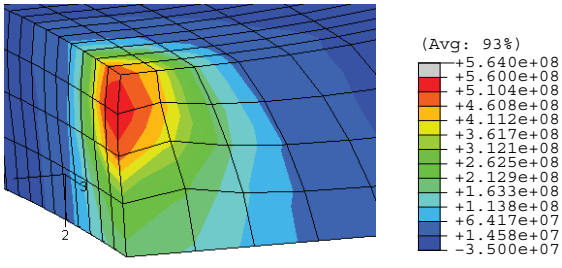

(d) SMISES Nm^{-2}

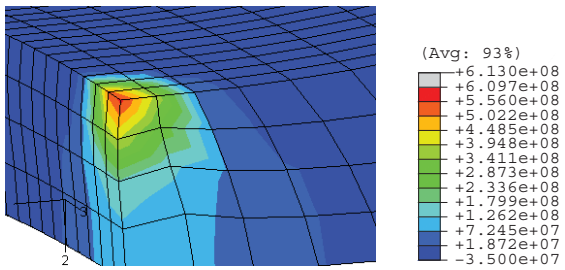

(e) SPRESSURE Nm^{-2}

Figure 3.10: Stress components in the loaded wheel

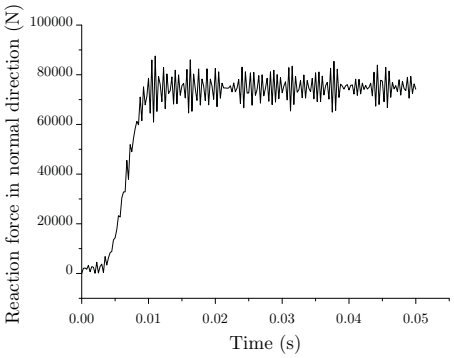

(a) RF - Global normal direction

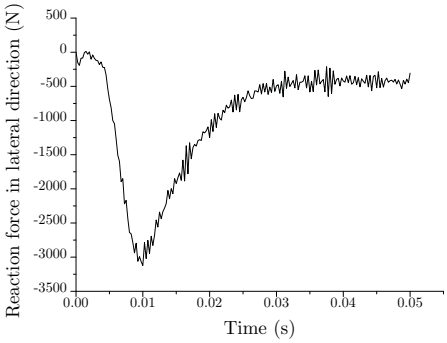

(b) RF - Global lateral direction

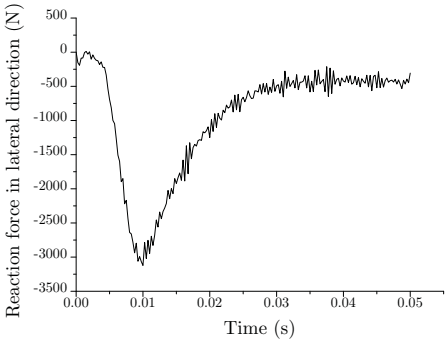

(c) RF - Global longitudinal direction

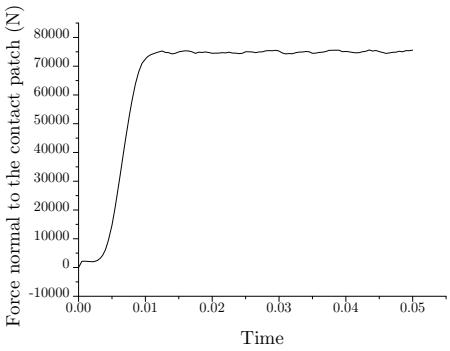

(d) F-Total - Normal direction to contact zone

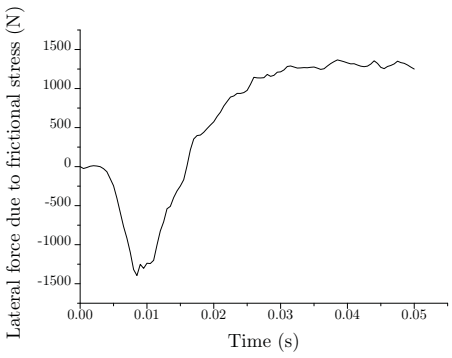

(e) F-Total due to frictional stress in contact zone (in global lateral direction)

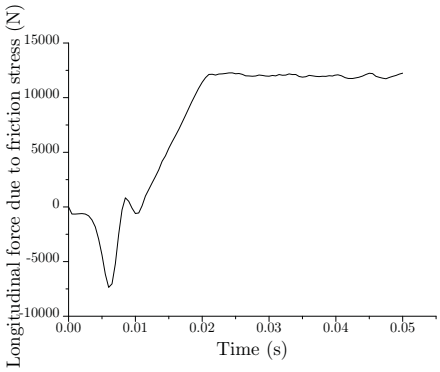

(f) F-Total due to frictional stress in contact zone (in global longitudinal direction)

Figure 3.11: Reaction forces in the system

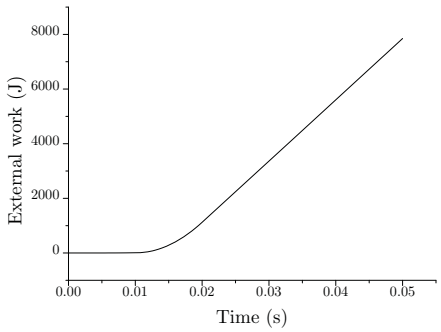

(a) External work

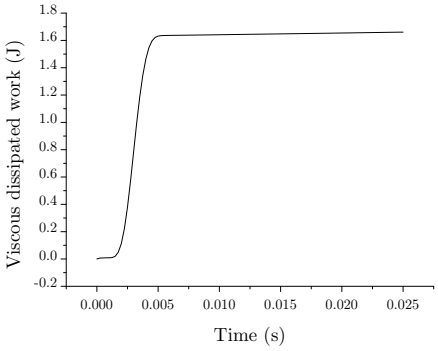

(b) Viscous dissipated work

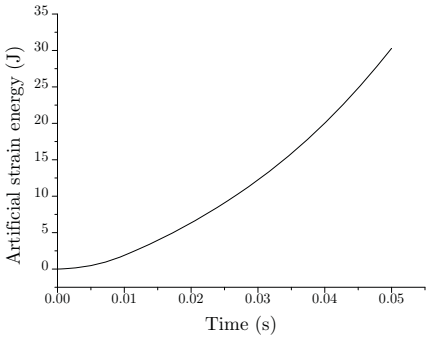

(c) Artificial strain energy

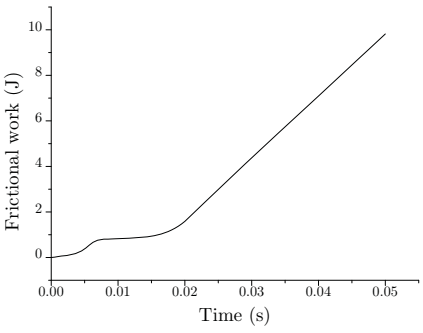

(d) Frictional dissipated work

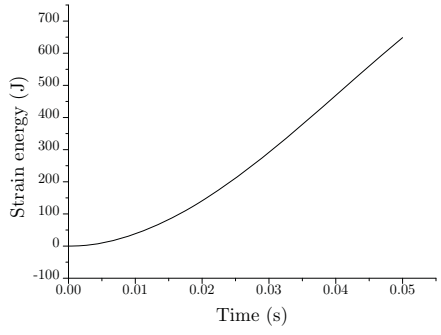

(e) Internal strain energy

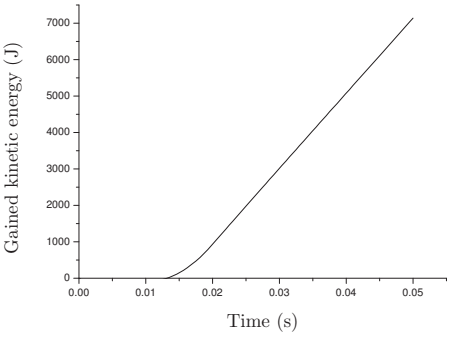

(f) Kinetic energy

Figure 3.12: Energy balance in the system

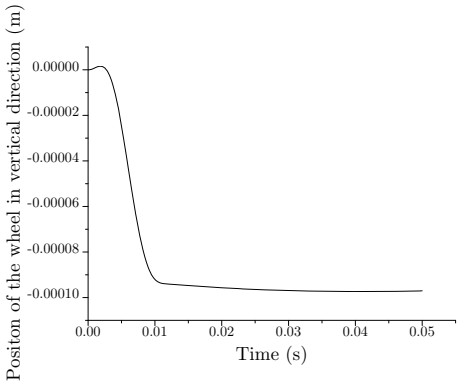

(a) Displacement in normal direction

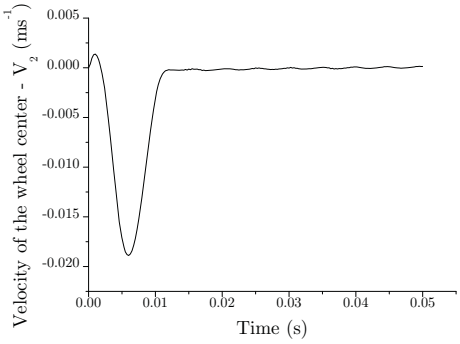

(b) v_2 - Velocity in normal direction

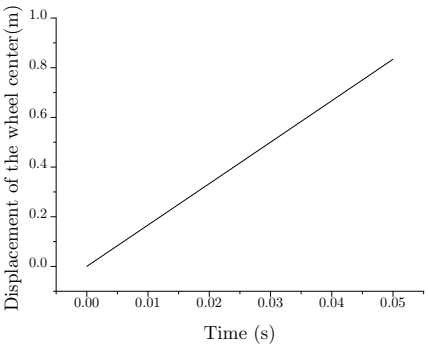

(c) Displacement in translational direction

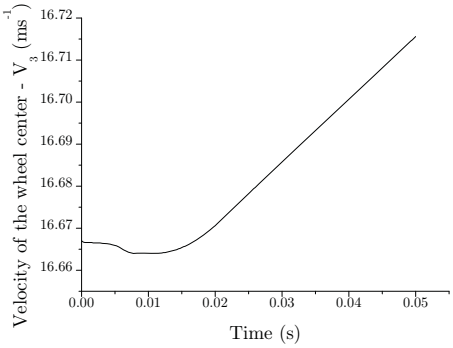

(d) v_3 - Translational velocity

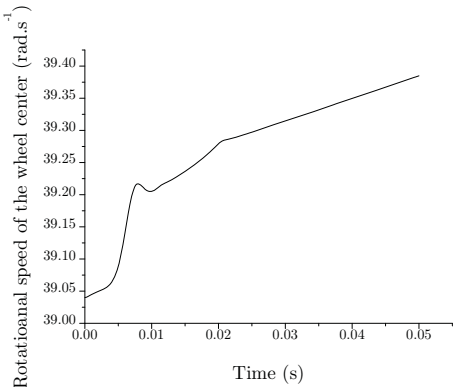

(e) Rotational speed

Figure 3.13: Velocity and displacement components of the wheel

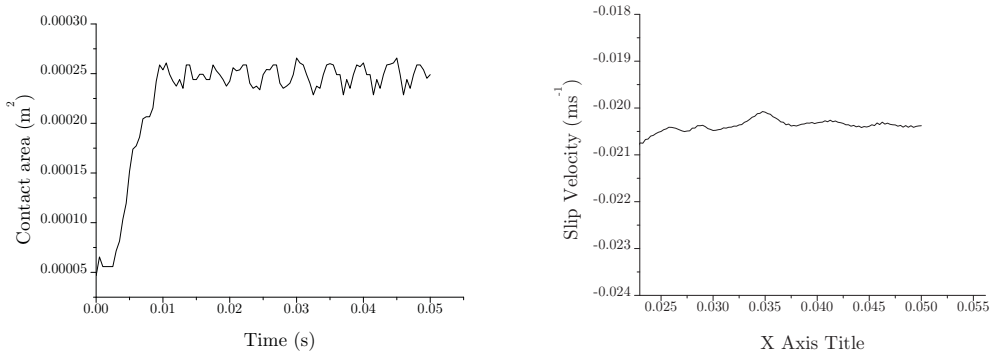

(a) Contact area (b) Slip Velocity

Figure 3.14: Contact area and slip velocity at the wheel surface

The plots in **Fig. 3.12** depict the energy balance of the system. The total external work is a sum of the viscous dissipated work, artificial strain energy, frictional dissipated work, internal strain energy and the kinetic energy of the system.

The definitions of these forms of energies are as following:

External work is the work done by the external forces and moments acting on the system.

Viscous dissipated work is the work done by the viscous dissipation effects. In the current model, the sources of viscous dissipation are the bulk viscosity of the material, material damping and the dashpots.

Frictional dissipated work accounts for the energy loss due to the friction between the wheel and the reil.

Internal strain energy is the sum of the energy in the the system due to elastic and plastic strains.

It is noticed that sometimes the mesh has a pattern of alternating trapezoids, which indicate that hourglassing is propagating through the mesh. Hourglassing can be sometimes observed in the form of a deformed mesh, especially at corners. The energy associated with these deformations is termed as the artificial strain energy. Normally it constitutes a very small part of the total energy in the system.

The system is set into motion under the influence of an external work, a part of the work is converted into the kinetic energy by virtue of translation and rotation of the wheel. This is the gained kinetic energy.

The values obtained from the FEM calculations are compared to the values obtained from MBS calculations performed at STS. The comparison is tabulated in **Tab.3.3**. Refer to **Fig. 3.1 and 3.2** for the context to the quantities tabulated in the table.

Table 3.3: Comparison of input values provided by STS and results calculated by MCL.

Wheel set	Units	Siemens	MCL
y_RS	mm	0.15	0.15
z_Rs	m	-424.85	-424.85
Yaw angle	rad	0.00001	0.00001
Roll angle	rad	-0.00001	0.00001
Wheel angular velocity - w_{w3}	rad /sec	-52.232	-52.232
Reaction forces and moments at the bearings			
Fx	N	13474.8	14385.7
Fy	N	-657	-471.852
Fz	N	76987.4	80670
Tz	Nm	10124.5	10791.6
Driving moment - T_an	Nm	-5726.2	-6115.09
Values recorded at contact surface			
Tx	N	-13474.8	-14392.1
Ty	N	-2006.7	-2295.59
N	N	81163.9	80568.4
a	mm	5.65	5.8
b	mm	8.02394	10
yw	mm	-1.8	-1.0
yr	mm	1.8	-0.7

The model is capable of simulating an accelerated as well as a braked wheel starting with an arbitrarily chosen initial velocity. The obtained results are seen to be in harmony with those obtained from SIMPACK calculations carried out at STS. This model is the basis of all the advanced models that are developed in the later stages of this work.

This wheel-rail model can be applied in analyzing various scenarios involving a wheel-rail contact. The main advantage of this dynamic model is that it is able to account for irregularities in the track, switches or wheel flats. Since the deformations and oscillations of the wheel are an inherent result of such a model, e.g. the vibrations of the wheel leading to excitation of noise can be extracted from results of this model. The model can find applications in analyzing the impact of a rail on a crossing or a wheel in a curve.

Since the whole geometry of the wheel and the rail can be modeled with elastic material behavior, also waves moving in the wheel and the rail are calculated. Since the whole wheel can be modeled without using a rigid body, accepting longer calculation times, investigations involving noise oscillations, vibrations and also ovalization of wheels are also possible.

The limitation of this model lies in the large calculation time. The model takes approximately two days for completing one calculation on a standard PC of the year 2006. This makes the model impractical for cyclic analysis. For this reason a quasi-static model is developed, see **Chap. 4**.

CHAPTER 4

Load Analysis at Contact Surface

The basic model used in the dynamic calculations in the previous chapter is modified for the execution of the load analysis. The load analysis in this chapter is aimed at determining the stresses, strains and damage in the contact region.

In contrary to the original full model, the modified model is relatively small in size. It consists of only a small slice from the wheel and a corresponding length of the rail. Major changes in constraints and boundary conditions are also implemented in the model. The case of a wheel running on a straight track and in a curve is analyzed. Calculations on a small section of the wheel and the rail are carried out using a quasi-static model which is intended to be a sub-model of the dynamic model.

This dynamic simulation can be done using finite-element software e.g. ABAQUS/Explicit or a multi-body simulation software like SIMPACK. In the case at hand the data from the SIMPACK software provided by STS is taken for the description of the kinematics of the model. The model geometry, mesh and other model details have been created using ABAQUS/CAE. The final analysis is carried out with ABAQUS/Explicit.

4.1 Model geometry

The basic wheel geometry in this quasi-static model is the same as that in the dynamic model i.e. the UIC ORE 1002. The difference lies in the fact that instead of creating a

full wheel by revolving the section outlines by 360°, a small slice is created by revolving the geometry by an angle of 5.5°.

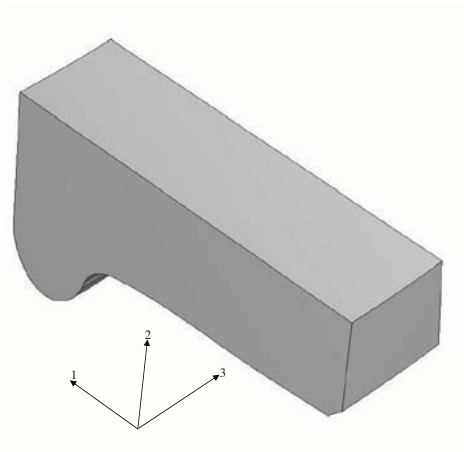

(a) Part of the wheel modeled as elastic

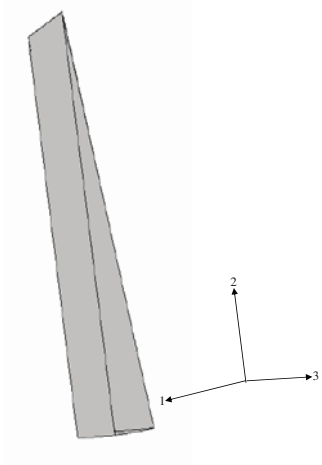

(b) Part of the wheel modeled as rigid

Figure 4.1: The two parts of the modeled wheel

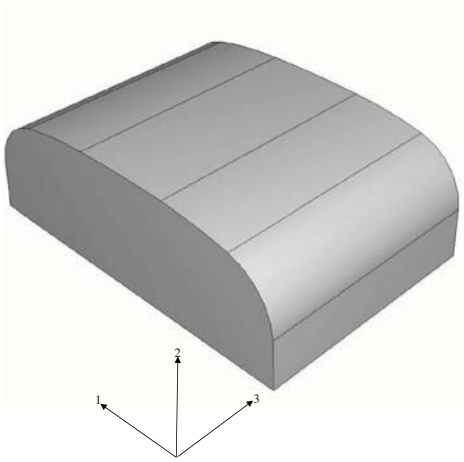

(a) Part of the rail modeled as elastic

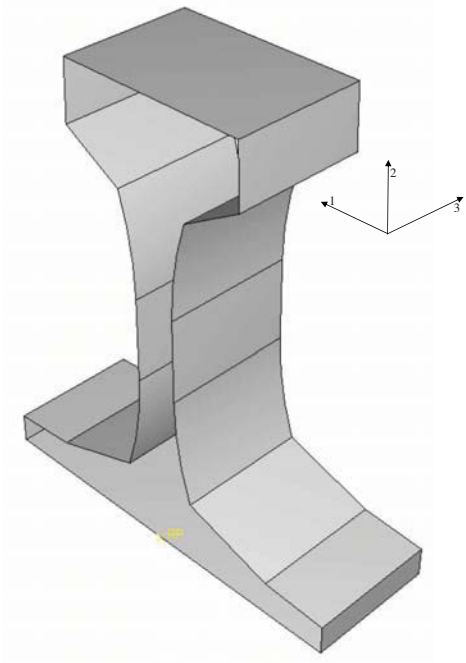

(b) Part of the rail modeled as rigid

Figure 4.2: The two parts of the modeled rail

4.2 Defining the contact point and the loading

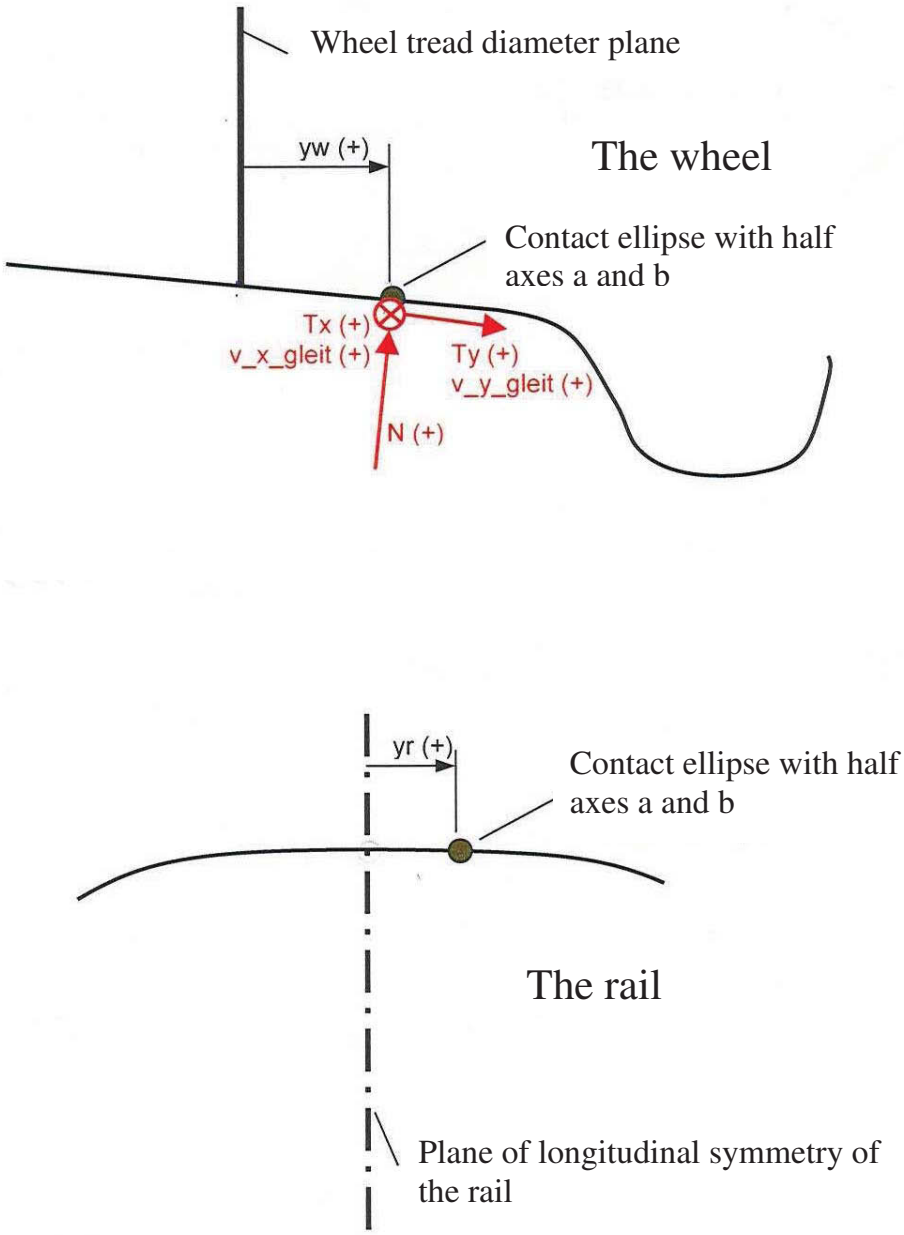

Figure 4.3: Definition of the contact point (STS Graz)

The position of the contact point on the wheel surface is defined by a distance yw of the contact point from the wheel tread diameter plane. The value of yw is conventionally

taken to be positive when the ellipse lies between the flange and this plane, else it is taken to be negative. Similarly the position of the contact patch on the rail is defined using a variable yr which is measured taking the plane of longitudinal symmetry of the rail as the origin. Refer to **Fig. 4.3** for a detailed sketch.

The angular position of the wheel is defined by the yaw angle yaw_RS and the roll angle Roll_RS. The angle definitions are schematically shown in **Fig. 3.1 and 3.2**

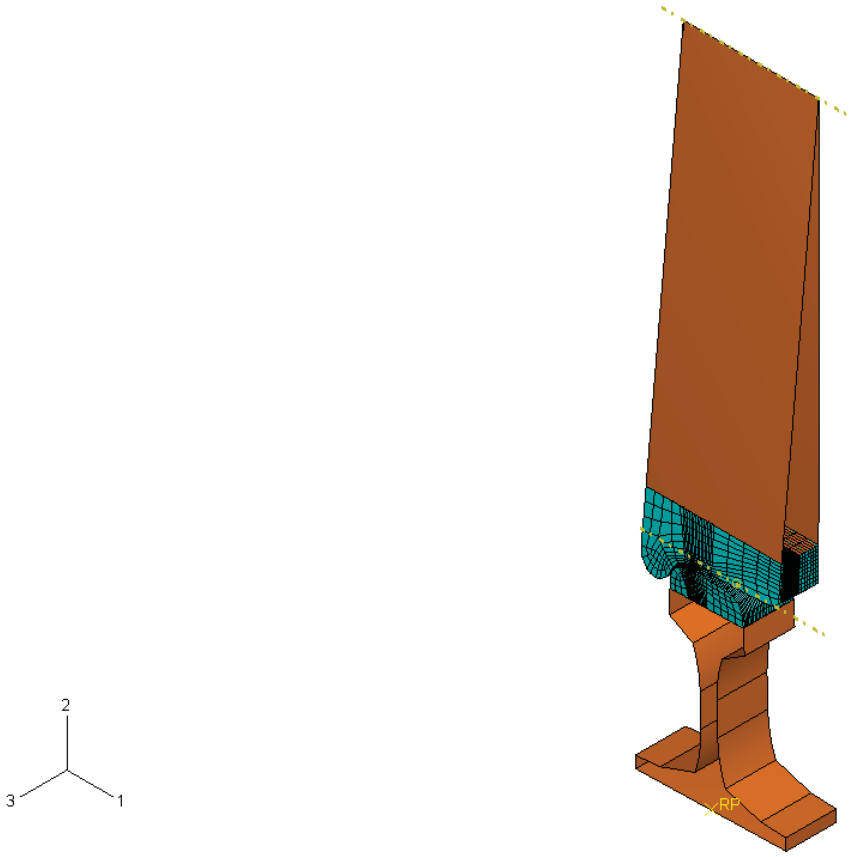

Figure 4.4: Details of the rail and wheel geometry

4.3 Meshing the finite element model

The model is meshed in a way that the contact regions on the wheel and the rail have an element size of 1 mm. The rest of it is somewhat coarsely meshed to optimize the calculation. **Fig. 4.4** shows the complete meshed model. The part of the model that appears not meshed is actually the analytic rigid part of the model.

Table 4.1: Translation of the coordinate system.

Global	Siemens	MCL
Longitudinal	x	-3
Lateral	y	-1
Normal	z	-2

4.4 Boundary conditions and coordinate system definitions

Since the calculations are done parallel at STS and at MCL and the results are compared, it is important to translate the coordinate system used by the two set of calculations. **Table. 4.1** represents the translation of the two coordinate systems with respect to the global coordinate system. **Fig. 3.7** represents the coordinate system for the finite element calculations.

4.5 Simulation steps

The FE calculations are carried out for several cases of wheel loading. Each simulation is a set of the following four calculation steps.

- The wheel and the rail are positioned according to the inputs of the dynamical multi-body system SIMPACK.
- The wheel and the rail are brought in mutual contact by a displacement boundary condition. The wheel is moved downwards (-2 direction) so far as to produce a contact pressure on the rail.This step produces a static stamping of the wheel onto the rail.
- After a contact between the wheel and the rail is established, the wheel is loaded with a moment Tx acting at the middle point of the axle producing a force in 2 direction at the contact between the wheel and the rail (see **Fig. 3.2**). The middle point of the axle is chosen since it is also the symmetry point of the wheel set and a standard point for outputs of the simulation program SIMPACK.
- The velocity boundary conditions are applied now: The rolling of the wheel and the translational movement of the rail is produced using kinematical boundary conditions acting at the wheel axle and the rigid part of the rail. These boundary

conditions can simulate the rigid slip between wheel and rail due to acceleration, braking or sliding in transversal direction in a curve.

4.6 Results

The results for the case of a wheel running on a straight track and that for the inner and outer wheel in a curved track are presented at the position where the wheel and rail are loaded using the maximum moment and after movement of the contact patch along the rail of about 20mm. The wheel and the rail are meshed in a fine way. The element size is 1mm, in the region where the results are obtained.

The numerical values are recorded after a movement of a distance larger than the length of the contact patch where it can be assumed that a quasi-static state is reached.

The contact patch is an ellipse with major and minor axes of length 2a and 2b, respectively. A normal reaction force N acts at the wheel-rail contact patch.

The results from FE simulation and MBS simulations are tabulated and compared (see **Table. 4.2 and 4.3**).

The following are the cases that have been analyzed.

- Wheel on a straight track
- Wheel on the inner track in a curve

4.6.1 Wheel in a straight track

Table 4.2: Comparing the results of the FE and MBS simulations. (Case of a straight track)

Wheel set	Units	Siemens	MCL
y_RS	mm	0.15	0.15
z_Rs	mm	-424.85	-424.85
Yaw angle	rad	.00001	.00001
Roll angle	rad	-0.00001	0.00001
Wheel angular velocity	rad/sec	-52.232	-52.232
Reaction forces and moments at the bearings			
Fx	N	13474.8	14385.7
Fy	N	-657	-471.852
Fz	N	76987.4	80670
Tz	Nm	10124.5	10791.6
Driving moment	Nm	-5726.2	-6115.09
Values recorded at contact surface			
Tx	N	-13474.8	-14392.1
Ty	N	-2006.7	-2295.59
N	N	81163.9	80568.4
a	mm	5.65	5.8
b	mm	8.02394	10
yw	mm	-1.4	-1
yr	mm	01.8	-0.7

4.6.2 Wheel on the inner rail in a curve

Table 4.3: Comparing the results of the FE and MBS simulations. (Case of the inner wheel in a curve)

Wheel set	Units	Siemens	MCL
y_RS	mm	5.61	5.61
z_Rs	mm	-425.13	-425.13
Yaw angle	rad	.00128	.00128
Roll angle	rad	-0.00049	-0.00049
Wheel angular velocity	rad/sec	-64.866	-64.866
Reaction forces and moments at the bearings			
Fx	N	20940.8	22128.7
Fy	N	-7797.2	-7091.3
Fz	N	61577.2	66240.9
Tz	Nm	15990	16748.3
Driving moment	Nm	-8895.3	-9355.4
Values recorded at contact surface			
Tx	N	-20950.8	-22152.2
Ty	N	6860.8	4968.67
N	N	65851.6	66411.7
a	mm	6.08384	9.5
b	mm	4.87334	4.25
yw	mm	-13.57	-8
yr	mm	-4.69	0.6

This model is able to describe the material response near the wheel surface due to rolling contact and is an important enhancement in comparison to purely static models, where only the stamping of a wheel onto a rail is described or models where the normal and tangential forces (stresses) simulating a contact patch are moved along the wheel surface. Such contact pressures are obtained by finite element stamping models or some Kalker software using a purely elastic material response e.g. CONTACT .

By reducing the bulk volume of the model and hence the number of elements, we have succeeded in greatly controlling the calculation time. This has allowed us to make more calculations in a shorter period of time and using normal PCs.

The model is able to describe isotropic, kinematic and mixed cyclic hardening of the elastic-plastic material. A damage indicator can be implemented to describe the danger of material failure.

This finite element model builds the basis to implement further micromechanical and metal-physical models to describe the rolling contact fatigue and the development of wear. In combination with the loads and kinematics obtained from dynamic multi-body programs or dynamic finite element programs we have now a powerful instrument for the analysis of stress and strains due to a big variety of loading conditions. This is a prerequisite for the evolution of rolling contact fatigue in wheels.

CHAPTER 5

Examination of the plastification of the wheel

With this chapter we enter into the scenario of elastic-plastic material definitions. The quasi-static model described in the previous two chapters is refined and adopted to describe the elastic-plastic deformation of the material near the surface for several interesting load cases. A FORTRAN code has also been integrated with the finite element model to record the development of damage in the wheel.

The model at hand is advanced in relation to models found in the literature [46],[47],[48]. This model, equipped with plastic material definitions, damage indicator and capable of simulating a wide variety of loading conditions describes in an accurate way the development of stresses, strains and indicates a damage development during the wheel-rail rolling process. The results show that conventional methods used for the design process must be questioned.

5.1 Finite element model

The wheel is modeled using only a part from the full wheel (see **Fig. 5.1**). This part is generated by rotating the original section outlines of the wheel through an angle of 8 degrees. Although a very reduced size of the wheel part is taken, the computing time for the elastic-plastic simulation of this complex rolling contact process takes approximately twenty-four hours.

The length of the rail is chosen with 70 mm, **Fig. 5.2** . The friction coefficient between the wheel and the rail is set at $\mu_f = 0.4$ (It is to be noted that in the previous calculations μ_f was taken to be 0.3. It is found that $\mu_f = 0.4$ is a more realistic value) . For defining loading conditions for the inner and outer wheel in a curved track and a wheel in a straight track the yaw and roll angles are applied to the wheel and the inclination of the rail is taken into account, see **Tab. 5.1**.

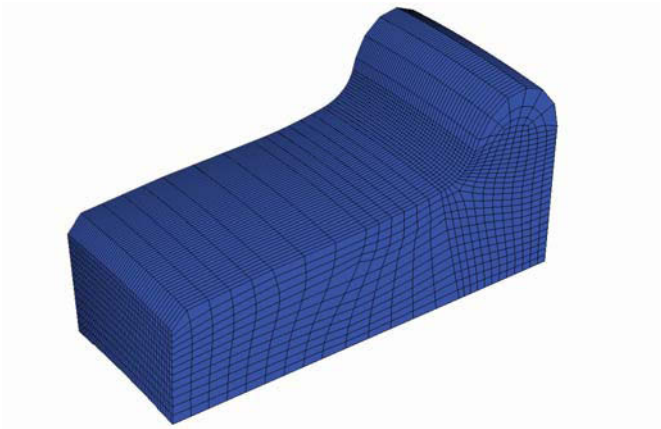

Figure 5.1: Part of the wheel modeled as deformable

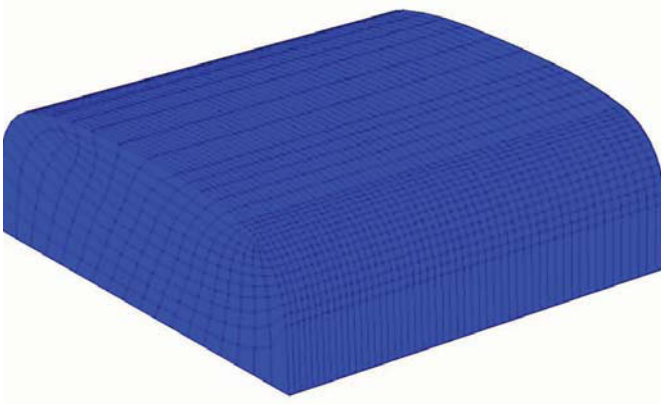

Figure 5.2: Part of the rail modeled as deformable

Table 5.1: Angles defining the relative position of wheel and the rail for various scenarios.

	Straight rail	Inner rail in a curve	Outer rail in a curve
Yaw angle °	0.00001	-0.00125	0.00128
Roll angle °	-0.00001	0.00048	-0.00049
Rail inclination °	0.02499	0.02499	0.02499
Curve radius m	Straight line	900	-900
Speed ms^{-1}	22.22222	27.59718	27.59723

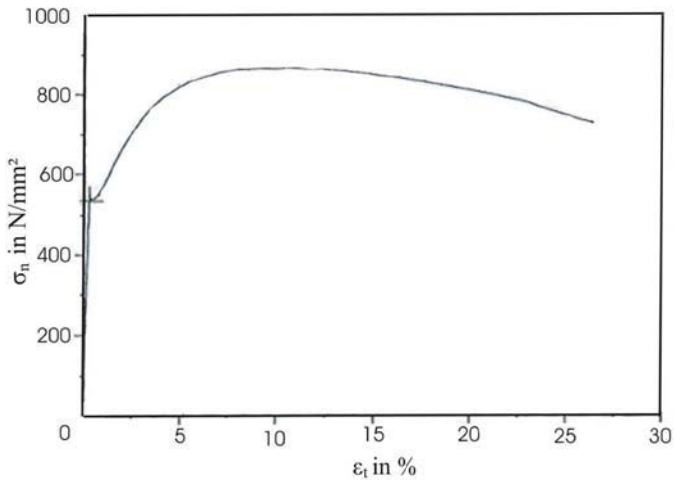

Figure 5.3: Engineering stress engineering strain curve for wheel material

An elastic plastic behavior is assigned to the wheel material and an elastic behavior to the rail material. The engineering stress vs. engineering strain curve shown in **Fig. 5.3** represents the behavior of the wheel material under axial loading. The true stress and true strain values are required as an input for ABAQUS calculations. However, for low values of strains engineering stress and engineering strains can also be used. The properties of the wheel and the rail are tabulated in **Tab. 5.1**.

The regions of the rail and the wheel, which are at such distances from the contact patch that their influence on the analysis and the final results can be neglected, are defined as rigid. This simplifies the model and drastically saves calculation time.

A spring has to be applied to the rail in lateral direction with the same spring constant as used in the SIMPACK calculations performed at the STS to obtain the same results of reaction and other contact forces and variables.

The car load is simulated by applying a moment T_x(**Fig. 3.2**) at the center of the wheel axis so as to produce a stamping of the wheel on the rail.

Other boundary conditions and forces are applied at the rail base and the mid point of the wheel axle to take care of the kinematics of the system. Rest of the details of the model are included in **Chapter 4**.

Elastic behavior(Wheel and the rail)	
Property	Value
Density [Kgm^{-3}]	7800
Young modulus [$10^{11}Nm^{-2}$]	2.1
Poison's ratio	0.3
Plastic behavior (Wheel)	
Stress [10^6Nm^{-2}]	Plastic strain [%]
540	0.00000
570	0.00625
620	0.01250
660	0.01875
710	0.02500
750	0.03125
790	0.03750
810	0.04375
830	0.05000

Table 5.2: Wheel and rail material properties

Table 5.3: Variables describing kinetics and dynamics of the system.

Symbol	Description
V_{w1}, V_{w2}, V_{w3}	Velocities of the wheel in respective directions
W_{w1}, W_{w2}, W_{w3}	Angular velocities of wheel in respective directions
V_{r1}, V_{r2}, V_{r3}	Velocities of rail in respective directions
T_{drive}	Driving moment acting on the wheel
T_3	Moment defining the car load

Tab. 3.1.5 shows a correlation of the local coordinate system to the global coordinate system.

The variables governing the kinetics and the dynamics of the system are tabulated in **Tab. 5.3**. The rail velocity, V_{r1}, is constrained by the lateral spring attached to the rail. The velocity V_{r2} is set to zero. The velocity component V_{r3} simulates the wheel velocity in running direction and the rail moves in negative 3 direction. That means the rail is moved in 3 direction and the wheel remains in its place.

The wheel is fixed in space; hence the three components V_{w1}, V_{w2} and V_{w3} are zero. W_{w1} is the rotational velocity depending on the moment T_{drive}. The rotational velocity W_{w2} is set to zero and W_{w3} is unconstrained.

5.2 Damage indicator

From the available approaches to recording the damage in engineering materials [49],[50], the one which fits best to the case of wheel-rail contact is chosen. An external FORTRAN code implements the damage indicator variable. This code interacts with ABAQUS/STANDARD and stores the development of damage in the external variable UVAR(1).

This code is based on the work by Fischer et al. [51]. It is the implementation of the damage indicator developed by Hancock and Mackenzie [52] which is based on the work of Rice and Tracy [53]. It is defined as

$$D_1 = \frac{1}{1.6\epsilon_0} \int_0^{\epsilon_0} exp(R\frac{\sigma_H}{\sigma_{eq}}) d\epsilon_{eq}$$

where D_1 is the damage indicator variable. σ_H is the hydrostatic stress and σ_{eq} is the equivalent stress; ϵ_0 is a calibration parameter. The value of the constants R and ϵ_0 are taken to be 1.5 and 0.2, respectively.

It is assumed that the value of D_1 reaches 1.0 at the time when failure starts. Some interesting damage models for a ductile matrix have been discussed also by Drabek and Böhm in [54].

The concept of damage indicators is based on the growth of a void in an elastic-plastic solid subjected to a hydrostatic tension and a certain deviator. The case of wheel-rail contact lies in the compressive regime. However Gänser et al. [50] have shown that the concept of damage indicator is also applicable in all the scenarios where at least one component of the principal stresses is tensile. The cases where dominant shear exists satisfy the above minimum requirement. Hence the application of the damage indicator variable in a wheel-rail scenario is admissible.

The microvoids present in the microstructure may grow in a preferable direction due to shearing. This leads to the flattening of the voids in the orthogonal direction. The damage indicator can be considered to give a picture on the local material damage behavior.

5.3 Initial calculations and the results

Before going into detailed and cyclic calculations involving large number of cycles, some calculations are performed with only a small number of load cycles. These calculations help us identify the load scenarios that need to be analyzed for large number of load cycles. The following set of preliminary calculations are made.

- A wheel running on the inner track in a curve.
- A wheel running on the outer track in a curve.
- A wheel rolling on a straight track.
- A wheel accelerating on a straight track.
- A wheel braking on a straight track.

With reference to the shakedown map, an analysis is performed to identify the location of different loading scenarios on a standard shakedown map for a point contact. See **Fig.5.4**. Equivalent accumulated plastic strains PEEQ and the corresponding accumulation of damage D are plotted for different loading scenarios. **Fig. 5.6, 5.7 and 5.8** show the accumulated equivalent plastic strain PEEQ and the damage parameter D at the element where the maximum plastification is recorded for various loading scenarios. To simulate the different scenarios of mixed loading,different values of the driving moment have been applied.**Fig. 5.5** shows the traction moment applied to the wheel axle for one such selected case.

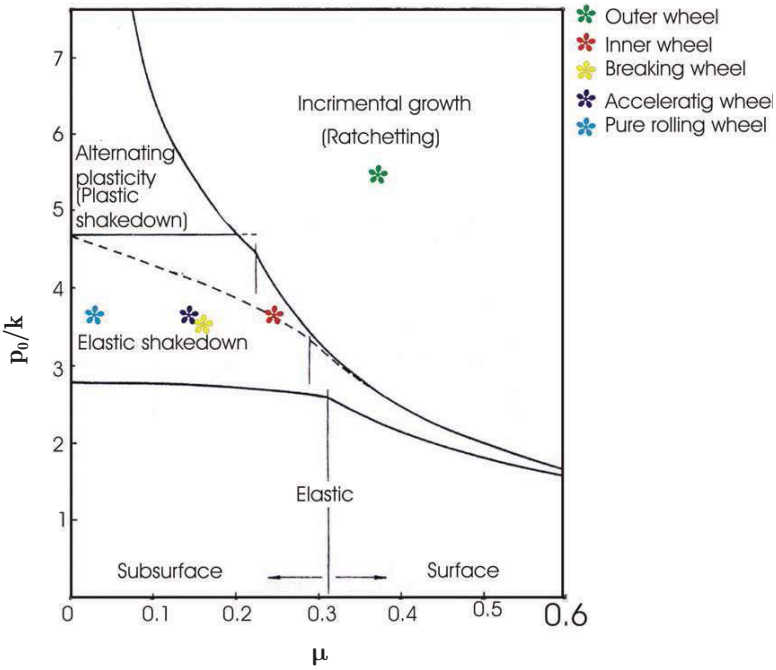

Figure 5.4: Location of various load scenarios on shakedown map [55]

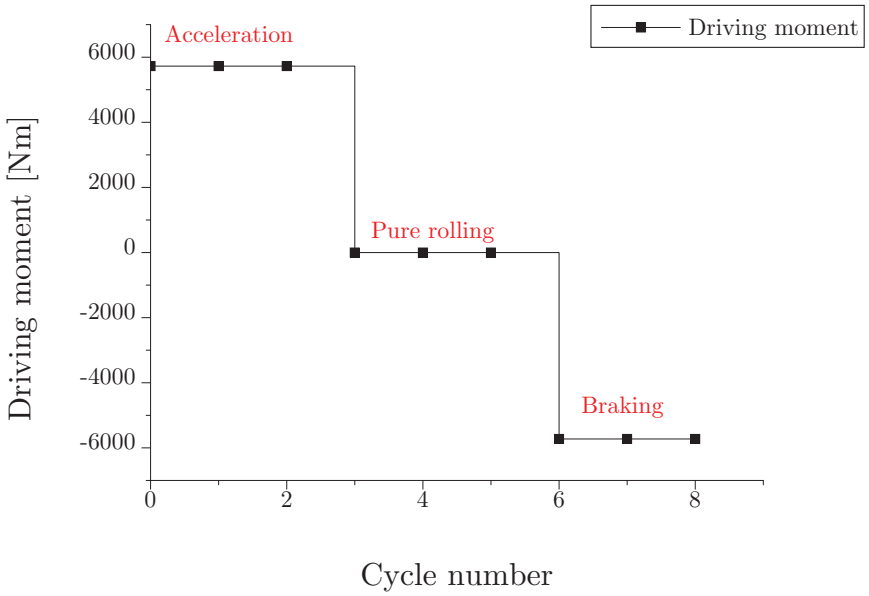

Figure 5.5: Driving moment applied on the axle of the wheel for modeling a wheel running on a straight track - 3 cycles of acceleration, 3 cycles of pure rolling and 2 cycles of braking

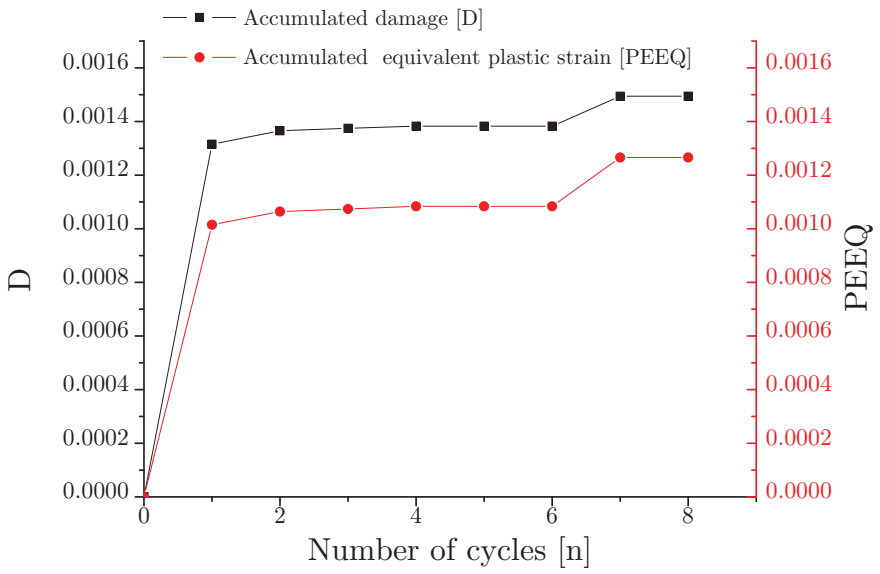

Figure 5.6: Wheel running on a straight track - 3 cycles of acceleration, 3 cycles of pure rolling and 2 cycles of braking

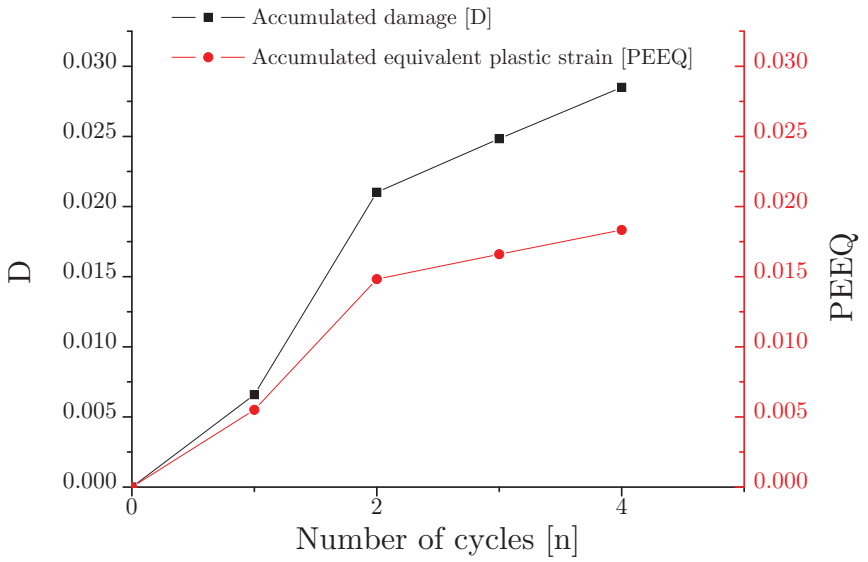

Figure 5.7: Wheel running on the outer rail in a curved track

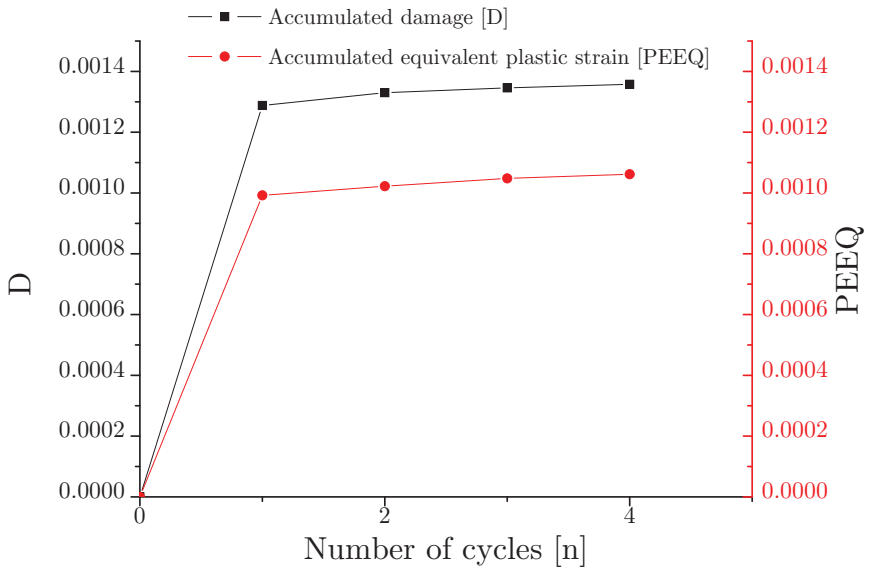

Figure 5.8: Wheel running on a straight track

An analysis of the stresses in the contact patch has been performed. This analysis is inspired by the work done by Johnson [35].

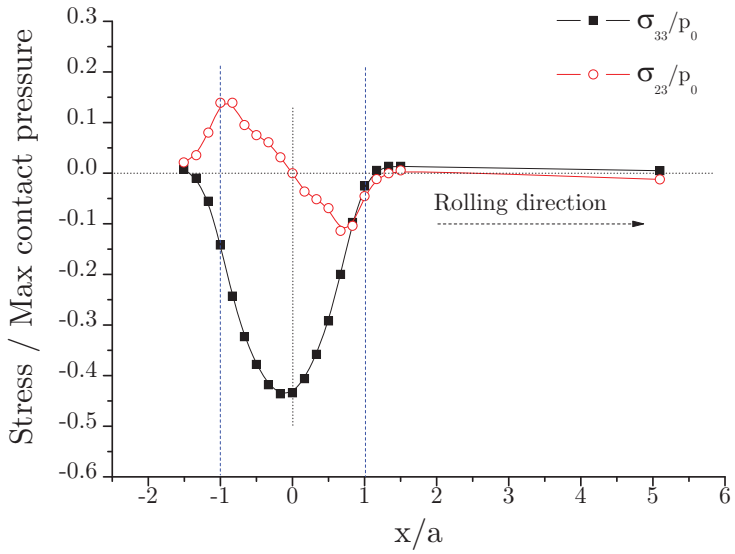

Figure 5.9: Relative longitudinal and shear stress distribution on a line in rolling direction through the center of a contact patch in the case of pure rolling during the third cycle(a=semiaxis, in the rolling direction, of the contact ellipse)

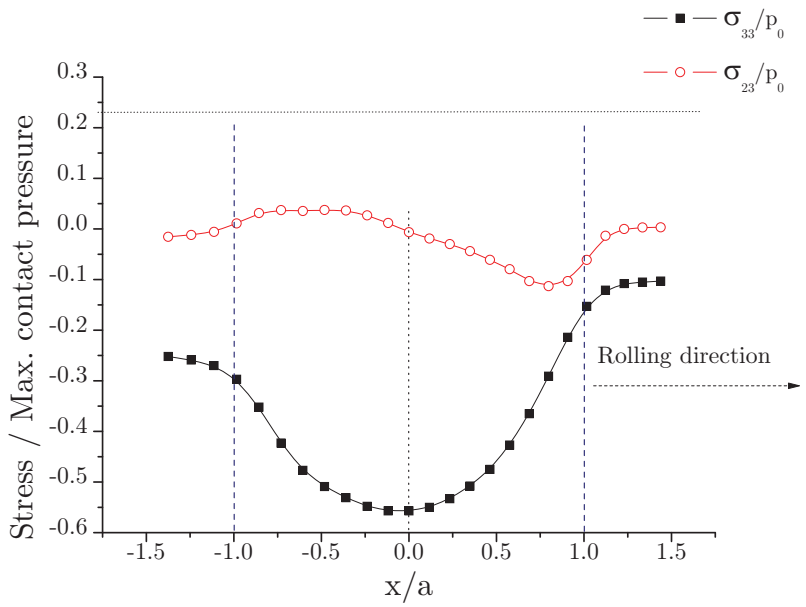

Figure 5.10: Relative longitudinal and shear stress distribution on a line in rolling direction through the center of a contact patch in the case of an outer wheel in a curve during the third cycle(a=semiaxis, in the rolling direction, of the contact ellipse)

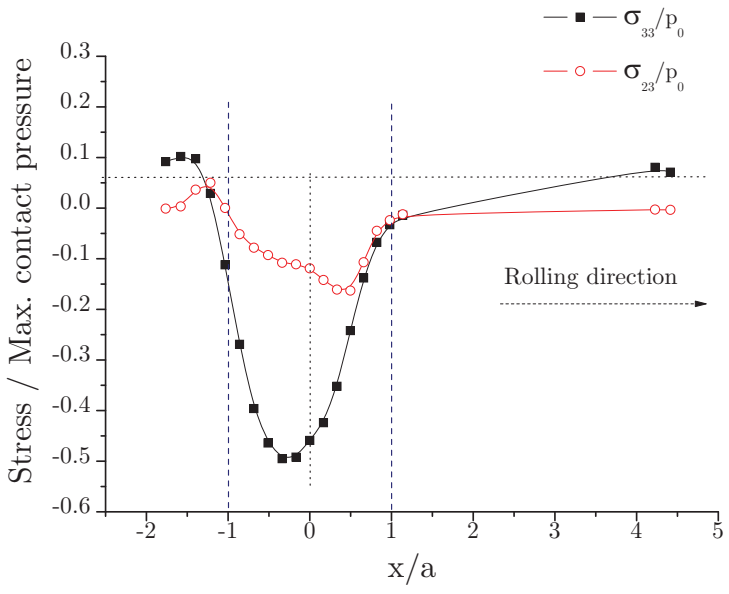

Figure 5.11: Relative longitudinal and shear stress distribution on a line in rolling direction through the center of a contact patch in the case of an inner wheel in a curve during the first cycle(a=semiaxis, in the rolling direction, of the contact ellipse)

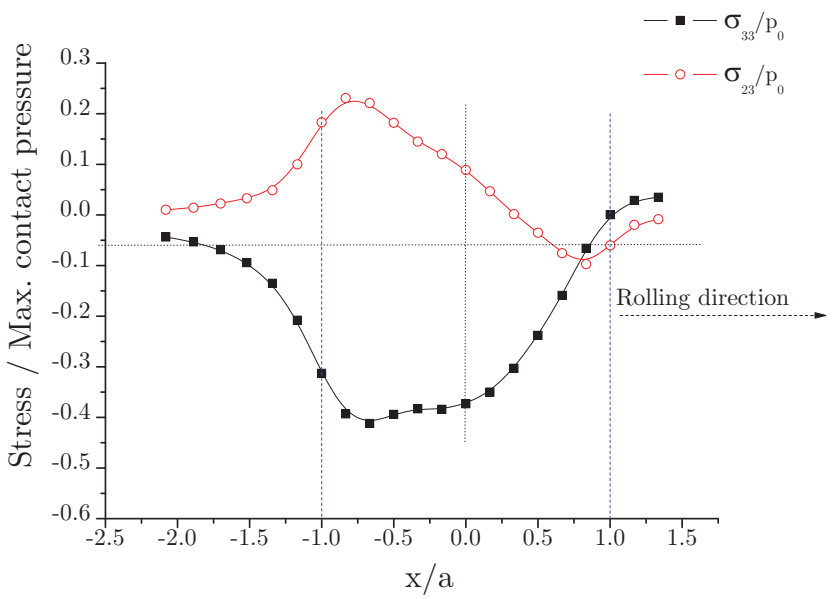

Figure 5.12: Relative longitudinal and shear stress distribution on a line in rolling direction through the center of a contact patch in the case of a braking wheel during the third cycle(a=semiaxis, in the rolling direction, of the contact ellipse)

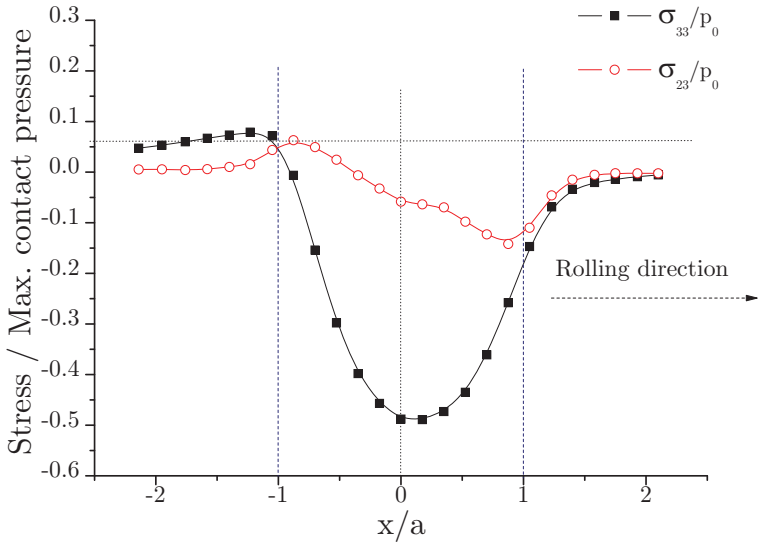

Figure 5.13: Relative longitudinal and shear stress distribution on a line in rolling direction through the center of a contact patch in the case of an accelerating wheel during the third cycle(a=semiaxis, in the rolling direction, of the contact ellipse)

This analysis, for the various cases of loading, leads to some interesting results. **Fig. 5.9** represents the values of σ_{33} and σ_{23}, during the third cycle of rolling, for the contact patch in the case of a wheel rolling with a constant velocity on a straight rail. In this plot the transition in the shear stress from positive to negative can be seen. The transition point lies at the center of the contact patch. The normal longitudinal stress is distributed quite symmetrically along the length of the contact patch.

The results for the outer and the inner wheel are plotted in figures **Fig. 5.10 and 5.11** , respectively. In the case of an outer wheel in a curve, see **Fig. 5.10**, the distribution of the stresses is no longer symmetrical (The leading edge is at the point on the wheel where the wheel makes the first contact with the rail: x/a = -1.0), almost no shear stress will appear in this region. The normal longitudinal stress distribution is similar to a braked wheel superposed by a residual longitudinal pressure stress produced by previous cycles.

In the cases of a braking and an accelerating wheel, **Fig. 5.12 and 5.13** , an asymmetric distribution of both the stresses is observed. The normal stress is higher near the trailing edge for a braking wheel. In the case of an accelerating wheel the normal stress is positive near the leading edge. It can be seen that in the case of acceleration there is higher compressive stress near the trailing edge compared to that near the trailing edge for a braking wheel.

5.4 Conclusions

Some important conclusions are drawn which are the basis for planning the cyclic loading analysis on the railway wheel in the next phase of the project. The following points illustrate the conclusions drawn from these preliminary calculations.

- In the cases of a wheel moving in a curve, the outer wheel shows a much higher tendency towards accumulating plastic strain and the development of damage in comparison to the inner wheel.
- A wheel running on the outer track produces the largest amount of plastic work and the largest value of damage. The maximum plastic deformation and damage accumulation are calculated at the surface of the wheel where, as known, surface cracks are produced during operation. To which extent the number of cycles decreases the plastic strain increment for this loading case has to be investigated in the next phase of this project.
- For an accelerated or braked wheel running on a straight track the plastification during the first run is seven times less than for the case of an outer wheel and is

decreasing with each cycle. A change in the rolling direction or from acceleration to braking can start a new accumulation of plastic deformation again. If the plastification is not stopped after some thousand cycles or even increased in each change from braking to acceleration, a crack can possibly be generated below the surface near or in the zone of maximum deformation and produce spalling or flaking from surface parts of the wheel. To which extent the change in the direction of the shear loading will influence the accumulation of the plastic deformation shall also be investigated in the next phase of this project.

- During pure rolling the plastification and development of damage can be neglected, but a small amount of plastic deformation is produced which does not correspond to shakedown maps from which a pure elastic behavior of the wheel material for the calculated load case is predicted. This difference will be investigated.

- The damage is predominantly accumulating in regions with the highest amount of plastic deformation, but also in regions near the contact patch where tensile stresses are present during the plastic deformation.

- The results of the investigations show quantitatively the differences between the loading conditions. It can be used for investigations with different sets of forces and geometries.

- The model allows for cyclic investigations with the use of a sophisticated description of the cyclic plastic behavior of the material.

- In the case of acceleration, the compressive stresses are much higher in comparison to those in the case of braking

CHAPTER 6

Cyclic Calculations

A quasi-static wheel-rail model is developed which is capable of performing an analysis for the cyclic loading of a wheel-rail system.

The model is optimized in terms of calculation time so it can be practically used for calculating a reasonably big number of load cycles. Calculations up to 50 cycles are performed in this work. With further optimizations some hundred cycles can be performed using the same model.

Calculations are done to study the accumulation of plastic equivalent strain and the subsequent development of damage in a railway wheel during its service life. The work is divided into two sections. The first section deals with cyclic loading without changing the direction of loading. In the second section, the first six cycles have the load applied in one direction, and further cycles consist of alternate forward and backward loading.

Various scenarios, defined by varied normal load P and traction coefficient μ, are calculated in both the sections. These scenarios cover almost the whole range of loading conditions encountered by a wheel in its normal service life.

Since all the calculated scenarios can be evaluated by shakedown maps, the results from these calculations are compared and mapped on the shakedown map.

In a real life scenario the wheel undergoes loading with changing direction; hence the set of calculations involving changing load directions is performed. The results from the two

sets of calculations are compared to get a quantitative outlook into the effect of changing directions (in general terms, braking, reversing and moving over a curve).

A qualitative analysis is made on the development of roughness on the wheel surface with increasing number of load cycles. These calculated developments in the wheel surface account for some of the discrepancies encountered in the results.

Based on the trends in damage rate for all the analyzed load cases, an attempt is made to quantify the relative service life of a wheel under different conditions of loading.

6.1 The model

The quasi-static model used for performing cyclic load analysis consists of a small fraction of the wheel and a rail of appropriate length. An eight degree sector of the wheel satisfies the need of achieving the steady state values of the interesting physical quantities. A corresponding value of the rail length is taken.

The wheel is assigned elastic-plastic material properties, and the rail is assumed to exhibit elastic material properties. The element size in and near the contact region is 1mm by 1mm. A smaller element size would have been helpful in a better understanding of the development of surface roughness and would have lowered the discrepancies in the results. However such relatively big element size is chosen to optimize the calculation time.

The friction coefficient, μ_f, between the wheel and the rail is taken to be 0.3. A lateral spring connected to the rail facilitates the damping out of any possible oscillations arising in the system. All the degrees of freedom, except longitudinal and lateral displacements, for the rail are "frozen". The degrees of freedom of the wheel are assigned to allow the wheel producing a stamping action against the rail and enabling to rotate about the wheel set axis. **Fig.3.7** illustrates the model and the co-ordinate system.

6.2 Unidirectional loading

Calculations are made by loading the wheel repeatedly up to 30 times in the same direction. **Tab. 6.1** lists the damage indicator D and its rate in this set of calculations. The following terms have been used in **Tab. 6.1**:

Identity	Identification code of the calculation.
P	Normal Load in percent of the standard normal load.
μ_f	Traction coefficient.
Damage Depth	Depth in the wheel where the maximum damage was observed.
D	Accumulated damage at the end of calculation.
$\overline{dD}$	Weighted damage rate.

Calculations are performed with various combinations of normal load P in percent(The standard normal load represents 100 percent load which amounts to a static load of 80568.4 N on a wheel) and a given traction coefficient μ. The first column in the table represents the identification of each calculation by a set of two numbers separated by a dash symbol. The first number represents the normal load as a percent of the standard normal load and the second number represents the traction coefficient μ multiplied by one hundred. Column n represents the number of cycles the wheel-rail system was loaded. The column labeled damage depth represents the approximate depth beneath the wheel surface where the maximum damage is recorded. D is the total accumulated damage. The last column lists the weighted damage rate $\overline{dD}$ calculated by neglecting the first ten load cycles of the total n cycles performed in the calculation. The following formula describes the mathematical procedure to obtain the $\overline{dD}$ as

$$\overline{dD} = \frac{\sum_{k=11}^{n} (k-10) * dD_k}{\sum_{k=11}^{n} (k-10)}$$

The details from the above set of calculations have been plotted in **Fig.6.1** to **Fig.6.24** .

The accumulated equivalent plastic strain PEEQ and the accumulated damage D have been plotted against the traction coefficient μ for various normal loads in **Fig.6.1** and **Fig.6.2**. All the values are recorded at the end of thirty cycles. Some of the cases could not be calculated up to thirty cycles. For such cases, the results are linearly extrapolated to thirty cycles.

Six cases corresponding to different normal loads are considered. It is observed that the accumulated damage D and the accumulated equivalent plastic strain PEEQ have a trend to increase with an increase in the traction coefficient μ. This increase in the accumulated equivalent plastic strain PEEQ is not so severe in the case of low normal loads. In the case of high normal loads the plot takes an exponentially increasing trend. Another important implication that is drawn from these two figures is the similar behavior in the trend of

increase and decrease of accumulated damage D and the accumulated equivalent plastic strain PEEQ.

Table 6.1: Unidirectional loading cases analyzed.

Identity	P%	μ	n	Damage Depth	D	$\overline{dD}(10^{-5})$
050-35	50	0.35	30	$<$ 2 mm.	0.0121709	1.180
070-20	70	0.20	30	$<$ 2 mm.	0.0034116	3.426
070-30	70	0.30	30	Surface	0.0137135	1.226
070-35	70	0.35	30	Surface	0.0219291	5.309
090-17	90	0.17	30	$>$ 2 mm.	0.0064435	1.191
090-20	90	0.20	30	Surface	0.0068624	2.523
090-25	90	0.25	30	Surface	0.0144245	1.404
090-30	90	0.30	30	Surface	0.0295552	8.337
090-35	90	0.35	30	Surface	0.0431626	10.1008
100-17	100	0.17	29	$>$ 2 mm.	0.0081340	0.210
100-20	100	0.20	30	$>$ 2 mm.	0.0093771	1.696
100-25	100	0.25	29	$<$ 2 mm	0.0205601	2.231
100-30	100	0.30	28	Surface	0.0385214	6.740
100-35	100	0.35	28	Surface	0.0558343	6.898
110-17	110	0.17	27	$>$ 2 mm.	0.0101488	0.020
110-20	110	0.20	27	$>$ 2 mm.	0.0121055	1.880
110-25	110	0.25	26	Surface	0.0270473	16.000
110-30	110	0.30	26	Surface	0.0561982	16.612
110-35	110	0.35	26	Surface	0.0767703	20.898
120-10	120	0.10	25	$>$ 2 mm.	0.0110098	2.520
120-15	120	0.15	25	$>$ 2 mm.	0.0121709	1.180
120-17	120	0.17	25	$>$ 2 mm.	0.0122010	0.860
120-25	120	0.25	24	Surface	0.0356772	20.439
120-30	120	0.30	24	Surface	0.0162314	6.450
120-35	120	0.35	24	Surface	0.1059999	64.751
140-05	140	0.05	22	$>$ 2 mm.	0.0146634	1.010
140-13	140	0.13	22	$>$ 2 mm.	0.0167062	1.640
140-17	140	0.17	22	$>$ 2 mm.	0.0198242	0.650
140-20	140	0.20	21	$<$ 2 mm.	0.0269694	9.900
140-30	140	0.30	21	Surface	0.1018321	31.384
140-35	140	0.35	20	Surface	0.1658270	268.720

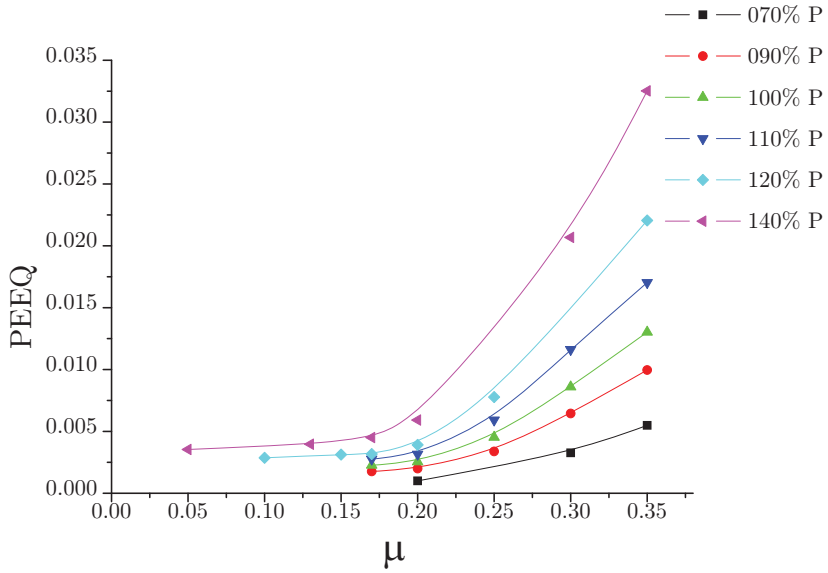

Figure 6.1: Dependence of accumulated equivalent plastic strain PEEQ on traction coefficient μ with parameter load P.

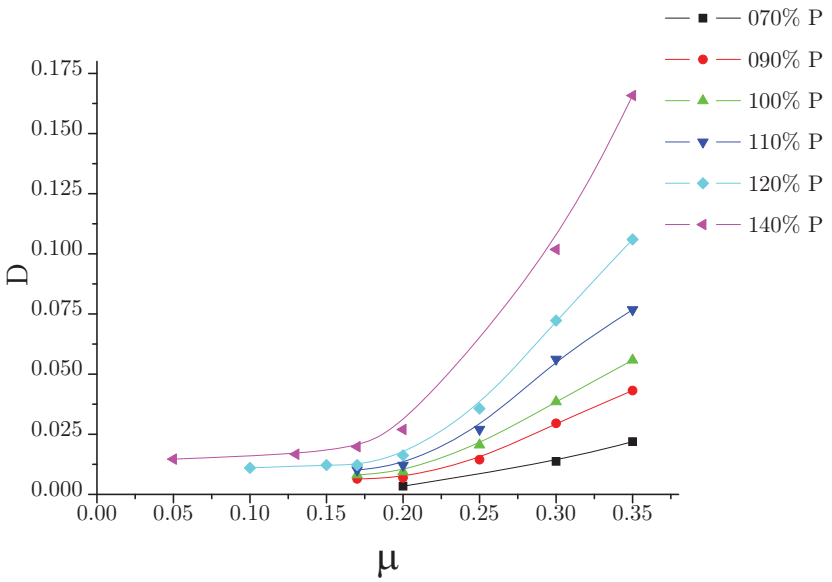

Figure 6.2: Dependence of accumulated damage D on traction coefficient μ with parameter load P.

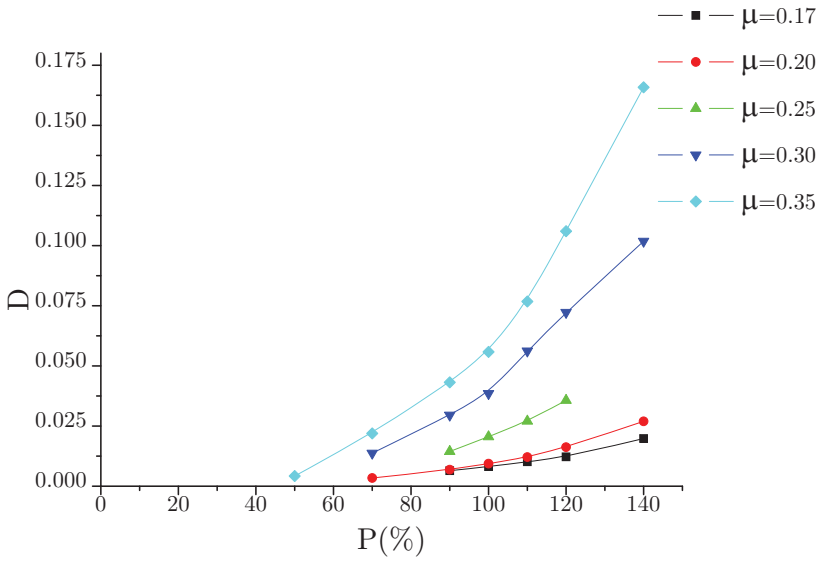

Figure 6.3: Dependence of accumulated damage D on normal load P with parameter traction coefficient μ.

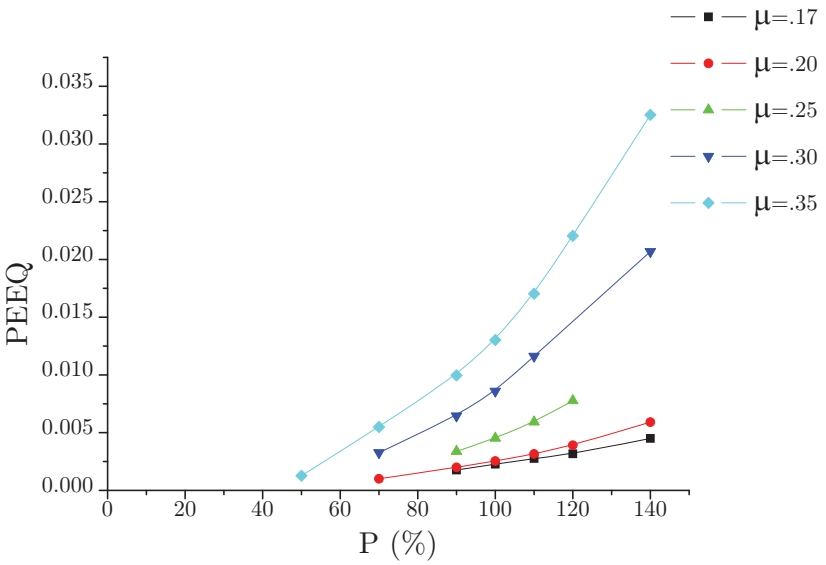

Figure 6.4: Dependence of accumulated equivalent plastic strain PEEQ on normal load P with parameter traction coefficient μ.

Fig.6.3 and **Fig.6.4** show the dependence of the accumulated damage D and accumulated equivalent plastic strain PEEQ, respectively, on the load P. Here again an analogous trend is observed in the behavior of D and PEEQ.

In **Fig.6.5** - **Fig.6.9** the accumulated equivalent plastic strain PEEQ is plotted against the number of cycles n for various normal loads. Similarly in **Fig.6.10** - **Fig.6.14** accumulated damage D for various normal loads are plotted against n. It is observed that both PEEQ and D have higher values for higher loads at any given value of traction coefficient μ.

The points plotted for the five analyzed cases with different traction coefficients μ show that both the accumulated equivalent plastic strain PEEQ and the resulting accumulated damage D increase with an increase in the normal load. The slope of the curve also increases for higher values of load. The observed dependence of PEEQ and D on P is not as strong as the dependence on μ. The quantities D and PEEQ show to have an exponential dependence on μ.

It is also observed that the maximum plastification and the resulting damage takes place in the first few cycles. In the later cycles either the rate of plastification is very low or zero depending on P and μ.

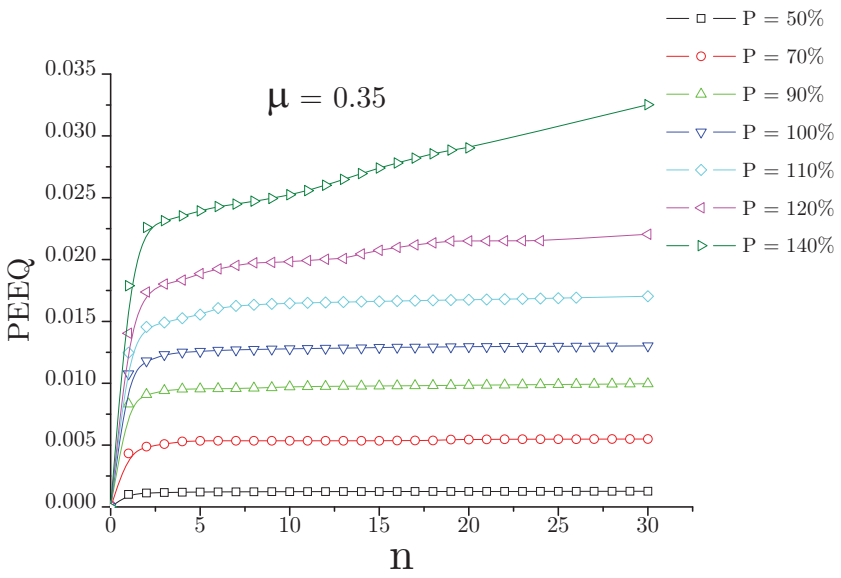

Figure 6.5: Development of accumulated equivalent plastic strain PEEQ for different loading P over number of cycles n at a constant $\mu = 0.35$.

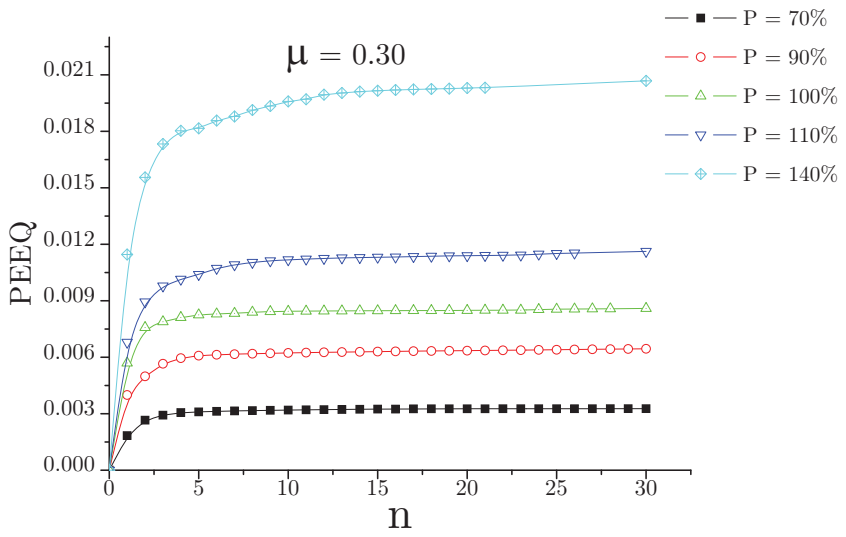

Figure 6.6: Development of accumulated equivalent plastic strain PEEQ for different loading P over number of cycles n at a constant $\mu = 0.30$.

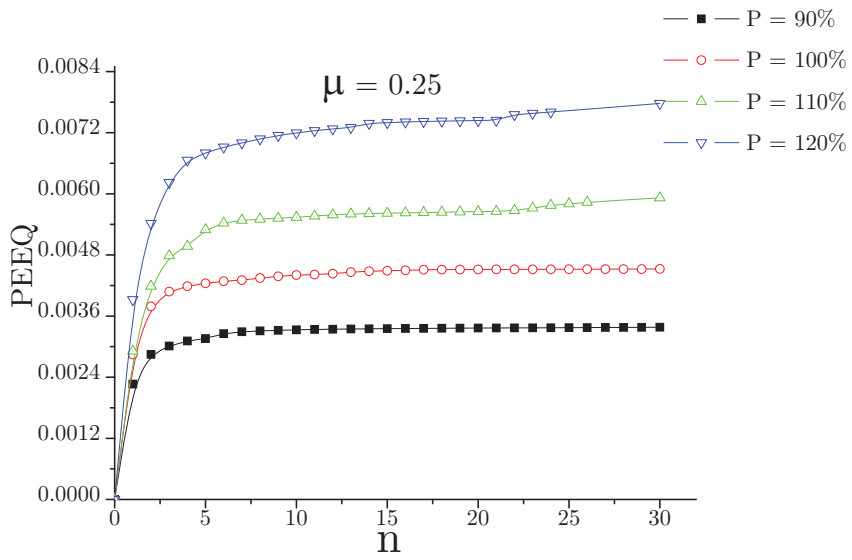

Figure 6.7: Development of accumulated equivalent plastic strain PEEQ for different loading P over number of cycles n at a constant $\mu = 0.25$.

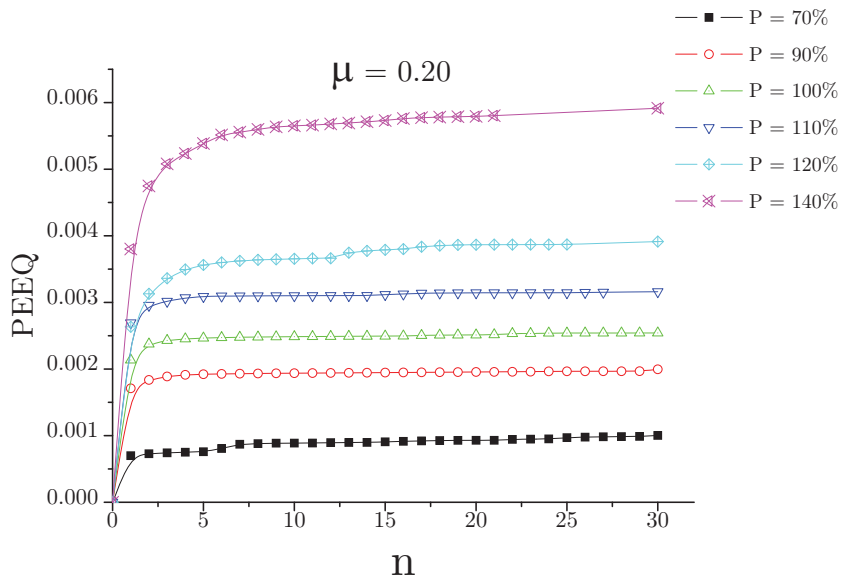

Figure 6.8: Development of accumulated equivalent plastic strain PEEQ for different loading P over number of cycles n at a constant $\mu = 0.20$.

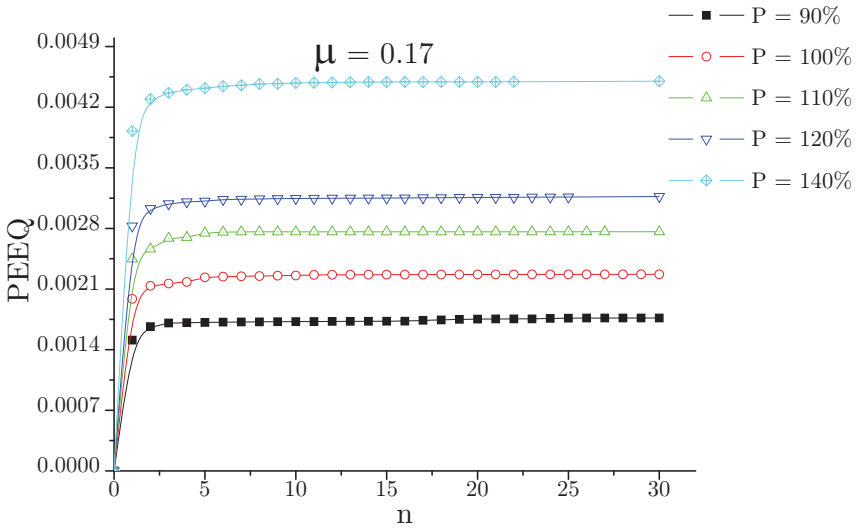

Figure 6.9: Development of damage D for different loading P over number of cycles n at a constant $\mu = 0.17$.

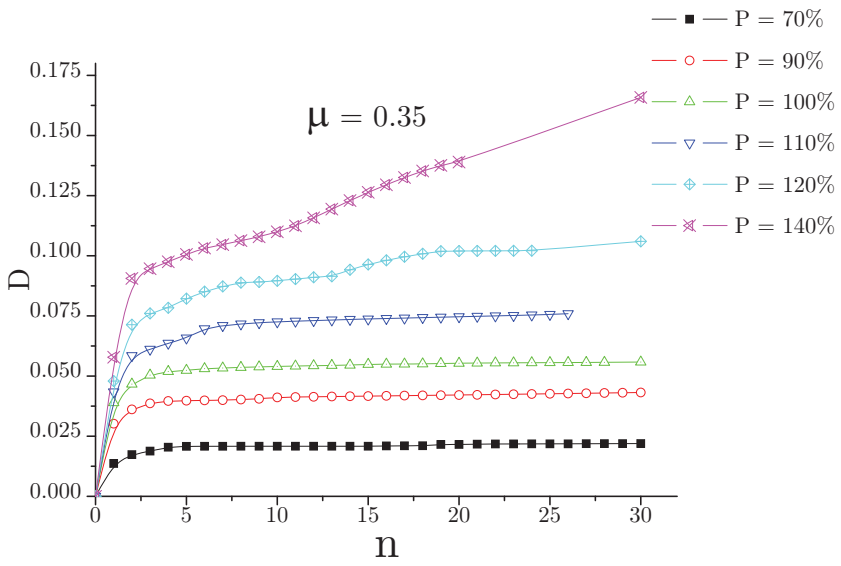

Figure 6.10: Development of damage D for different loading P over number of cycles n at a constant $\mu = 0.35$.

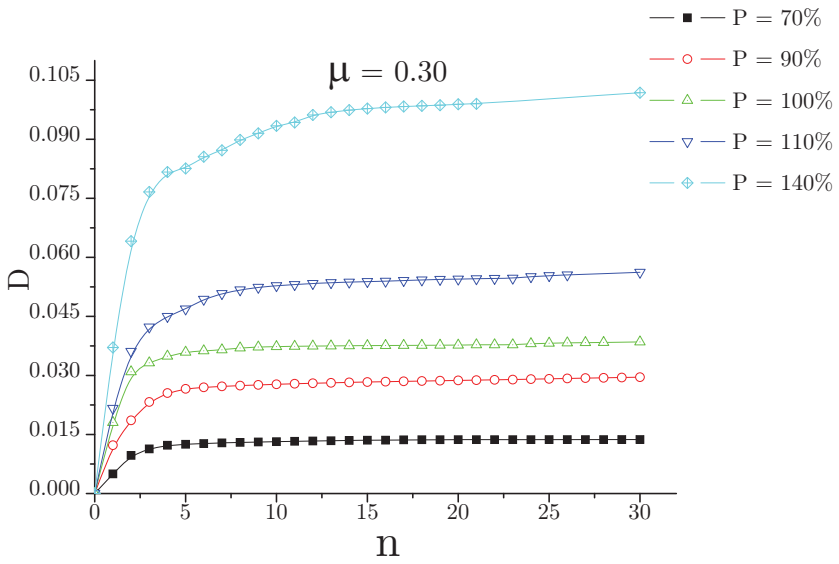

Figure 6.11: Development of damage D for different loading P over number of cycles n at a constant $\mu = 0.30$.

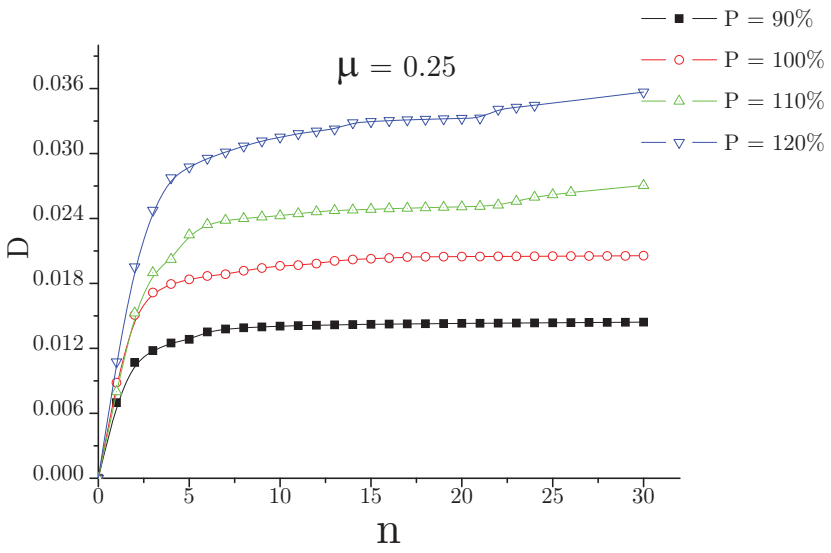

Figure 6.12: Development of damage D for different loading P over number of cycles n at a constant $\mu = 0.25$.

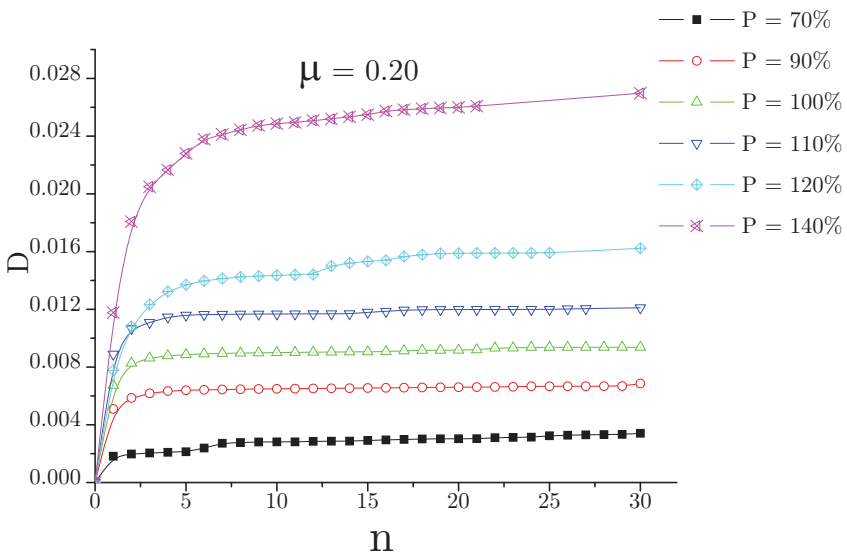

Figure 6.13: Development of damage D for different loading P over number of cycles n at a constant $\mu = 0.20$.

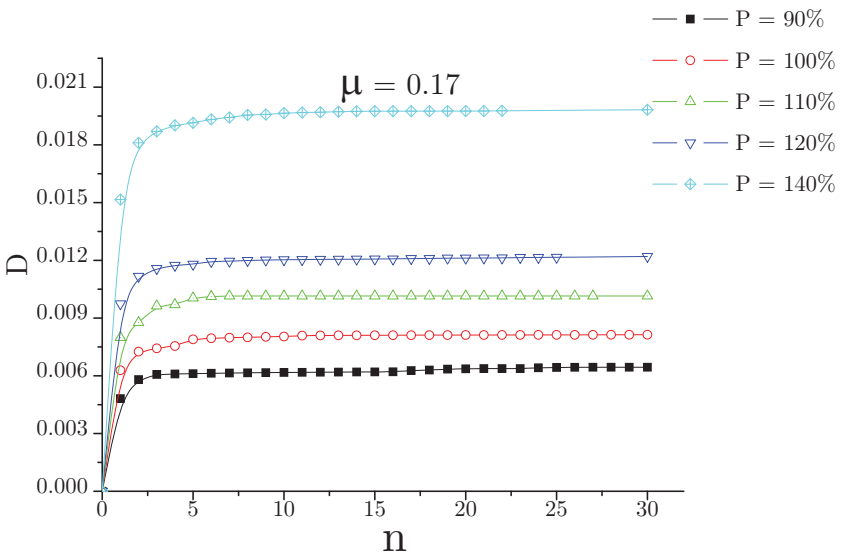

Figure 6.14: Development of damage D for different loading P over number of cycles n at a constant $\mu = 0.17$.

Accumulated equivalent plastic strain PEEQ and accumulated damage D are plotted in **Fig.6.15** - **Fig.6.19** and **Fig.6.20** - **Fig.6.24**. Each plot is generated by taking the values of PEEQ and D for a specific node in the wheel where the maximum plastification is observed. Both PEEQ and D show an increasing trend with increasing μ in all the cases. For values of μ lower than 0.17 the plot has a rather low slope but upon increasing the value of μ higher than 0.17, an exponentional increase in PEEQ and D is observed.

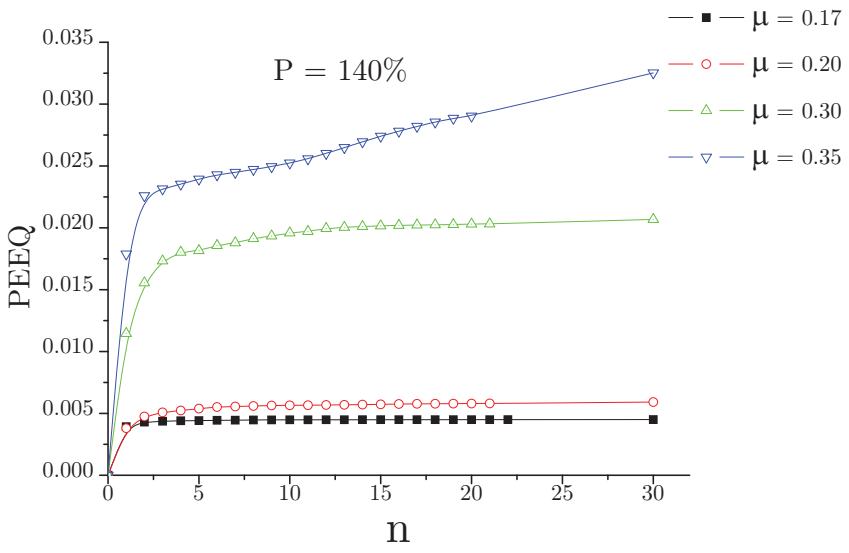

Figure 6.15: Development of accumulated equivalent plastic strain PEEQ over number of cycles for different traction coefficient μ at P = 140%.

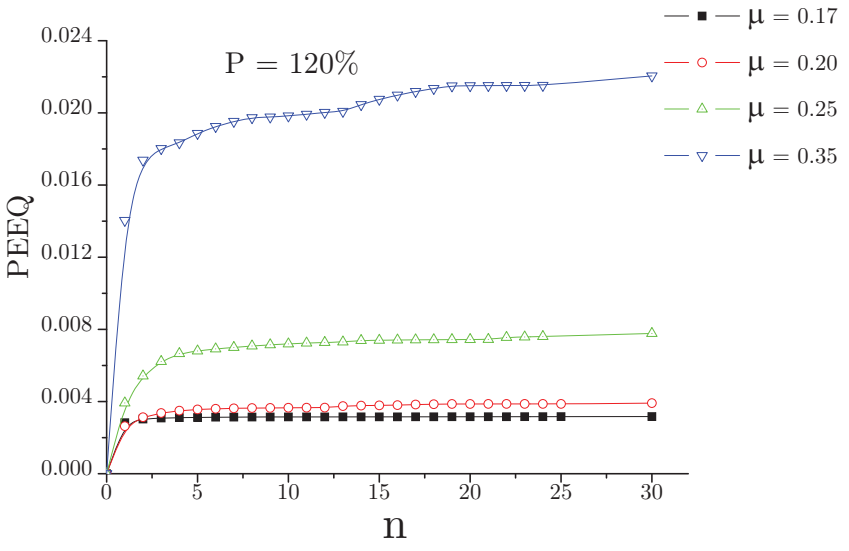

Figure 6.16: Development of accumulated equivalent plastic strain PEEQ over number of cycles for different traction coefficient μ at P = 120%.

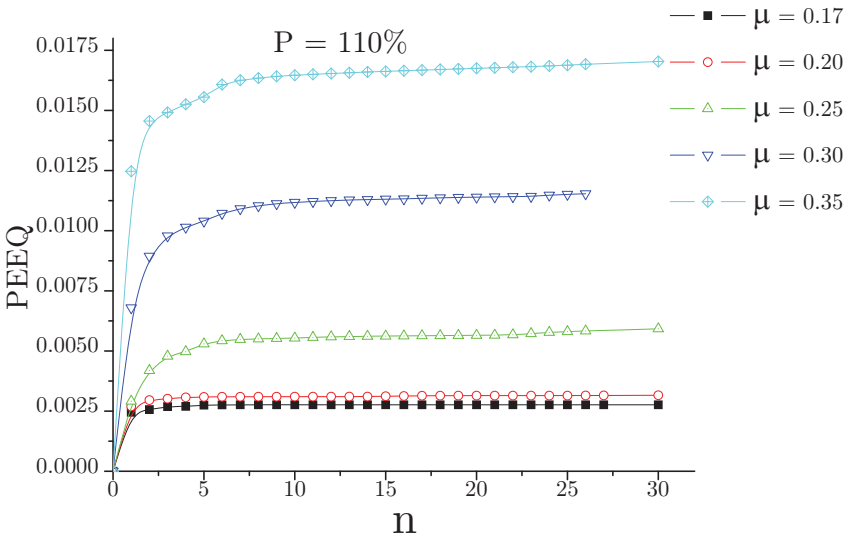

Figure 6.17: Development of accumulated equivalent plastic strain PEEQ over number of cycles for different traction coefficient μ at P = 110%.

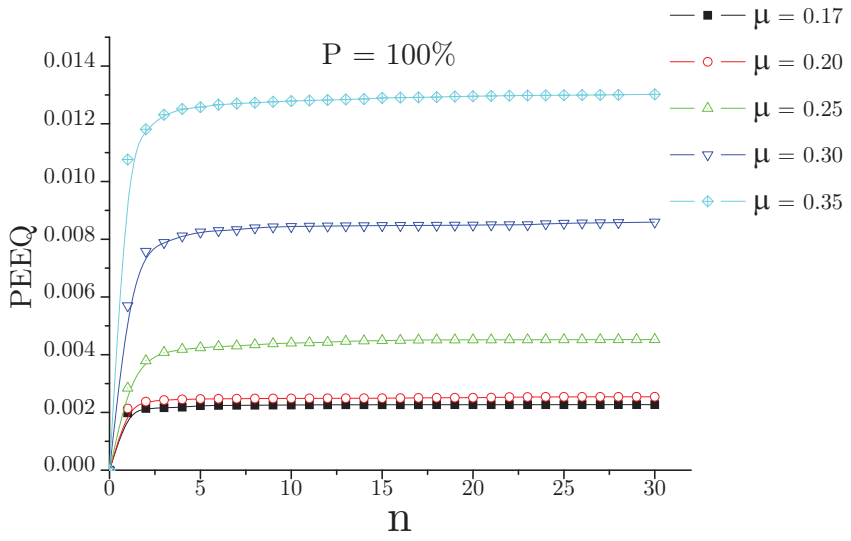

Figure 6.18: Development of accumulated equivalent plastic strain PEEQ over number of cycles for different traction coefficient μ at P = 100%.

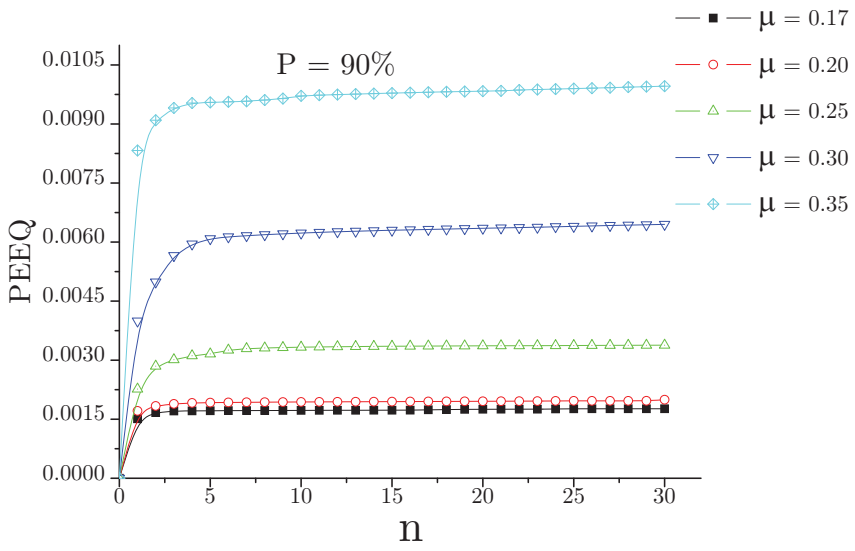

Figure 6.19: Development of accumulated equivalent plastic strain PEEQ over number of cycles for different traction coefficient μ at P = 90%.

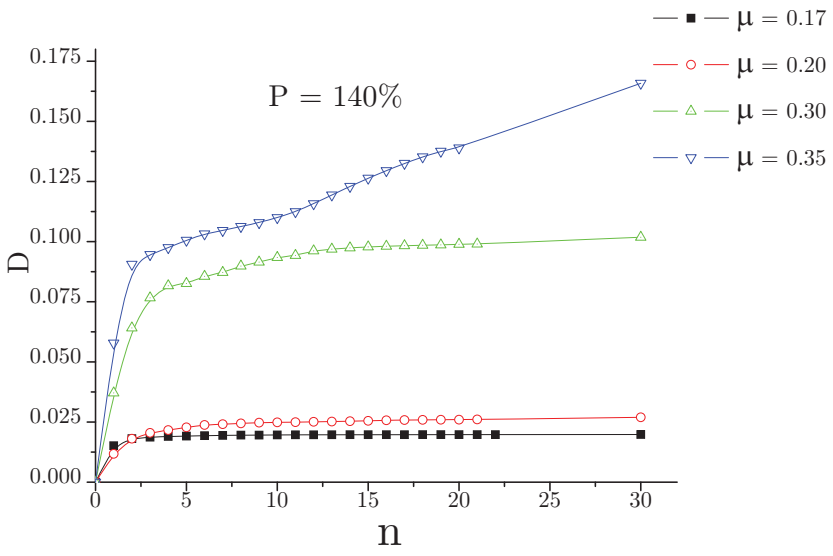

Figure 6.20: Development of damage D over number of cycles for different traction coefficient μ at P = 140%.

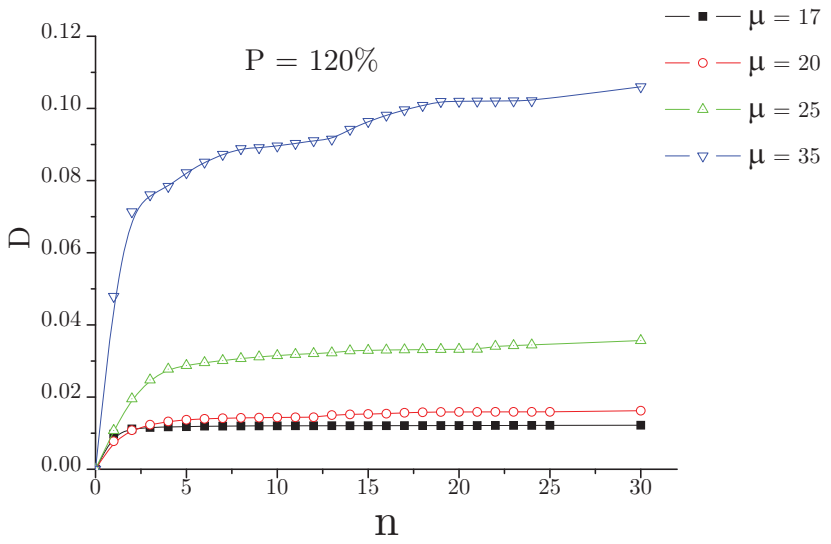

Figure 6.21: Development of damage D over number of cycles for different traction coefficient μ at P = 120%.

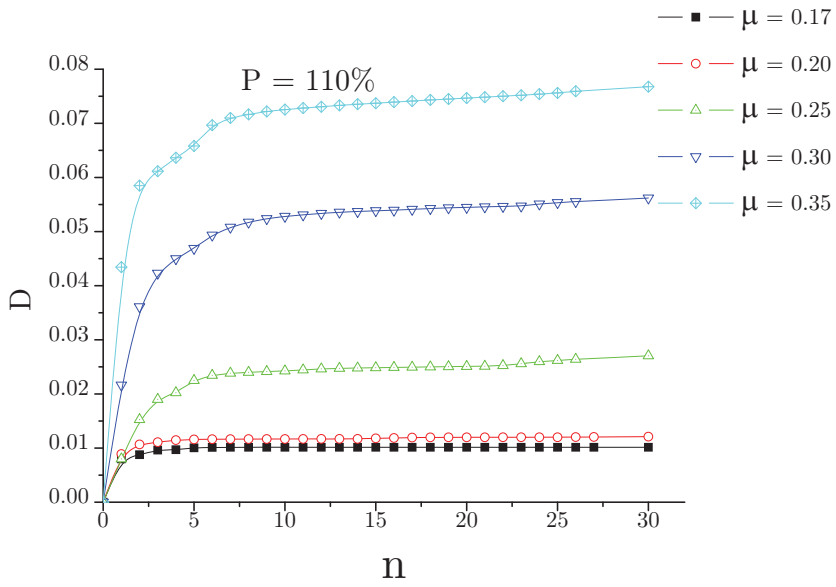

Figure 6.22: Development of damage D over number of cycles for different traction coefficient μ at P = 110%.

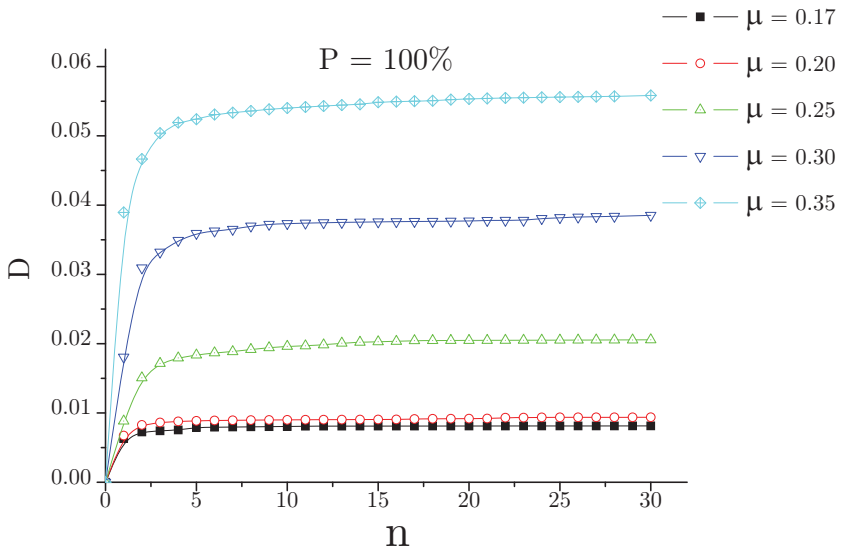

Figure 6.23: Development of damage D over number of cycles for different traction coefficient μ at P = 100%.

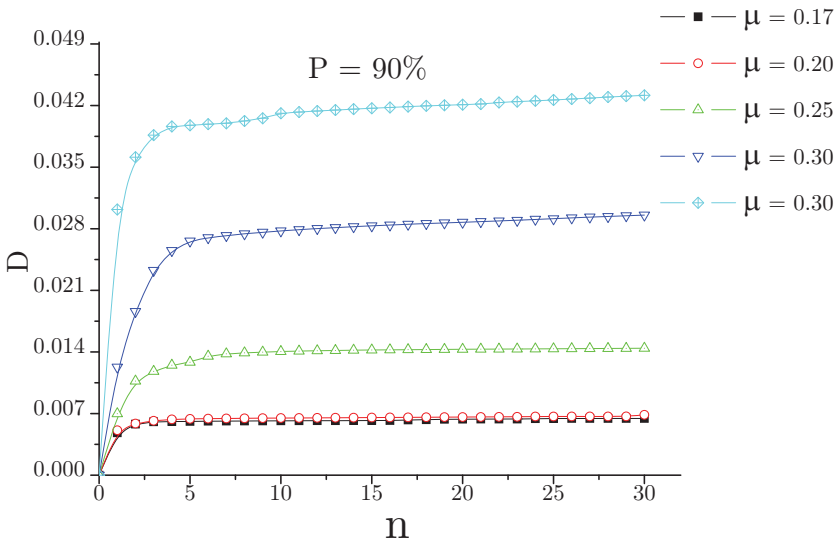

Figure 6.24: Development of damage D over number of cycles for different traction coefficient μ at P = 90%.

Fig.6.25 is basically a summary of **Fig.6.1 - Fig.6.24**. This figure is obtained by plotting the load factor P and the traction coefficient μ on the X-Y plane and the Z axis is the weighted damage rate $\overline{dD}$ as in **Sec.6.2**. The load factor L can be calculated from the maximum contact pressure p_0 and the shear yield stress k using the following relation

$$L=\frac{p_0}{k}$$

provided by Johnson [35].

The following table lists the load factor values corresponding to the calculations made.

Load(Percent)	Load Factor
30	2.592895055
50	3.07421702
70	3.439092586
90	3.739601779
100	3.873270736
110	3.998300362
120	4.115964338
140	4.332985142

Table 6.2: Relation between the Percent Load and the Load factor:

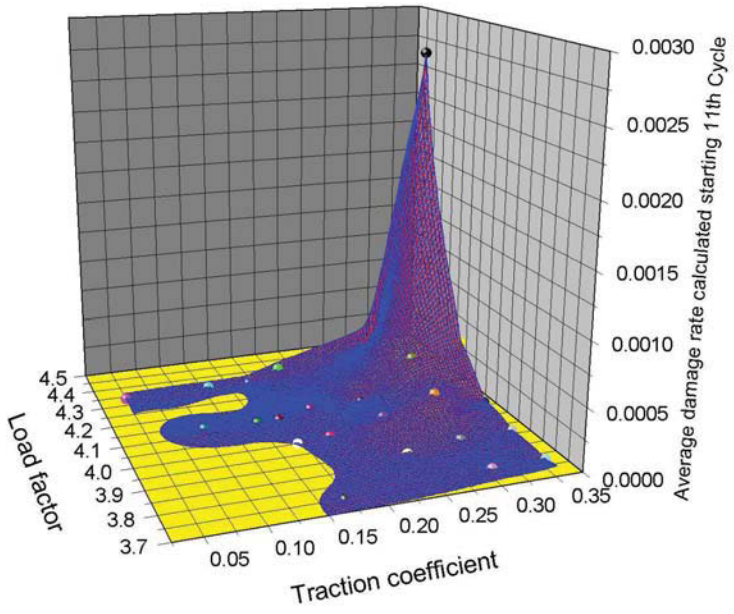

Figure 6.25: A three dimensional surface depicting the weighted damage rate for different loading cases with unidirectional loading calculated by neglecting the first 10 cycles.

A magnified view of the wheel surface reveals a development of roughness on the wheel surface. In **Fig.6.26** positions of six consecutive circumferential nodes on the wheel surface which was in contact with the rail is plotted in the beginning of the calculation and at the end of 26 cycles of loading (case 110-25). Apparently no roughness appears on the surface, but on magnifying the deformation to 100 times, the presence of unevenness on the surface is observed. This roughness is responsible for some of the fluctuations of the results encountered in the calculations. These abnormalities have been taken care by excluding the inconsistent results from the extrapolation of damage D, since a single fluctuation would have produced a big influence on the otherwise smooth development of damage D over the number of cycles n.

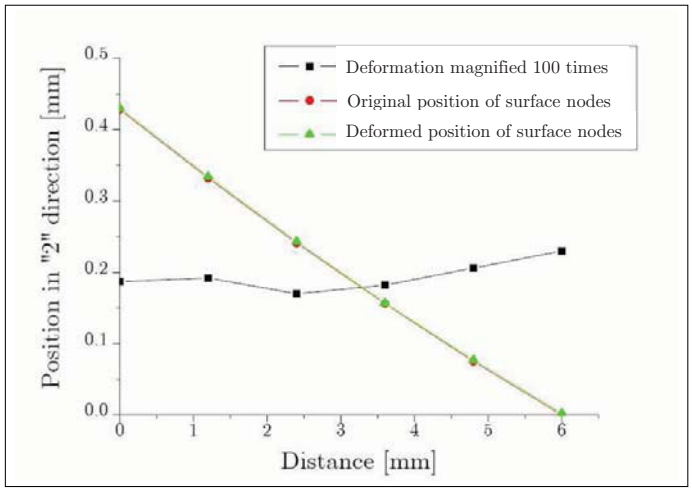

Figure 6.26: Development of roughness on the wheel surface.

6.3 Changing direction

A second set of calculations is performed with the intention of comparing the amount of accumulation of plastic strain or the development of damage in the case of unidirectional loading with the case of changing load direction.

This calculation implies unidirectional loading for the first six cycles; then alternate cycles of forward and backward traction are calculated. **Tab.6.3** lists all the calculations performed. The depth of damage is found to be nearly identical in both sets of calculations. In **Fig.6.27 - Fig.6.36** a comparison is made between the two sets of calculations. The plots clearly show that the changing of load direction leads to a drastic increase in the accumulation of plastic strain and hence causes faster damage.

Identity	P%	μ	n	Damage Depth	D	$\overline{dD}(10^{-5})$
030-35	30	0.35	41	$<$ 2 mm.	0.0001732	0.195
050-10	50	0.10	41	$<$ 2 mm.	0.0006691	0.520
050-30	50	0.30	41	$<$ 2 mm.	0.0039578	1.641
050-35	50	0.35	41	$<$ 2 mm.	0.0044437	1.356
070-10	70	0.10	40	$<$ 2 mm.	0.0033493	1.190
070-20	70	0.20	40	$<$ 2 mm.	0.0054223	1.081
070-30	70	0.30	28	Surface	0.0182586	6.754
070-35	70	0.35	38	Surface	0.0320647	9.448
090-17	90	0.17	25	$>$ 2 mm.	0.0081638	5.815
090-20	90	0.20	32	Surface	0.0102027	2.878
090-25	90	0.25	31	Surface	0.0197680	6.496
090-30	90	0.30	31	Surface	0.0379822	14.935
090-35	90	0.35	31	Surface	0.0947051	62.111
100-17	100	0.17	35	$>$ 2 mm.	0.0127245	6.996
100-20	100	0.20	29	$>$ 2 mm.	0.0140714	3.649
100-25	100	0.25	39	$<$ 2 mm	0.0299209	6.700
100-35	100	0.35	27	Surface	0.1615965	231.460
110-17	110	0.17	25	$>$ 2 mm.	0.0139769	7.935
110-20	110	0.20	27	$>$ 2 mm.	0.0212800	13.962
110-25	110	0.25	26	Surface	0.0457742	41.570
110-30	110	0.30	25	Surface	0.1015617	180.121
110-35	110	0.35	25	Surface	0.3258703	781.238
120-10	120	0.10	25	$>$ 2 mm.	0.0114493	4.853
120-15	120	0.15	25	$>$ 2 mm.	0.0159365	7.867
120-20	120	0.20	25	$>$ 2 mm.	0.0301555	30.264
120-25	120	0.25	24	Surface	0.0691806	116.616
120-30	120	0.30	24	Surface	0.1505614	368.239
120-35	120	0.35	23	Surface	0.5567754	1623.856
140-01	140	0.01	22	$>$ 2 mm.	0.0135034	0.770
140-05	140	0.05	22	$>$ 2 mm.	0.0144157	6.129
140-09	140	0.09	22	$>$ 2 mm.	0.0152284	1.928
140-13	140	0.13	20	$>$ 2 mm.	0.0204777	15.534
140-17	140	0.17	21	$>$ 2 mm.	0.0366349	48.321
140-20	140	0.20	21	$<$ 2 mm.	0.0548173	123.847
140-30	140	0.30	19	Surface	0.2498837	865.265
140-35	140	0.35	20	Surface	1.1049875	5502.017

Table 6.3: Changing direction loading cases analyzed.

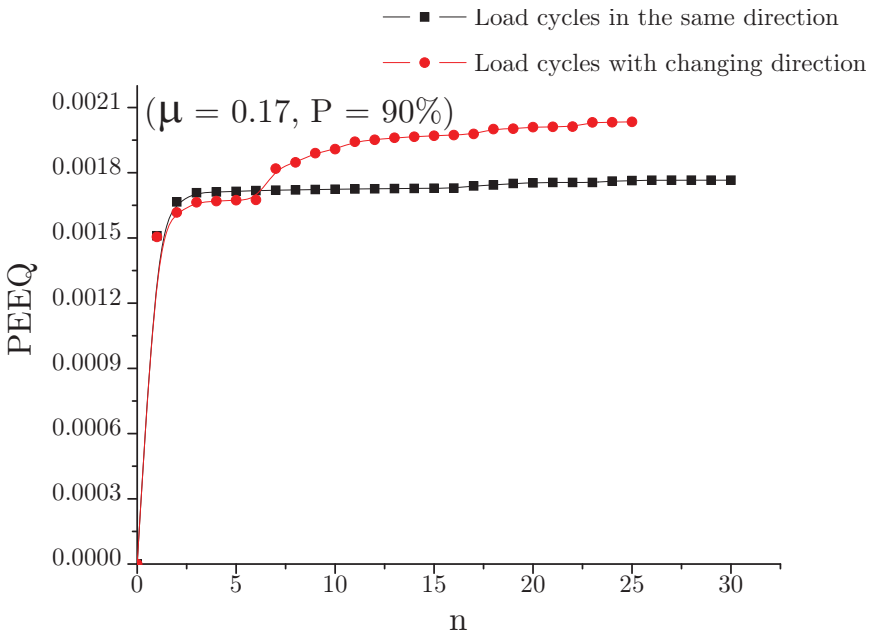

Figure 6.27: Development of accumulated equivalent plastic strain PEEQ over the load cycles for P = 90 % at $\mu = 0.17$.

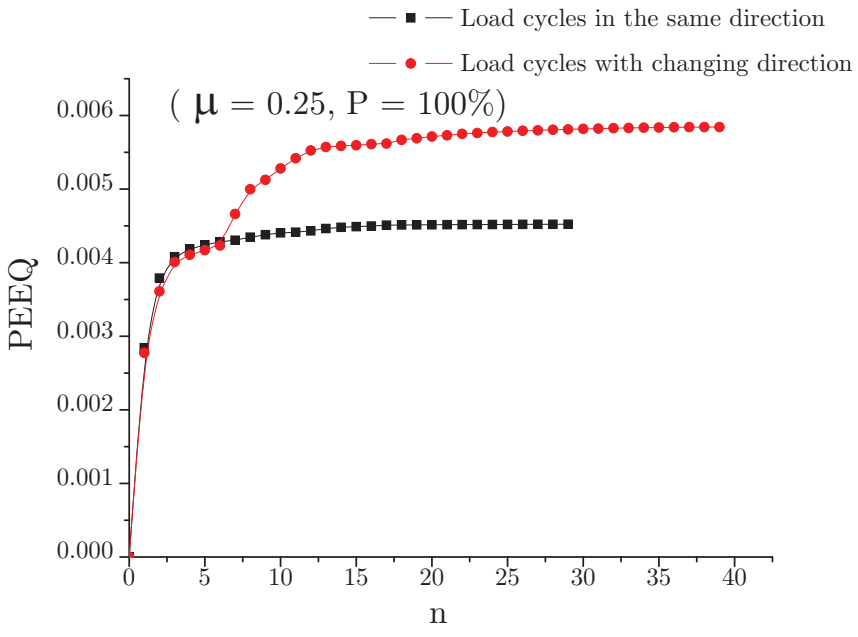

Figure 6.28: Development of accumulated equivalent plastic strain PEEQ over the load cycles for P = 100 % at $\mu = 0.25$.

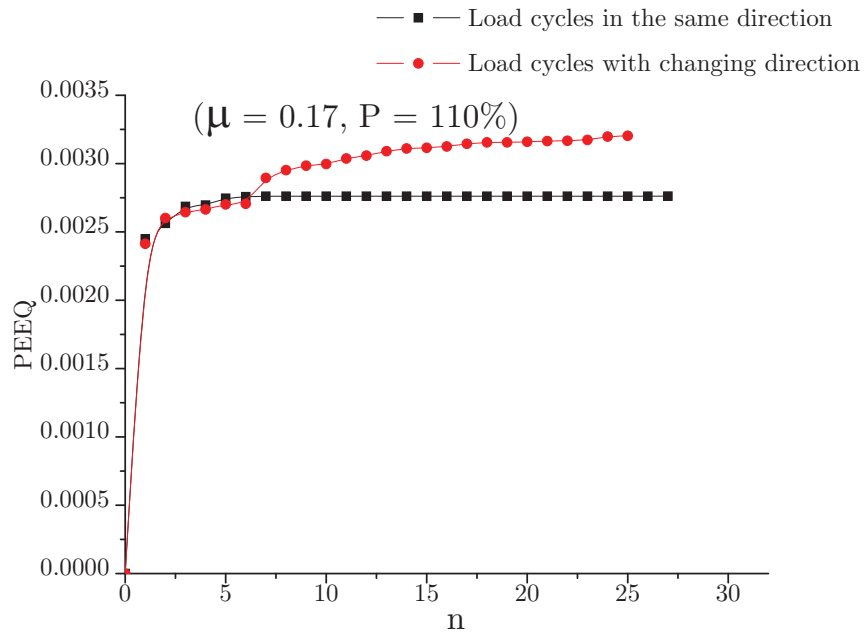

Figure 6.29: Development of accumulated equivalent plastic strain PEEQ over the load cycles for P = 110 % at $\mu = 0.17$.

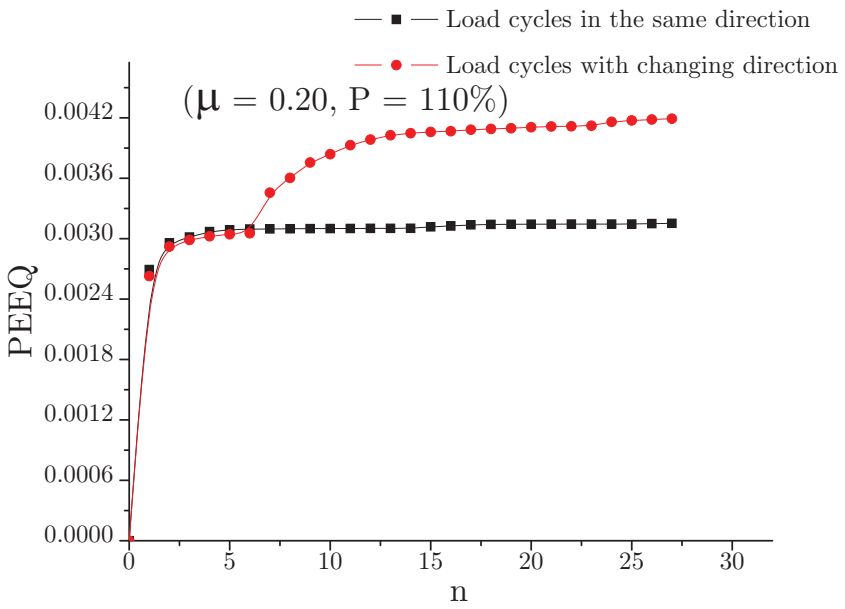

Figure 6.30: Development of accumulated equivalent plastic strain PEEQ over the load cycles for P = 110 % at $\mu = 0.20$.

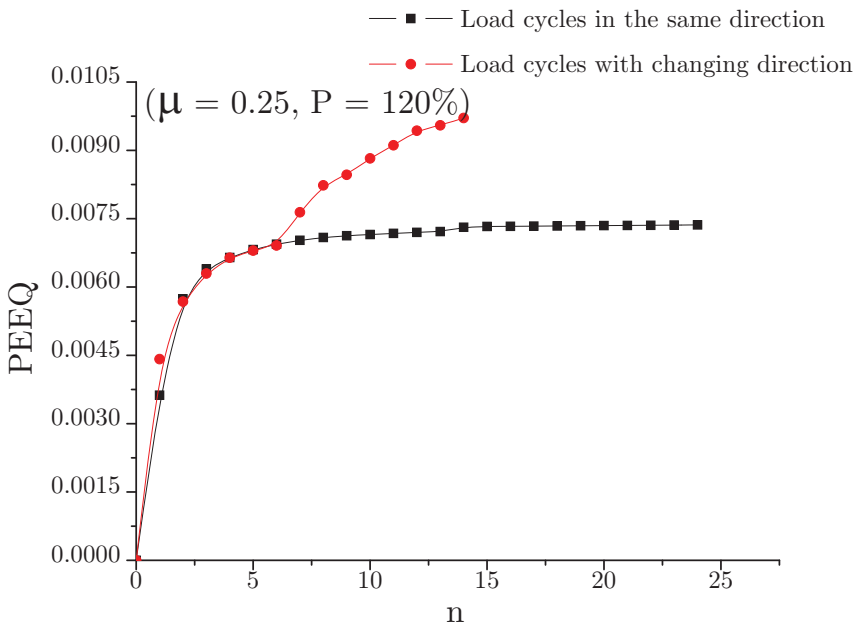

Figure 6.31: Development of accumulated equivalent plastic strain PEEQ over the load cycles for P = 120 % at $\mu = 0.25$.

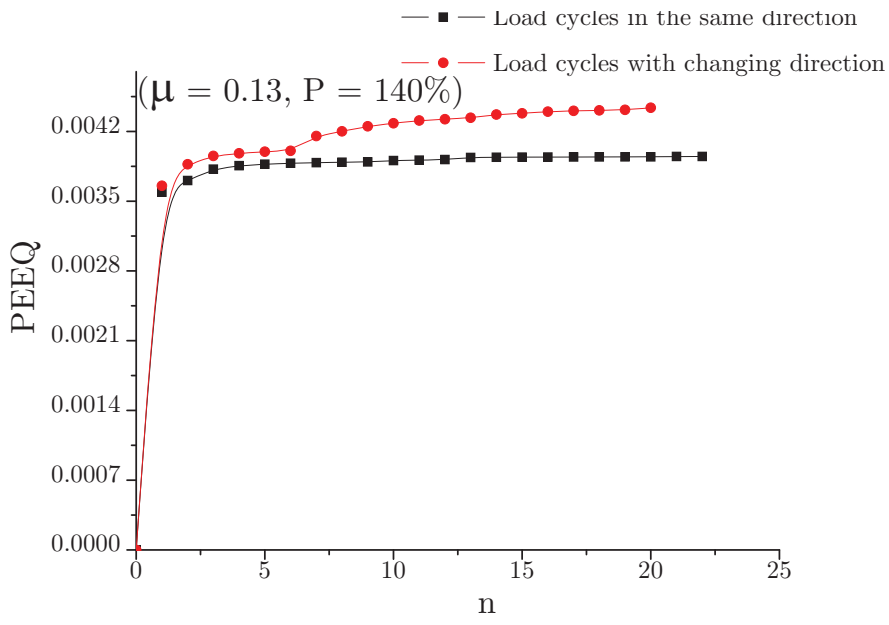

Figure 6.32: Development of accumulated equivalent plastic strain PEEQ over the load cycles for P = 140 % at $\mu = 0.13$.

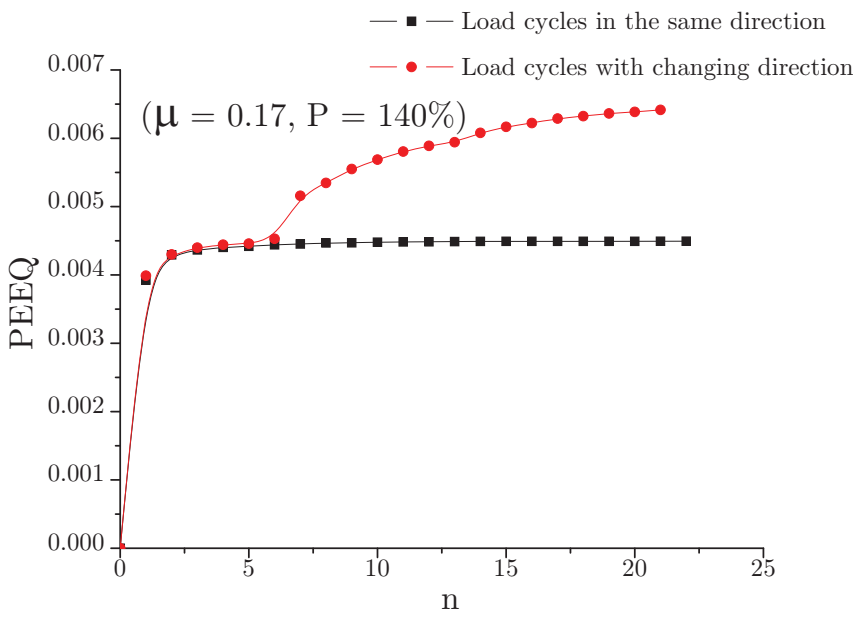

Figure 6.33: Development of accumulated equivalent plastic strain PEEQ over the load cycles for P = 140 % at $\mu = 0.17$.

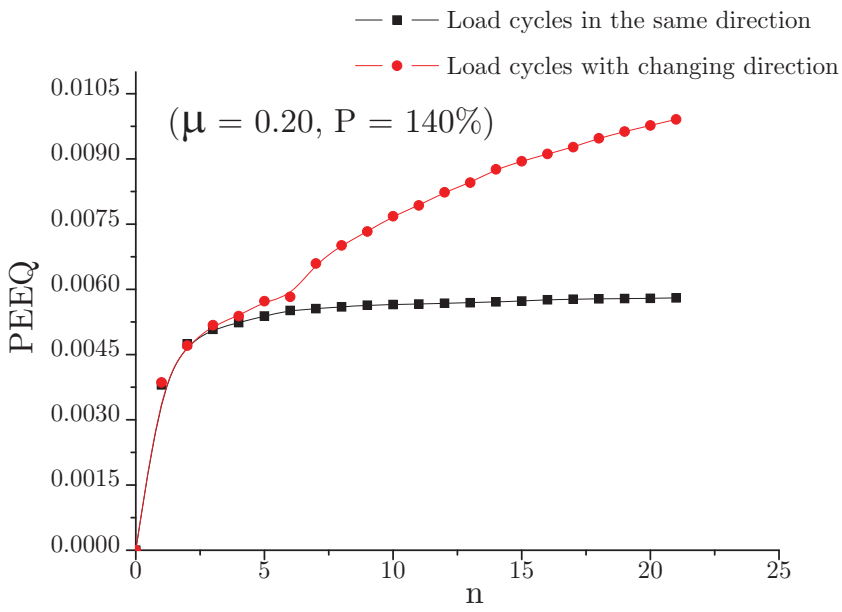

Figure 6.34: Development of accumulated equivalent plastic strain PEEQ over the load cycles for P = 140 % at $\mu = 0.20$.

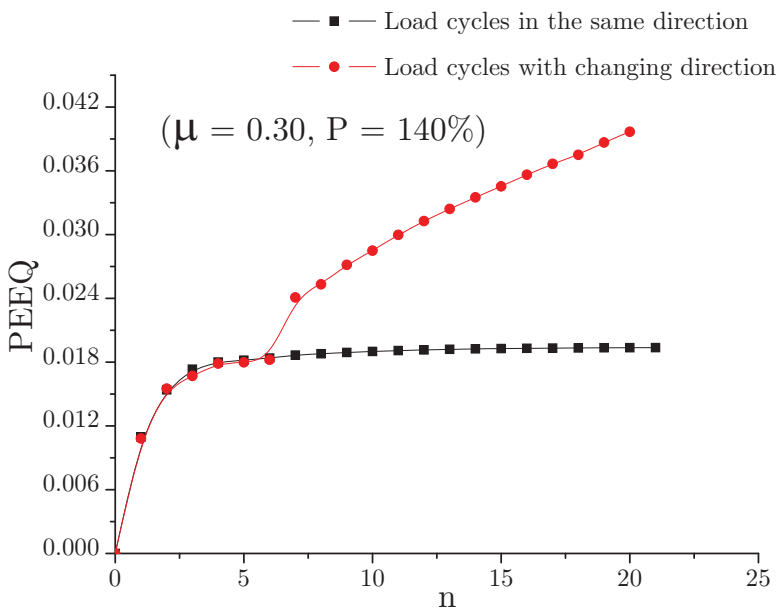

Figure 6.35: Development of accumulated equivalent plastic strain PEEQ over the load cycles for P = 140 % at $\mu = 0.30$.

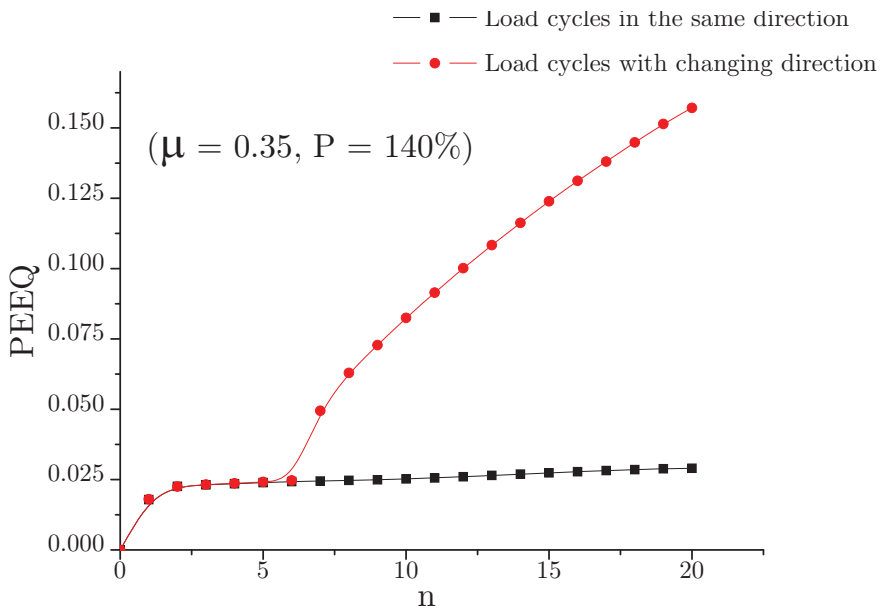

Figure 6.36: Development of accumulated equivalent plastic strain PEEQ over the load cycles for P = 140 % at $\mu = 0.35$.

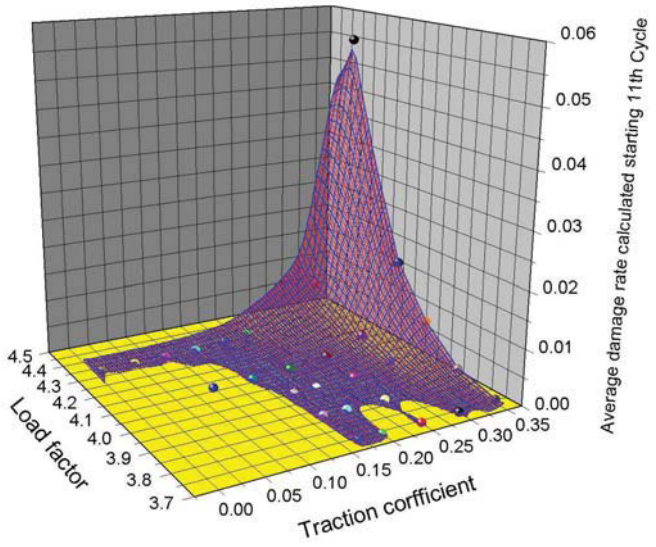

Figure 6.37: A three dimensional surface depicting the weighted damage rate for different loading cases with changing load direction calculated by neglecting the first 10 cycles.

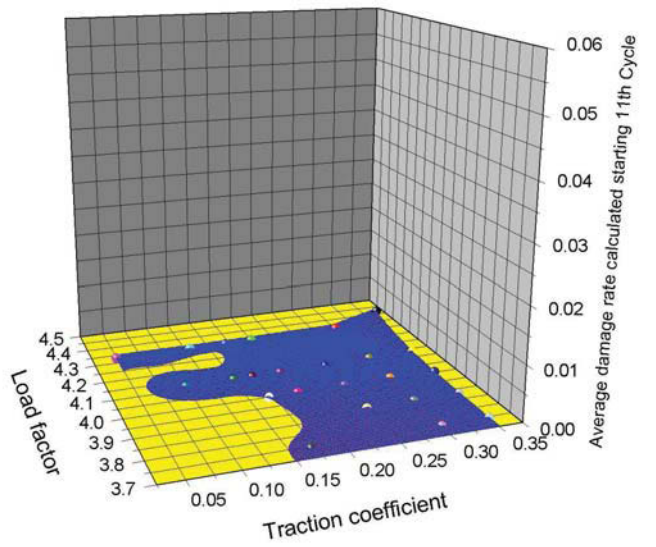

Figure 6.38: A three dimensional surface depicting the weighted damage rate for different loading cases with unidirectional loading calculated by neglecting the first 10 cycles. This figure is the same as **Fig.6.25** and is plotted using the same scale as in **Fig.6.37** for a direct comparison.

A surface depicting the weighted average damage rate for various cases is shown in **Fig.6.37**. **Fig.6.38** demonstrates the results for unidirectional loading (i.e. **Fig.6.25**) using the same scale as in **Fig.6.37** for a direct comparison and making visible the big difference in the results.

6.4 Conclusions

The analysis of the effect of repeated loading on a wheel-rail system under different loading conditions has lead to the following conclusions:

- The damage bears a very simple linear relation to the accumulated plastic strain. Hence any such analysis can be carried out taking into account only the accumulated equivalent plastic strain and the results can be later generalized for the accumulated damage D.
- A wheel-rail system undergoing a repeated loading with changing loads is more prone to damage compared to a system loaded repeatedly with the same load. The influence of changing directions is observed to be more pronounced in the cases where the major damage occurs on the surface. This effect can be justified based on the fact that surface damage on the wheel surface is governed by the amount of traction between the wheel and the rail. Furthermore repeated changing of traction direction is always accumulating plastic strain due to the kinematical hardening behavior of the wheel material and hence leads to fatigue at the wheel surface.
- The traction coefficient μ is seen to have a pronounced effect on surface damage. Although at very low values of μ almost no damage is observed, damage increases first linearly with increasing μ(μ lower than 0.17) and then increases exponentially at higher values of μ (μ higher than 0.17).
- Major part of the damage is observed to take place during the first 3-4 load cycles.
- During the numerical simulations some irregularities i.e. asperities are produced at the modeled wheel surface which was completely even at the beginning of the calculation. This effect is probably due to the surface plasitification under compression. If such a process exists in the real wheel-rail contact, a steady accumulation of plastic strain and surface damage will result due to the fact that every such irregularity will lead to very high stresses surpassing the yield limit of the material. The role of asperities in surface initiated RCF has been investigated by Alfredson et al. in [56].

CHAPTER 7

Conclusion and Future Work

7.1 Conclusions

In the first part of the work a fully dynamical three dimensional wheel-rail model is developed using the FEM package ABAQUS. This model can find application in the analysis of various phenomena involving wheel-rail contact, i.e.:

- Analysis of wheel flats.
- Analysis of irregularities in track.
- Wheel-rail contact behavior at crossings.

The model is able to describe the complete wheel-rail system with elastic-plastic material behavior. This elastic behavior allows the investigation of all the waves produced in the system including sound phenomena and the waves produced by the wheel or rail irregularities, wheel flats etc. Using this model different loading scenarios are modeled. These scenarios involve acceleration, braking, and rolling with a constant velocity. Inner and outer wheels of a train moving in a curve are also simulated. The results obtained from the FEM calculations are compared to the results obtained with multi-body calculations using the software SIMPACK. The SIMPACK calculations were performed by STS Graz.

In the second part the model is modified with the aim to make it more suitable for the analysis of the surface and near surface regions of the wheel. It was necessary to develop a quasi-static wheel-rail model which allows the inclusion of the dynamic rolling process as well as a fine representation of the stress-strain behavior near the wheel surface due to contact. Most existing models are either based on static stamping of the wheel on the rail, or the contact is simulated by moving a force field consisting of normal and tangential forces on the wheel surface. The model at hand provides a high amount of flexibility for implementing a different material behavior for both the wheel and the rail. Some features of the material behavior that can be modeled is plasticity including plastic isotropic or kinematic hardening as wells and mixed cyclic hardening. Modern theories for the evaluation of a damage indicator can also be integrated in this model. The new model is a very useful tool for understanding the problem of rolling contact fatigue from the very ground level. Physical quantities like stress and strains can be calculated for a wide variety of loading and material combinations.

As a basic investigation a usual spectrum of loading conditions encountered by a railway wheel are analyzed. This spectrum includes the following loading conditions:

- An accelerated wheel on a straight track.
- A wheel moving with a constant velocity on a straight track.
- A braking wheel on a straight track.
- A wheel moving on the inner rail of a curved track.
- A wheel moving on the outer rail of a curved track.

After the quantitative evaluation of the plastic strains accumulated in the wheel under different loading conditions it is found that the plastification obtains a maximum in the case of a wheel moving on the outer rail of a curved track. The plastification observed in this case is approximately seven times higher than that due to an accelerating or braking wheel.

Higher compressive stresses are observed in the wheel in the case of acceleration in comparison to those in the case of braking.

It has also been established that a wheel moving with a constant velocity produces a very low amount of plastic strain in the investigated load cases.

Comparing the values of the accumulated damage D and the accumulated equivalent plastic strain PEEQ it is seen that both quantities follow the same trend in the way they accumulate during cyclic loading.

In the third part of the work cyclic calculations are performed with alternating traction direction, which lead to the finding that a wheel undergoing mixed loading under a high traction coefficient may produce severe surface damage.

Furthermore, repeated changing of the traction direction is always accumulating plastic strain due to the kinematical plasitification behavior of the wheel material, hence leading to fatigue at the wheel surface.

During the numerical simulations an uneven surface is produced at the modeled wheel surface which was completely even at the beginning of the calculation. This effect is probably due to the surface plasitification under compression. If such a process exists in the real wheel-rail contact, a steady accumulation of plastic strain and surface damage will result due to the fact that every unevenness will lead to very high stresses surpassing the yield limit of the material.

After performing the parametric study of the effect of the traction coefficient on the accumulation of plastic strain, it is found that for lower values of the traction coefficient(μ less than 0.17), the accumulated plastic strain increases linearly with increasing traction coefficient but at higher values of the traction coefficient(μ greater than 0.17), the accumulated plastic strain increases exponentially.

Looking at the step by step increase in the accumulated damage for different loading cases, it is concluded that the major amount of damage takes place in the first few cycles of loading.

7.2 Future work

There is always a scope of building better models and getting more precise results. The model at hand can be used and improved to investigate more complicated dynamic and static wheel-rail problems. The high amount of flexibility available in the model allows changes in the wheel or the rail geometry and changes of the wheel and rail material. The geometrical position of the wheel and the rail can also be adjusted for defining different loading conditions. Also normal and driving forces can be easily controlled.

There is a need to make further calculations using different wheel and rail material behaviors. Calculations involving higher number of load cycles will be useful to further explain the formation and growth of cracks both in the wheel and the rail. Analysis involving already existing surface and subsurface cracks is of major interest. The focus of future studies could thus be to involve the presence of cracks into the existing EEM model.

List of Figures

1.1 Accident Site - ICE 2

1.2 Broken wheel - ICE 2

1.3 spalling on the wheel tread surface 4

1.4 Sketch of plastic deformation of the surface material in a railway wheel. The dotted lines indicate the material planes before and after deformation [11] 6

2.1 Structural response to cyclic loading 12

2.2 Shakedown map for point contacts [35] 14

3.1 Orienting the wheel and the rail (STS Graz) 16

3.2 Orienting the wheel and the rail (STS Graz) 17

3.3 Full Wheel Model 18

3.4 Full Rail Model 19

3.5 Mechanical model 20

3.6 Full Model - Meshed 22

3.7 Coordinate System 23

3.8 Magnitude of the contact slip rate FSLIPR at slave nodes on the wheel surface after contact 24

3.9 Contact variables as the wheel surface 25
3.10 Stress components in the loaded wheel 26
3.11 Reaction forces in the system 27
3.12 Energy balance in the system 28
3.13 Velocity and displacement components of the wheel 29
3.14 Contact area and slip velocity at the wheel surface 30

4.1 The two parts of the modeled wheel 34
4.2 The two parts of the modeled rail 35
4.3 Definition of the contact point (STS Graz) 36
4.4 Details of the rail and wheel geometry 37

5.1 Part of the wheel modeled as deformable 44
5.2 Part of the rail modeled as deformable 44
5.3 Engineering stress engineering strain curve for wheel material 45
5.4 Location of various load scenarios on shakedown map 49
5.5 Driving moment applied on the axle of the wheel for modeling a wheel running on a straight track - 3 cycles of acceleration, 3 cycles of pure rolling and 2 cycles of braking 49
5.6 Wheel running on a straight track - 3 cycles of acceleration, 3 cycles of pure rolling and 2 cycles of braking 50
5.7 Wheel running on the outer rail in a curved track 50
5.8 Wheel running on a straight track 51
5.9 Relative longitudinal and shear stress distribution on a line in rolling direction through the center of a contact patch in the case of pure rolling during the third cycle(a=semiaxis, in the rolling direction, of the contact ellipse) 51
5.10 Relative longitudinal and shear stress distribution on a line in rolling direction through the center of a contact patch in the case of an outer wheel in a curve during the third cycle(a=semiaxis, in the rolling direction, of the contact ellipse) 52

5.11 Relative longitudinal and shear stress distribution on a line in rolling direction through the center of a contact patch in the case of an inner wheel in a curve during the first cycle(a=semiaxis, in the rolling direction, of the contact ellipse) 52

5.12 Relative longitudinal and shear stress distribution on a line in rolling direction through the center of a contact patch in the case of a braking wheel during the third cycle(a=semiaxis, in the rolling direction, of the contact ellipse) 53

5.13 Relative longitudinal and shear stress distribution on a line in rolling direction through the center of a contact patch in the case of an accelerating wheel during the third cycle(a=semiaxis, in the rolling direction, of the contact ellipse) 53

6.1 Dependence of PEEQ on μ 60

6.2 Dependence of D on μ 60

6.3 Dependence of PEEQ on P 61

6.4 Dependence of D on P 61

6.5 Development of accumulated equivalent plastic strain PEEQ for different loading at a constant $\mu = 0.35$ 62

6.6 Development of accumulated equivalent plastic strain PEEQ for different loading at a constant $\mu = 0.30$ 63

6.7 Development of accumulated equivalent plastic strain PEEQ for different loading at a constant $\mu = 0.25$ 63

6.8 Development of accumulated equivalent plastic strain PEEQ for different loading at a constant $\mu = 0.20$ 64

6.9 Development of damage D for different loading P over number of cycle n at a constant $\mu = 0.17$ 64

6.10 Development of D for different loading at a constant $\mu = 0.35$ 65

6.11 Development of D for different loading at a constant $\mu = 0.30$ 65

6.12 Development of D for different loading at a constant $\mu = 0.25$ 66

6.13 Development of V for different loading at a constant $\mu = 0.20$ 66

6.14 Development of D for different loading at a constant $\mu = 0.17$ 67

6.15 Development of accumulated equivalent plastic strain PEEQ over number of cycles for different traction coefficient μ at P = 140% 68

6.16 Development of accumulated equivalent plastic strain PEEQ over number of cycles for different traction coefficient μ at P = 120% 68

6.17 Development of accumulated equivalent plastic strain PEEQ over number of cycles for different traction coefficient μ at P = 110% 69

6.18 Development of accumulated equivalent plastic strain PEEQ over number of cycles for different traction coefficient μ at P = 100% 69

6.19 Development of accumulated equivalent plastic strain PEEQ over number of cycles for different traction coefficient μ at P = 90% 70

6.20 Development of damage D over number of cycles for different traction coefficient μ at P = 140% 70

6.21 Development of damage D over number of cycles for different traction coefficient μ at P = 120% 71

6.22 Development of damage D over number of cycles for different traction coefficient μ at P = 110% 71

6.23 Development of damage D over number of cycles for different traction coefficient μ at P = 100% 72

6.24 Development of damage D over number of cycles for different traction coefficient μ at P = 90% 72

6.25 A three dimensional surface depicting the weighted damage rate for different loading cases with unidirectional loading calculated by neglecting the first 10 cycles 73

6.26 Development of roughness on the wheel surface. 74

6.27 Development of accumulated equivalent plastic strain PEEQ over the load cycles for P = 90 % at μ = 0.17 76

6.28 Development of accumulated equivalent plastic strain PEEQ over the load cycles for P = 100 % at μ = 0.25 76

6.29 Development of accumulated equivalent plastic strain PEEQ over the load cycles for P = 110 % at μ = 0.17 77

6.30 Development of accumulated equivalent plastic strain PEEQ over the load cycles for P = 110 % at μ = 0.20 77

6.31 Development of accumulated equivalent plastic strain PEEQ over the load cycles for P = 120 % at $\mu = 0.25$ 78

6.32 Development of accumulated equivalent plastic strain PEEQ over the load cycles for P = 140 % at $\mu = 0.13$ 78

6.33 Development of accumulated equivalent plastic strain PEEQ over the load cycles for P = 140 % at $\mu = 0.17$ 79

6.34 Development of accumulated equivalent plastic strain PEEQ over the load cycles for P = 140 % at $\mu = 0.20$ 79

6.35 Development of accumulated equivalent plastic strain PEEQ over the load cycles for P = 140 % at $\mu = 0.30$ 80

6.36 Development of accumulated equivalent plastic strain PEEQ over the load cycles for P = 140 % at $\mu = 0.35$ 80

6.37 A three dimensional surface depicting the weighted damage rate for different loading cases with changing load direction calculated by neglecting the first 10 cycles 81

6.38 A three dimensional surface depicting the weighted damage rate for different loading cases with unidirectional loading calculated by neglecting the first 10 cycles. This figure is the same as **Fig.6.25** and is plotted using the same scale as in **Fig.6.37** for a direct comparison. 81

List of Tables

3.1 Wheel and rail material properties 19

3.2 Coordinate system definition 23

3.3 Comparison of input values provided by STS and results calculated by MCL. 31

4.1 Translation of the coordinate system. 38

4.2 Comparing the results of the FE and MBS simulations (Case of a straight track). 40

4.3 Comparing the results of the FE and MBS simulations. (Case of the inner wheel in a curve) 41

5.1 Angles defining the relative position of the wheel and the rail for various scenarios 45

5.2 Wheel and rail material properties 46

5.3 Variables describing kinetics and dynamics of the system 46

6.1 Unidirectional loading cases analyzed. 59

6.2 Relation between the percent load and the load factor 73

6.3 Changing direction loading cases analyzed. 75

Bibliography

[1] H. A. Richard, M. Fulland, M. Sander and G. Kullmer: "Fracture in a rubber-sprung railway wheel", *Eng. Fail. Anal.* **12**:986–999, 2005.

[2] V. Esslinger, R. Kieselbach, R. Koller and B. Weisse: "The railway accident of Eschede - technical background", *Eng. Fail. Anal.* **11**:515–535, 2004.

[3] Y. Liu, B. Stratman and S. Mahadevan: "Fatigue crack initiation life prediction of railroad wheels", *Int. J. Fatigue* **28**:747–756, 2006.

[4] M. Civarella and H. Maitournam: "On the cycle fatigue limit for tolling contact fatigue", *Proc. 7th ICBMFF, June 28 - July 1, 2004, Berlin, Germany* pp. 637–642, 2004.

[5] S. M. Zakharov and I. G. Goryacheva: "Rolling contact fatigue defect in freight car wheels", *Wear* **258**:1142–1147, 2005.

[6] F. D. Fischer, W. Daves and E. A. Werner: "On the temperature in the wheel-rail rolling contact", *Fatigue Fract. Eng Mat. Struct.* **26**:999–1006, 2003.

[7] J. Ahlstroem and B. Karlsson: "Microstructural evaluation and interpretation of the mechanically and thermally affected zone under railway wheel flats", *Wear* **232**:01–14, 1999.

[8] T. Makino, M. Yamamoto and T. Fujimura: "Effect of material on spalling properties of railroad wheels", *Wear* **253**:284–290, 2002.

[9] T. N. Farris, L. M. Keer and R. Steele: "The effect of service loading on shell growth in rails", *J. Mech. Phys. Solids* **35**:677–700, 1987.

[10] K. L. Johnson: "Contact mechanics", *Cambridge University Press, Cambridge UK* pp. 452–459, 1987.

[11] A. Ekberg and E. Kaboo: "Fatigue of railway wheels and rails under rolling contact fatigue and thermal loading-an overview", *Wear* **258**:1288–1300, 2005.

[12] A. Ekberg and P. Sotkovski: "Anisotropy and rolling contact fatigue of railway wheels", *Int. J. Fatigue* **23**:29–43, 2001.

[13] U. Zerbst, K. Mädler and H. Hintze: "Fracture mechanics in railway applications - an overview", *Eng. Fract. Mech.* **72**:163–194, 2005.

[14] H. Hertz: "Über die Berührung fester elastischer Körper", *ZAMM* **92**:156–171, 1881.

[15] J. A. Greenwood and J. B. P. Williamson: "Contact of normally flat surfaces", *Proc. R. Soc. London* **295**:300–319, 1966.

[16] J. A. Greenwood: "Analysis of elliptical Herztian contacts", *Tribol. Int.* **30**:235–237, 1997.

[17] D. H. Cooper: "Hertzian contact-stress deformation coefficients", *ASME J. Appl. Mech.* **36**:296–303, 1969.

[18] F. D. Fischer, E. R. Oberaigner, W. Daves, M. Wiest, H. Blumauer and H. Ossberger: "The impact of wheel on a crossing", *ZEVrail Glasers Annalen* **129**:336–345, 2005.

[19] P. Podra and S. Andersson: "Finite element analysiswear simulation of a conical spinning contact considering surface topology", *Wear* **224**:13–21, 1999.

[20] S. Bogadanski: "Liquid-solid interaction at opening in rolling contact fatigue cracks", *Wear* **258**:1273–1279, 2005.

[21] A. Sladkowski and M. Sitarz: "Analysis of wheel-rail interaction using FE software", *Wear* **258**:1217–1223, 2005.

[22] Y. Q. Sun and M. Dhanasekar: .

[23] M. Guagliano and L. Vergani: "Experimental and numerical analysis of sub-surface cracks in railway wheels", *Eng Fract. Mech.* **72**:255–269, 2005.

[24] P. Massimiliano, A. Francesco and G. Francesco: "Distribution of contact pressure in wheel-rail contact area", *Wear* **253**:365–274, 2002.

[25] P. D. Warren, D. A. Hills and D. N. Dai: "Mechanism of Hertzian cracking", *Tribol. Int.* **28**:357–362, 1995.

[26] M. Andersson: "Stress distribution and crack initiation for an elastic contact including friction", *Int. J. Solids Struct.* **33-25**:3673–3696, 1995.

[27] F. W. Carter: "On the action of a locomotive driving wheel", *Proc. R. Soc. London A* **112**:151–157, 1926.

[28] Z. Y. Shen, J. K. Hedrick and J. A. Elkins: "A comparison of alternative creep-force models for rail vehicle dynamic alalysis, in J. K. Hedrick (ed.)", *The Dynamics of Vehicles, Proc. 8th IAVSD Symp., Cambridge,1984 MA, Swets and Zeitlinger, Lisse* pp. 591–605, 1984.

[29] J. J. Kalker: "Simplified theory of rolling contact", *Delft Progress Report* **1**:1–10, 1973.

[30] J. J. Kalker: "A fast algorithm for the simplified theory of rolling contact", *Vehicle Syst. Dyn.* **11**:1–13, 1982.

[31] J. J. Kalker: "On the rolling contact of two elastic bodies in the presence of dry friction", *PhD Thesis University Delft* 1967.

[32] J. J. Kalker: "Wheel-rail contact theory, algorithms and applications", *Strojnicky Casopis* **49**:1–26, 1998.

[33] J. J. Kalker: "Wheel-rail rolling contact theory", *Wear* **144**:243–261, 1991.

[34] K. L. Johnson: "Contact mechanics and the wear of metals", *Wear* **190**:162–170, 1995.

[35] K. L. Johnson: "The application of shakedown principles in rolling and sliding contacts", *Eur. J. Mech. A-Solids* **11**:155–172, 1992.

[36] M. Boulbibane and I. F. Collins: "The calculation of shakedown loads for contact problems", *Key Eng. Mat.* **122-180**:763–774, 2000.

[37] M. Ertz and K. Knothe: "Thermal stress and shakedown in wheel rail contact", *Arch. Appl. Mech.* **72**:715–729, 2003.

[38] I. Y. Shevtsov, V. L. Markine and C. Esveld: "Optimal design of wheel profiles for railway vehicles", *Wear* **258**:1022–1030, 2005.

[39] H. D. Grohmann and K. H. A. Groß-Thebing: "A new RCF, experimental investigations and theoretical modelling", *Wear* **253**:67–74, 2002.

[40] T. Jendel: "Prediction of wheel profile wear –comparison with field measurements", *Wear* **253**:89–99, 2002.

[41] E. Magel, J. Kalousek and R. Caldwell: "A numerical simulation of wheel wear", *Wear* **258**:1245–1254, 2005.

[42] T. Klisch: "Contact mechanics in multibody systems", *Mech. Mach Theory* **34**:665–675, 1999.

[43] B. Gilbert: "VAMPIRE-Opportunities for fast, optimised, railway simulations", *CEng, MIMechE - AEA Technology Rail, Derby, UK.* 2001.

[44] ABAQUS: "Prescribed conditions, constraints and interactions", *ABAQUS Version 6.5 www.abaqus.at* **V**, 2006.

[45] "Abaqus Maunal", *Simulia* **Volume 7.7**, 2007.

[46] W. Daves, W. P. Yao, F. D. Fischer, P. Pointner, R. Stock, R. Oswald and H. Blumauer: "Dynamical finete element analysis - A wheel in a curve and a wheel passing a crossing", *Proc. CM2003 Gothenburg, Sweden, June 10-13* pp. 455–660, 2003.

[47] J. W. Ringsberg, H. Bjarnehed, A. Johnson and B. L. Josefson: "Rolling contact fatigue of rails - finite element modelling of residual stresses, strains and crack initiation", *J. Rail Rapid Transit* **214**:7–19, 2000.

[48] T. Telliskivi and U. Olofsson: "Contact mechanics Analysis of measured Wheel-Rail Profiles using the finite element methods", *Journal of Rail Rapid Transit* **215**:65–72, 2000.

[49] Y. Bao and T. Wierzbicki: "On fracture locus in the equivalent strain and stress triaxiality space", *Int. J. Mech. Sci.* **46**:81–98, 2004.

[50] H. P. Gänser, A. G. Atkins, O. Kolednik, F. D. Fischer and O. Richard: "Upsetting of cylinders A comparison of two different damage indicators", *ASME J Eng. Met. Techn.* **123**:94–99, 2001.

[51] F. D. Fischer, O. Kolednik, G. X. Shan and F. G. Rammerstorfer: "A note on caliberation of ductile failure damage indicators", *Int. J. Fracture* **73**:345–357, 1995.

[52] J. W. Hancock and A. C. Mackenzie: "On the mechanisms of ductile failure in High-Strenght steels subjected to Multi-Axial Stress-States", *J. Mech. Phys. solids* **24**:147–169, 1976.

[53] J. R. Rice and D. M. Tracey: "On the ductile enlargement of voids in triaxial stress fields", *J. Mech. Phys. solids* **17**:201–217, 1969.

[54] T. Drabek and H. J. Böhm: "Damage models for studying ductile matrix failure in composites", *Comp. Mater. Sci.* **32**:329–336, 2005.

[55] W. Daves, B. P. Singh and K. Six: "Rolling contact fatigue of Wheels - Finite element modelling", *7th international conferrence on contact mechanics and wear of Rail/wheel systems(CM2006), Brisbane, Australia, September 24-26* 2006.

[56] B. Alfredsson, J. Dahlberg and B. Olsson: "The role of a single surface asperity in rolling contact fatigue", *Wear* **In press**, 2007.